

UNIVERSITY OF CALIFORNIA

Los Angeles

Integrated Cryogenic Buffer Gas Beam, Linear Quadrupole Trap, and Time of Flight Mass  
Spectrometer for Low Temperature Ion-Molecule Chemistry

A dissertation submitted in partial satisfaction

of the requirements for the degree

Doctor of Philosophy in Physics

by

Gary Chen

2019

© Copyright by

Gary Chen

2019

ABSTRACT OF THE DISSERTATION

Integrated Cryogenic Buffer Gas Beam, Linear Quadrupole Trap, and Time of Flight Mass Spectrometer for Low Temperature Ion-Molecule Chemistry

by

Gary Chen

Doctor of Philosophy in Physics

University of California, Los Angeles, 2019

Professor Wes Campbell, Chair

The dissertation of Gary Chen is approved.

Eric Hudson

Paul Hamilton

James Larkin

Wes Campbell, Committee Chair

University of California, Los Angeles

2019

?

## CONTENTS

<b>List of Figures . . . . .</b>	<b>viii</b>
<b>Preface . . . . .</b>	<b>xiii</b>
<b>Curriculum Vitae . . . . .</b>	<b>xiv</b>
<b>1 Introduction . . . . .</b>	<b>1</b>
1.1 Thesis Outline . . . . .	1
<b>2 Chemical Rate Constants . . . . .</b>	<b>2</b>
2.1 Average Dipole Orientation Theory (ADO) . . . . .	3
2.1.1 General Treatment of Adiabatic Capture Theory . . . . .	3
2.1.2 Ion-Dipole Interaction . . . . .	5
2.2 Statistical State Counting . . . . .	10
<b>3 The Cryogenic Buffer Gas Beam (CBGB) . . . . .</b>	<b>11</b>
3.1 Design . . . . .	13
3.1.1 Heat Load and Thermal Conductivity . . . . .	16
3.1.2 Gas Fill Lines . . . . .	19
3.2 Beam Density and Extraction . . . . .	23
3.2.1 Direct density measurements . . . . .	27
3.3 Beam Velocity . . . . .	32
3.4 Beam Shuttering . . . . .	35
<b>4 Trapping and Cooling Ions . . . . .</b>	<b>38</b>

4.1	Ion Trapping . . . . .	38
4.2	Vacuum Requirements . . . . .	38
4.3	${}^9\text{Be}^+$ Laser Cooling . . . . .	38
4.4	Time of Flight Mass Spectrometer (TOF-MS) . . . . .	42
4.5	Dual Species Loading . . . . .	42
<b>5</b>	<b><math>\text{Be}^+({}^2\text{S}_{1/2}/{}^2\text{P}_{3/2}) + \text{H}_2\text{O}</math></b> . . . . .	<b>46</b>
5.1	Optical Control of Reactions between Water and Laser-Cooled $\text{Be}^+$ Ions . . . . .	46
5.1.1	Abstract . . . . .	46
<b>6</b>	<b><math>\text{Be}^+ + \text{H}_2\text{O/HOD/D}_2\text{O}</math></b> . . . . .	<b>53</b>
6.1	Isotope-selective chemistry in the $\text{Be}^+({}^2\text{S}_{1/2}) + \text{HOD} \longrightarrow \text{BeOD}^+ / \text{BeOH}^+ + \text{H/D}$ reaction . . . . .	53
6.2	Abstract . . . . .	53
6.3	Introduction . . . . .	53
6.4	Experimental . . . . .	55
6.5	Results and Discussion . . . . .	59
6.6	Conclusion . . . . .	61
6.7	Notes . . . . .	62
6.8	$\text{Be}^+ + \text{HOD}$ branching ratio . . . . .	64
<b>7</b>	<b><math>\text{Be}^+ + \text{O}_2</math></b> . . . . .	<b>66</b>
<b>8</b>	<b><math>\text{C}^+ + \text{H}_2\text{O}</math></b> . . . . .	<b>70</b>
8.1	Formyl Isomer Branching Ratio . . . . .	70
8.2	$\text{CO}_2$ Titration . . . . .	73
8.2.1	$\text{Be}^+ + \text{CO}_2$ . . . . .	75

8.2.2	$\text{C}^+ + \text{CO}_2$	76
8.2.3	$\text{Be}^+ + \text{C}^+ + \text{H}_2\text{O}$ with $\text{CO}_2$	78
8.3	$^{15}\text{N}_2$ Titration	81
8.3.1	Estimate Isomerization	81
<b>9</b>	<b>Conclusion and Future Outlook</b>	<b>82</b>
<b>A</b>	<b>CBGB Drawings</b>	<b>83</b>
<b>References</b>		<b>85</b>

## LIST OF FIGURES

2.1	Rough plotting of $\theta_1$ as a function of maximum angle $K$ . The behaviour is as expected, the greater the maximal capture angle, the more $\theta_1$ tends towards 0 . . . . .	8
2.2	$\theta_2$ as a function of the ratio of rotational energy and the monopole-dipole term. The low ratio behavior is not immediately obvious, but the greater the ratio between the rotational energy and monopole-dipole term, the more $\theta_2$ tends towards $\pi/2$ . . . . .	9
3.1	Schematic of target species entrainment within a buffer gas beam cell. With high densities of buffer gas particles, an introduced target species undergoes collisions with the buffer gas such that it cools. At high enough densities, flow dynamics cause the target species to become entrained in the buffer gas flow and are carried out of the cell with greater efficiency. . . . .	12
3.2	Cross sectional view of CBGB in solidworks. Components include copper sheath for PTR, aluminum radiation shield with chevron baffles, copper shield and experimental cell, and skimmer mounted in stem chamber. The baffles allow for gas to flow into the cold region of the beam apparatus, while preventing 300 K black body radiation from hitting the inner shield and cell. . . . .	15
3.3	Cross sectional view of CBGB with side walls removed from the outer vacuum chamber, 40 K aluminum radiation shield, and inner 4 K cryopumping shield exposing the inner experimental cell. A skimmer is mounted in the stem region. . . . .	16
3.4	The water fill line, sealed by an ultratorr fitting and heated by nichrome wire. A shut off valve and vernier valve are used to regulate the flow of water into the buffer gas cell. . . . .	21

3.5 A kapton film serves as the back wall of the buffer gas cell with a hole punctured for the insertion of the water fill line. The kapton surface seals the back of the cell for a stronger forward beam, while limiting the heat load from a room temperature fill line, and resisting ice formation allowing for continuous and consistent operation with water for over 10 hours. . . . .	22
3.6 Theoretically derived buffer gas beam properties of interest given the physical dimensions of our cell in particular: $d_{aperture} = 9$ mm. A) $\gamma$ extraction ratio, dotted red line indicates $\gamma = 1$ where hydrodynamic entrainment begins. B) Number density of buffer gas species within the experimental cell, given an enclosed back wall. The density of target species introduced should stay under 1% of the buffer gas density for other properties to hold. C) Number of collisions a target species particle would expect before extraction out of the cell, the dotted red line indicates 100 collisions before extraction, when rotational degrees of freedom are characteristically thermalized. . . . .	27
3.7 Fitted linear behavior of H <sub>2</sub> O entrained in a Ne buffer gas beam 30 cm from cell aperture. The onset of hydrodynamic entrainment seems to occur around 20 SCCM up through 60/65 SCCM where the H <sub>2</sub> O extracted into the beam has a clear linear form of $(9.2 \times 10^8 \text{ cm}^{-3}/\text{SCCM})f - 2 \times 10^{10} \text{ cm}^{-3}$ . . . . .	28
3.8 Projected beam densities with a Ne flow rate of 30 SCCM with various distances of interest within the chamber. Beam densities shown are without throttling of the H <sub>2</sub> O flow valve. . . . .	30
3.9 Projected beam densities at the trap center over various nominal Ne flow rates and smallest skimmer aperture size. Beam densities shown are without throttling of the H <sub>2</sub> O flow valve. . . . .	31
3.10 . . . . .	34
3.11 . . . . .	35
3.12 RGA contrast . . . . .	36

3.13	Fluorescence decays of loaded $\text{Be}^+$ ions exposed to a cold water beam with an inline shutter either opened, in green ( $\tau = 7.23 \times 10^{-3}\text{s}$ ) or closed, in blue ( $\tau = 6.37 \times 10^{-2}\text{s}$ )	37
3.14	Fluorescence decays of loaded $\text{Be}^+$ ions exposed to a cold water beam with an inline shutter opened, in green ( $\tau = 5.37 \times 10^{-2}\text{s}$ ) or closed, in red ( $\tau = 7.59 \times 10^{-3}\text{s}$ )	37
4.1	Electronic structure of ${}^9\text{Be}^+$ . Laser cooling is done with 313 nm light tuned from the ${}^2\text{S}_{1/2}$ to ${}^2\text{P}_{3/2}$ state.	39
4.2	Set of ion images taken at various 313 nm powers with an algorithm that identifies individual ions	40
4.3	Individual ions identified from images in figure 4.2. Integrated fluorescence counts shown for each image as well as averaged value in brackets.	41
4.4	P-state fraction curve fitted to incident laser power at a fixed detuning of $\omega_l = \omega_0 - \Gamma/2$ .	42
4.5	Image of the single laser, dual ablation set up. The 1064 nm YAG pulse is split into two paths, and recombined such that they proceed through the same focusing element into the chamber to hit two different targets.	44
4.6	TOF trace of simultaneous $\text{Be}^+$ and $\text{C}^+$ ablation loading averaged over 10 shots. A soft A-ramp is applied after loading, ejecting any unintentionally loaded $\text{Cn}^+$ clusters.	45
5.1		51
5.2		52
6.1		56
6.2		57
6.3		57
6.4		58

6.5	.....	58
6.6	.....	63
7.1	A linear dependence on the rate constant for reaction 7.1 as a function of P state excitation. $k = (6 \pm 1) \times 10^{-11}P + (-0.03 \pm 0.16) \times 10^{-11}$ .....	67
7.2	Shared fitting of trapped products with 14% p-state excitation. ....	67
7.3	Shared fitting of trapped products with 14% p-state excitation. ....	68
7.4	TOF traces for data taken with 14% p-state excitation at 0s and 200s showing no products at 0s, but distinct peaks for reaction products $\text{BeH}^+$ , $\text{BeOH}^+$ , and $\text{O}_2^+$ . ....	68
7.5	TOF traces for data taken with 14% p-state excitation at 0s and 200s showing no products at 0s, but distinct peaks for reaction products $\text{BeH}^+$ , $\text{BeOH}^+$ , and $\text{O}_2^+$ . ....	69
8.1	Gasses .....	71
8.2	RGA showing purity of $\text{CO}_2$ introduced into chamber. Ratios of $\text{CO}_2$ peaks at $m/z = 12, 16, 28$ , and 44 in agreement with table 8.2, with no conclusive evidence of contamination by any other gas. ....	74
8.3	TOF trace of laser-cooled $\text{Be}^+$ reacting with $\approx 1 \times 10^{-8}$ Torr $\text{CO}_2$ introduced via leak valve for 50 seconds. ....	75
8.4	Integrated ion signal of individual TOF traces normalized by $\text{Be}^+$ fluorescence at various $\text{CO}_2$ exposure times. ....	76
8.5	TOF trace of laser-cooled $\text{Be}^+$ and $\text{C}^+$ reacting with $\approx 1 \times 10^{-8}$ Torr $\text{CO}_2$ introduced via leak valve for 40 seconds. ....	77
8.6	Integrated ion signal of individual TOF traces normalized by total ion signal excluding $\text{Be}^+$ at various $\text{CO}_2$ exposure times. ....	77
8.7	$\text{C}^+$ and $\text{Be}^+$ loaded into the trap is reacted with $\text{H}_2\text{O}$ introduced from the beam. The gate valve is closed after 10 seconds and $\text{CO}_2$ is introduced via leak valve so that the $\text{COH}^+$ is titrated into $\text{CO}_2\text{H}^+$ . ....	79



## PREFACE

## CURRICULUM VITAE

- 2009 – 2013                    B.S. in Physics, University of Maryland (UMD), College Park, Maryland
- 2013 – Present                Ph.D. student in Physics, University of California, Los Angeles (UCLA).

# **CHAPTER 1**

## **Introduction**

This thesis chronicles the experimental work done to realize an apparatus for cold ion-molecule chemistry of species of astrochemical interest, and attempts to understand chemistry in general along the way.

### **1.1 Thesis Outline**

## CHAPTER 2

### Chemical Rate Constants

When describing the rates of chemical reactions, it is usually described by the order of reaction. Usually the order of reaction is dependent on the sum of the order the constituents contribute to the reaction. For example, if we have a reaction of:



The appearance of products  $[C]$  and  $[D]$  is directly equivalent to the disappearance of  $[A]$  and  $[B]$ . The rate constant is then defined as:

$$k = \frac{\Gamma}{[A]^m[B]^n}$$

Where  $k$  is the rate constant, and  $\Gamma$  is the reaction rate in time. The order of the reaction is defined as the sum of the constituent power dependencies  $m + n$ . For gas phase reactions, the dependencies are usually  $= 1$ , as it is unlikely to have multiple collisions during a single reaction lifetime. For bi-molecular reactions that we are exploring, we would expect the rate to be a second order rate, which gives a solution of:

$$\frac{[A]}{[B]} = \frac{[A]_0}{[B]_0} e^{([A]_0 - [B]_0)kt}$$

Where the rate constant  $k = 1/([A]_0 - [B]_0)t$ . In reality, we are only trapping a few ions in the trap while flooding the chamber with neutral reactants from either the beam or a leak valve. In either case, the concentration of one reactant is held effectively fixed, while the

other is depleted. From here, we yield the pseudo-first-order reaction rate constant, which takes a second order reaction and simplifies it to a first order rate equation.

$$\frac{d[A]}{dt} = -k[B][A]$$

$$[A] = [A]_0 e^{-k[B]t} \quad (2.1)$$

Where  $[A]$  and  $[B]$  are the concentrations of the scarce and flooded reactants respectively. We can readily identify the rate constant  $k = 1/[B]\tau$ , with dimensions  $\text{cm}^3\text{s}^{-1}$ . The reactions discussed in this thesis are exclusively of the pseudo-first-order.

## 2.1 Average Dipole Orientation Theory (ADO)

Adiabatic capture theory is a study of the long range potentials between particles to yield a reaction rate constant. This is easily done for many potentials, such as the ion and induced-dipole interaction (Langevin), but is more difficult when considering potentials with another degree of freedom; in particular, we would like to consider the ion-dipole interaction. Unlike the Langevin interaction, the ion-dipole term has an angular term defined with respect to the inter-molecular axis. A few approximations are taken to give an average dipole orientation theory pioneered and expanded on by Su and Bowers.[\[47, 48\]](#) This can also be extrapolated to include quadrupole interactions.[\[49\]](#)

### 2.1.1 General Treatment of Adiabatic Capture Theory

A general method of calculating the rate constant of two particles with a given potential, finding the collisional cross section, which is then averaged over a velocity distribution to find the rate constant.[\[59\]](#) Starting with the attractive potential, we find that it is a summation

of interactions with coefficients  $C_n$  and  $r$  dependence  $n$ .

$$V(r) = \sum_n -\frac{C_n}{r^n} \quad (2.2)$$

In the center of mass frame, we see that

$$V_{eff} = \frac{l^2}{2\mu r^2} - \sum_n \frac{C_n}{r^n} \quad (2.3)$$

if  $n > 2$ , we can derive the capture cross-section and rate constant as follows. First, we find the position  $r_0$  corresponding to the maximum of the effective potential, which is the maximum of the centrifugal barrier.

$$\begin{aligned} \frac{\partial V_{eff}(r_0)}{\partial r} &= 0 \\ \therefore r_0 &= \left( \frac{n\mu, C_n}{l^2} \right)^{1/n-2} \end{aligned}$$

Substituting  $r_0$  back into equation 2.3, we find the maximal value of the effective potential:

$$V_{eff}(r_0) = \left( \frac{l^2}{\mu} \right)^{\frac{n}{n-2}} \frac{n-2}{2n} (nC_n)^{-\frac{2}{n-2}} \quad (2.4)$$

This then defines the energy necessary for a collision, for if  $E_{col}$  exceeds  $V_{eff}(r_0)$ , the reactants will be able to surmount the centrifugal barrier and collide. Thus, we may define the maximum value for the angular momentum  $l$  and the impact parameter  $b$ .

$$\begin{aligned} l_{max} &= (\mu n)^{1/2} (C_n)^{1/n} \left( \frac{2E_{col}}{n-2} \right)^{\frac{n-2}{2n}} \\ b_{max} &= \frac{l_{max}}{\mu v} \end{aligned}$$

We can then define a collision cross section dependent on the collision energy:

$$\begin{aligned}\sigma(E_{col}) &= \pi b_{max}^2 \\ &= \frac{\pi}{2} n \left( \frac{2}{n-2} \right)^{\frac{n-2}{2}} \left( \frac{C_n}{E_{col}} \right)^{\frac{2}{n}}\end{aligned}$$

Integrating the collision cross section with a Maxwell Boltzmann distribution yields a generalized rate constant as a function of temperature and  $n$ .

$$k(T) = \int_0^\infty v f(v) \sigma(v) dv \quad (2.5)$$

$$= \sqrt{\frac{2\pi}{\mu}} n \left( \frac{2}{n-2} \right)^{\frac{n-2}{2}} C_n^{2/n} (k_B T)^{\frac{n-4}{2n}} \Gamma \left( 2 - \frac{2}{n} \right) \quad (2.6)$$

### 2.1.2 Ion-Dipole Interaction

The Langevin term of the ion and ion-induced dipole interaction is as follows:

$$V_L(r) = -\frac{\alpha q^2}{2r^4} \quad (2.7)$$

In the case of the ion-dipole interaction:

$$V_D(r, \theta) = -\frac{q\mu_D}{r^2} \cos(\theta) \quad (2.8)$$

The method outlined in section 2.1.1 finds the rate constant by dealing with a two body problem only needing to consider the  $r$  degree of freedom. The inclusion of the  $\theta$  term complicates this, but to first order, we can parameterize it as a function of  $r$ . What we want to achieve is to write down the potential as such:

$$\begin{aligned}V(r) &= -\frac{\alpha q^2}{2r^4} - \frac{q\mu_D}{r^2} \cos(\bar{\theta}(r)) \\ \bar{\theta} &= \frac{\int \theta P(\theta) d\theta}{\int P(\theta) d\theta}\end{aligned} \quad (2.9)$$

Where  $P(\theta)$  is the probability of finding the dipole at  $\theta$ . To determine the average orientation of the dipole, we consider the following cases:

1.  $P(\theta)$  is inversely proportional to the angular velocity:

$$P(\theta) \propto 1/\dot{\theta}$$

2. An orientation has a probability weighted by the circumference of an angle:

$$C = 2\pi l \sin(\theta)$$

$$P(\theta) \propto \sin(\theta)$$

The angular probability is proportional to both effects:

$$P(\theta) \propto \frac{\sin(\theta)}{\dot{\theta}} \quad (2.10)$$

We can relate the angular velocity to the angular kinetic energy and the total energy in the system:

$$\begin{aligned} KE_{rot} &= \frac{1}{2} I \dot{\theta}^2 \\ E_{tot} &= KE_{rot} + V_D \end{aligned} \quad (2.11)$$

Redefining equation 2.10 with equation 2.11, we find:

$$P(\theta) \propto \frac{\sin(\theta)}{\sqrt{E_{rot} - V_D}} \quad (2.12)$$

Combining equations eqs. (2.12) and (2.9) yields a total averaged dipole orientation.

$$\bar{\theta} = \frac{\int \frac{\theta \sin(\theta) d\theta}{\sqrt{E_{rot} + q\mu_D/r^2 \cos(\theta)}}}{\int \frac{\sin(\theta) d\theta}{\sqrt{E_{rot} + q\mu_D/r^2 \cos(\theta)}}} \quad (2.13)$$

From here, two situations arise:

1.  $E_{rot} = E_1 < \frac{q\mu_D}{r^2}$ : There is not enough rotational energy to overcome the dipole locking. The solution is oscillatory, but  $\theta$  has an  $r$  dependent bound. We let the maximal capture angle be defined as  $K$ .

$$E_1 = -\frac{q\mu_D}{r^2} \cos(K)$$

When substituted into equation 2.13, we find:

$$\bar{\theta}_1 = \frac{\int_0^K \frac{\theta \sin(\theta) d\theta}{\sqrt{\cos(\theta) - \cos(K)}}}{\int_0^K \frac{\sin(\theta) d\theta}{\sqrt{\cos(\theta) - \cos(K)}}}$$

After some math (something something integration by infinite series) and get a result of:

$$\bar{\theta}_1 = \frac{2\sqrt{2}A}{\sqrt{1 - \cos(K)}}$$

where  $A \equiv \int_0^{\pi/2} \frac{a^2 \cos(\phi)^2 d\phi}{\sqrt{q - a^2 \sin(\phi)^2}}$

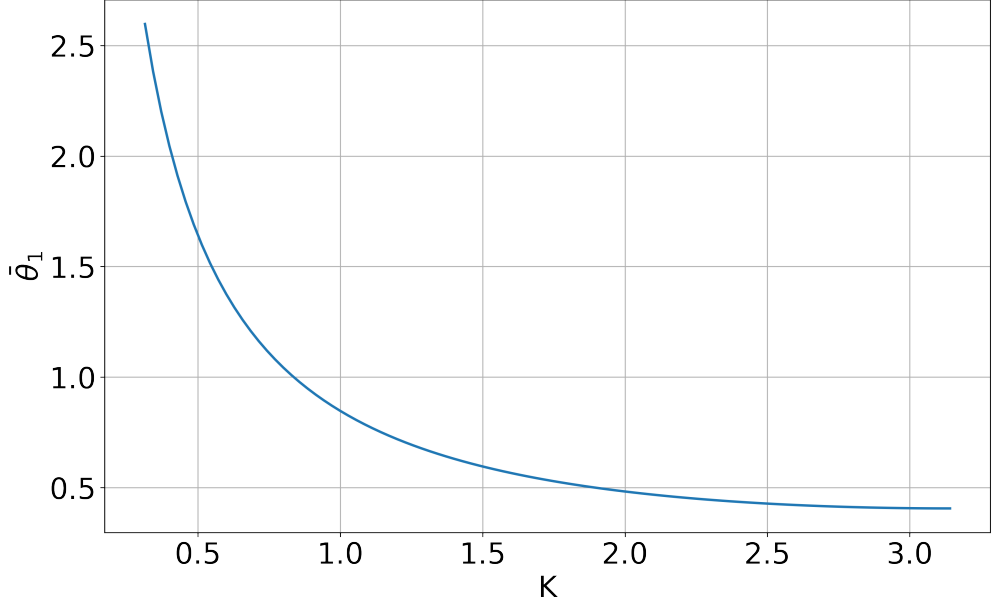


Figure 2.1: Rough plotting of  $\theta_1$  as a function of maximum angle  $K$ . The behaviour is as expected, the greater the maximal capture angle, the more  $\theta_1$  tends towards 0.

2.  $E_{rot} = E_1 > \frac{q\mu_D}{r^2}$ : The rotational energy is enough to overcome the dipole locking and  $\theta$  can swing around in a complete circle

$$\bar{\theta}_2 = \frac{\int_0^\pi \frac{\theta \sin(\theta) d\theta}{\sqrt{E_2 + q\mu_D/r^2 \cos(\theta)}}}{\int_0^\pi \frac{\sin(\theta) d\theta}{\sqrt{E_2 + q\mu_D/r^2 \cos(\theta)}}} \quad (2.14)$$

We no longer have bounds on the angles the dipole is allowed over, but the behavior is still dependent on the strength of the internal energy and dipole force.

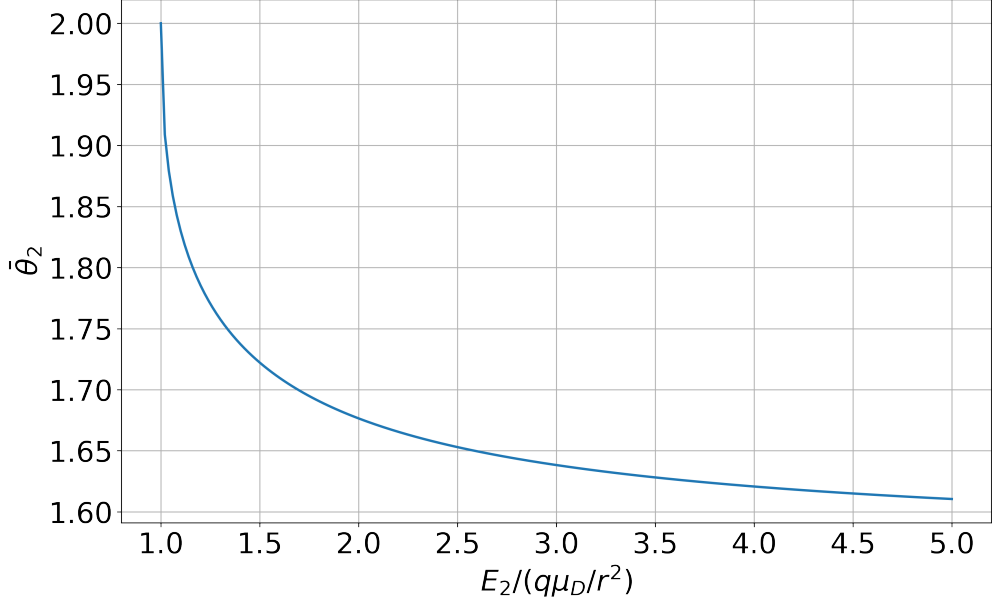


Figure 2.2:  $\theta_2$  as a function of the ratio of rotational energy and the monopole-dipole term. The low ratio behavior is not immediately obvious, but the greater the ratio between the rotational energy and monopole-dipole term, the more  $\theta_2$  tends towards  $\pi/2$ .

Let's say we have the forms for  $\bar{\theta}_1$  and  $\bar{\theta}_2$ , we want to write down the full form of  $\theta$ . We can combine the two weighted by the probability of each as a function of internal energy.

$$\bar{\theta}(r) = \bar{\theta}_1(r)F_1 + \bar{\theta}_2(r)F_2$$

Where these weightings are found via:

$$P(\epsilon)d\epsilon = \frac{1}{k_B T} e^{-\frac{\epsilon}{k_B T}} d\epsilon$$

For diatomics, we can use:

$$\epsilon = \frac{J(J+1)\hbar^2}{2I}$$

We can then use equation 2.5 and get a cross section and rate constant. The form is similar to that of just a Langevin term, but now with a dipole interaction term added onto

it. All of the terms aside from  $C$  come from the integration over a Boltzmann distribution, where then averaging over the angles is wrapped up into the  $C$  term.

$$k_{ADO} = \frac{2\pi e}{\sqrt{\mu}} \left( \sqrt{\alpha} + C\mu_D \sqrt{\frac{2}{\pi k_B T}} \right) \quad (2.15)$$

The dipole locking constant ( $C$ ) can be numerically solved by iteratively integrating over combinations of  $\mu_D$  and  $\alpha$ .[47][51]

## 2.2 Statistical State Counting

$$E_{int} = \omega_e \left( v + \frac{1}{2} \right) - \omega_e x_e \left( v + \frac{1}{2} \right)^2 + B_e j(j+1) \quad (2.16)$$

Where  $\omega_e$  is the vibrational constant,  $\omega_e x_e$  is the anharmonic vibrational constant,  $B_e$  is the rotational constant, and  $v, j$  are vibrational and rotational quantum numbers respectively. You can count how many states there are up to a maximum energy input and compare states to see which product channel is preferred statistically.

To get a more accurate counting, we should be comparing the integrated states including the energy taken away by the other reactant.

$$\int_0^{p_{max}} 4\pi p^2 n(p) dp \quad (2.17)$$

where  $n(p)$  is the number of internal states allowed with momentum  $p$

## CHAPTER 3

### The Cryogenic Buffer Gas Beam (CBGB)

To reach reaction temperatures around 10K from a beam of molecules with trapped ions, a cryogenic buffer gas beam (CBGB) of neon with entrained water is employed. Numerous other methods of creating cold beams of molecules exist, from Zeeman decelerators [31], to Stark decelerators. CBGB's in particular have the benefit of being species agnostic, where the resultant beam properties are not dependent on the target species at hand, rather, the buffer gas species.

By holding a cell filled with a noble gas above its vapor pressure, a volume of gas can be held at cryogenic temperatures. Other species of molecules or atoms may be introduced into the buffer gas cell via ablation, fill line, etc. The target species particles are then sympathetically cooled via collisions with the cold buffer gas. An aperture at one end of the cell allows for the extraction of the buffer gas and entrained target species into a ballistic beam. Holding the buffer gas cell temperature to above 17 K for neon, and 4 K for helium, in high vacuum allows us to accumulate an appreciable stagnation number density within the cell to produce a beam of entrained target particles.

The properties of interest are a function of the flow regime of the beam, which is determined by the choice of gas, its flow rate, and the dimensions of the cell it is held in. It's convenient to use the Reynolds number at the aperture to characterize the flow regime, which can be written as:

Add  
ci-  
ta-  
tions  
for  
de-  
cel-  
er-  
a-  
tors



Figure 3.1: Schematic of target species entrainment within a buffer gas beam cell. With high densities of buffer gas particles, an introduced target species undergoes collisions with the buffer gas such that it cools. At high enough densities, flow dynamics cause the target species to become entrained in the buffer gas flow and are carried out of the cell with greater efficiency.

$$\begin{aligned} Re &\approx \frac{2d_{aperture}}{\lambda} \\ &\approx \frac{8\sqrt{2}\dot{N}\sigma}{d_{aperture}\bar{v}} \end{aligned} \quad (3.1)$$

Where  $d_{aperture}$  is the diameter of the aperture and  $\lambda$  is the mean free path of the buffer gas particles.[22] When the Reynolds number is low,  $Re < 1$ , we find that there are on average  $> 1$  collisions at the aperture, meaning the particles escape with little to no interactions with other particles and is called the effusive regime. At high Reynolds numbers,  $Re > 100$ , in the supersonic regime, there are many collisions and forward velocity boosting as well as internal velocity distribution narrowing occurs. In between, we find the intermediate regime, where we observe the onset of hydrodynamic entrainment of target species with mild forward velocity boosting. In all cases, the gasses inside the cell at thermal equilibrium follow the Maxwell-Boltzmann distribution.

$$f(v) = \left(\frac{m}{2\pi kT}\right)^{3/2} 4\pi v^2 e^{-\frac{mv^2}{2kT}} \quad (3.2)$$

Where the mean velocity is:

$$\bar{v} = \sqrt{\frac{8k_B T}{\pi m}} \quad (3.3)$$

The goal for our beam is three fold, to produce a **slow, dense, localized** beam of our target species that can make it down into the ion trap region. The velocity and density of the target species are both related to the flow regime of the buffer gas, and to reach our goal, it's ideal for us to aim for a beam that operates within the intermediate regime, between effusive and supersonic. Producing a localized beam ensures that we are introducing the minimal unwanted gas load into the ion trap chamber, and that we may quickly and reliably shutter the beam to start and stop the chemical reactions. In the following sections, we will discuss the design of the apparatus and characterization of the beam density, extraction, forward velocity, and shuttering.

### 3.1 Design

The CBGB apparatus design has various stages, a room temperature 300 K outer aluminum vacuum chamber, onto which a Pulse Tube Refrigerator (PTR) is mounted, an aluminum radiation shield mounted to the 40 K PTR cooling stage, and an inner copper cryopumping shield and experimental cell connected to the 4 K PTR cooling stage. Connected to the vertical vacuum chamber, a "stem" region protrudes out from the beam side as seen in figures figs. 3.2 and 3.3 where a large Agilent Varian-V 551 turbo pump evacuates the entire volume. The beam comes out of the experimental cell and shield, through a set of apertures, into the stem region where skimmers and shutters are mounted to manipulate the beam.

A Cryomech PT415 PTR with a remote head option was attached to the top plate of the vacuum chamber with a large bellows mount to isolate the chamber from the mechanical vibrations caused by the PTR motor head. The chamber was pumped down to normal operating pressures, where then 4 retaining screws were tightened to just above the bellows' compressed height. This maintains mechanical decoupling between the outer vacuum

chamber and the PTR while running.

We want to minimize the mechanically coupling onto the PTR due to the fragility of the pulse tube walls; small amounts of force applied onto a mechanically connected component would risk torquing the walls to break. Thus, all components inside the CBGB are mechanically connected to the top plate of the vacuum chamber via 8-32 stainless steel (SS316) threaded rods. Thermal connections are made with copper braids welded onto L-shaped brackets that mount between platforms secured to the PTR cooling stages, and the shields.

Not only are all the inner shields connected to the top plate, but so are the feedthroughs including gas fill lines. This ensures that any and all connections made into the CBGB are not disturbed when opening the outer vacuum chamber to expose the inner components.

The design of the shields themselves is informed by the choice of buffer gas species. Commonly used buffer gas species are helium and neon, while helium provides a slower beam, it is more technically challenging to implement. The main technical difference comes from the cryopumping requirements; where neon only needs surfaces to be held at 17 K to continually cryopump, helium requires (coconut) activated charcoal held at 4 K or lower. Aside from the difficulty of getting surfaces to 4 K these volumes of charcoal can become saturated and require purging, limiting one's operating time (few hours). On the other hand, neon ice formed on the 17 K surface will act as a cryopump for more neon gas, allowing for many hours of continuous operation with no appreciable build up of background gas. Our experiment uses neon as a buffer gas for its technical simplicity, the lower achievable temperature with the helium does not yield dramatic gains in the final reaction temperature.

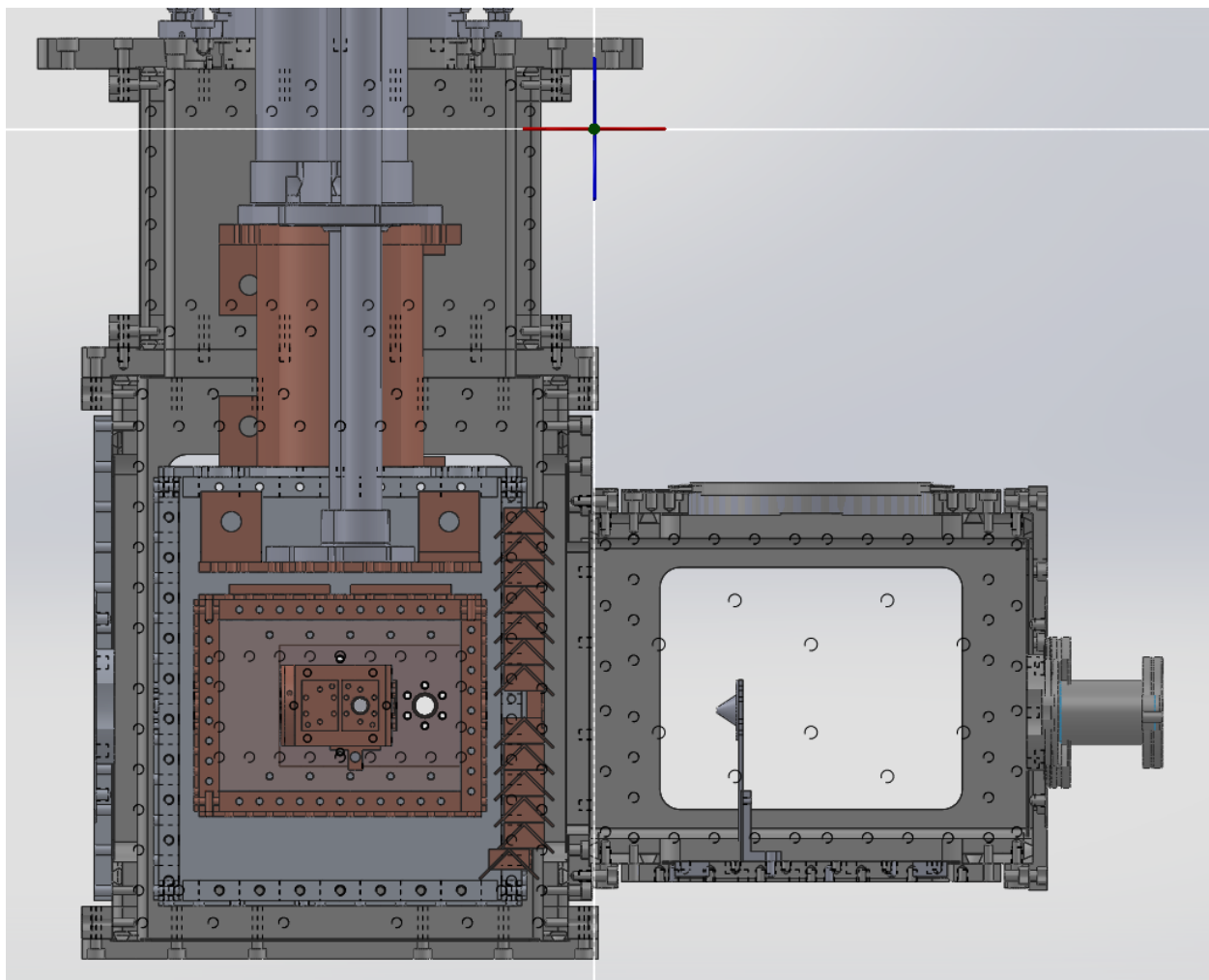


Figure 3.2: Cross sectional view of CBGB in solidworks. Components include copper sheath for PTR, aluminum radiation shield with chevron baffles, copper shield and experimental cell, and skimmer mounted in stem chamber. The baffles allow for gas to flow into the cold region of the beam apparatus, while preventing 300 K black body radiation from hitting the inner shield and cell.

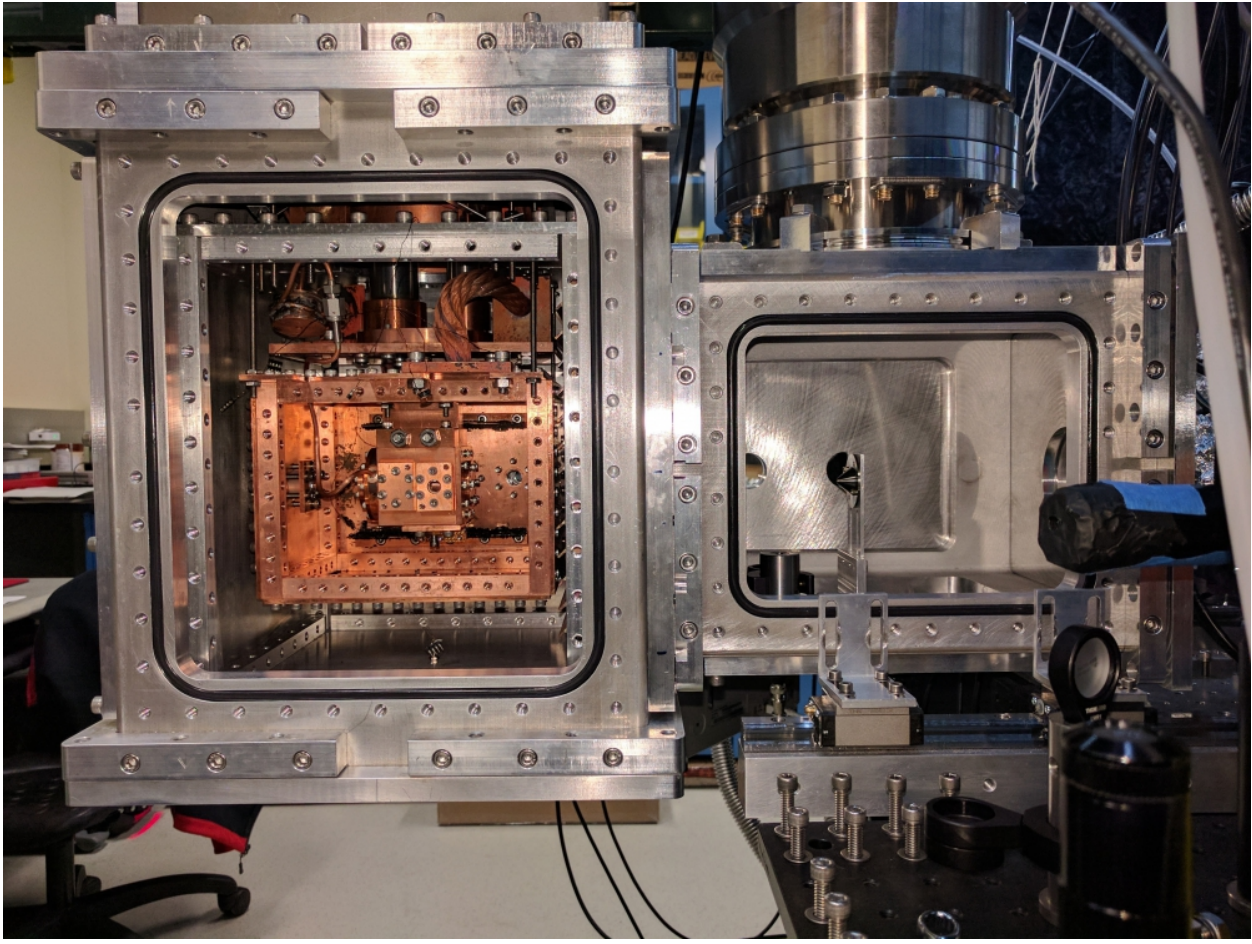


Figure 3.3: Cross sectional view of CBGB with side walls removed from the outer vacuum chamber, 40 K aluminum radiation shield, and inner 4 K cryopumping shield exposing the inner experimental cell. A skimmer is mounted in the stem region.

### 3.1.1 Heat Load and Thermal Conductivity

To produce a beam of cold particles, various components need to be held within specific temperature ranges to ensure proper operation. Considering neon as the buffer gas species of choice, we maintain the experimental cell at 20 K to prevent the neon from freezing to the walls and maintain a high stagnation density that allows for tuning of the flow regime. Conversely, we need the cryopumping shield surrounding the experimental cell to maintain

a temperature  $< 17$  K so that the neon that escapes the cell is readily captured, as the turbo connected to the stem chamber cannot keep up with the gas load. A lack of proper cryopumping results in high densities in the chamber, which scatters the beam.

The PTR 40 K cooling stage has 40 W of cooling power, while the lowest 4 K stage has only 4 W. The low cooling power of the lowest stage means that extra care is needed to minimize the heat transfer to the stage from the higher temperature regions including black body radiation and conducted heat from high temperature surfaces.

Material choices used in the CBGB are dictated by their thermal conductivity down to the temperature ranges of interest. At room temperature, thermal conductivity ( $k$ ) of a material is dominated by transfer of energy via phonons through the material. In this regime, different alloys and purities of a material do not greatly affect the conductivity. But once we enter cryogenic temperatures, the conductivity is dominated by electron motion through the material, meaning that purer samples have fewer imperfections to scatter off of, yielding higher conductivities.

Al 6061 was chosen for the radiation shield for its thermal conductivity ( $k_{Al6061}(T = 40$  K) = 70 W/(m K)[?]), ease of machining, as well as lightweight properties. The thermal mass of the aluminum shield coupled with its relatively lower thermal conductivity (compared to Cu 10100) means the cool down of this region limits the cool down process to 6 hr until at workable temperatures. The face of the aluminum shield coinciding with the outgoing buffer gas beam was fitted with a set of stacked chevron baffles as seen in figure 3.2. The baffle design blocks stray light from entering the radiation shield, while enabling gas to pass from the enclosed shields into the stem region, preventing high density regions from forming and scattering the beam. Conversely, the baffles allow for gas within the stem region to reenter the cryogenic shields and facilitate cryopumping of stray particles.

The copper region contains the experimental cell, enclosed by a copper shield that acts as a cryopumping surface at the appropriate temperatures. At cryogenic temperatures, it's convenient to characterize the conductivity of a copper with the residual resistance ratio ( $RRR = \frac{R(T=295\text{ K})}{R(T=4\text{ K})}$ ), where  $R(T)$  is the measured resistance at temperature  $T$ , which can be

related to the thermal conductivity with the Wiedemann-Franz Law.<sup>[?]</sup> Cu 10100, or oxygen free copper, was chosen for these components for its high thermal conductivity through to 4 K,  $RRR = 2000$ ,  $k_{Cu10100}(4 \text{ K}) = 10^4 \text{ W}/(\text{m K})$  compared to <sup>[?]</sup>.

Because it is heat sunk into the same cooling stage as the experimental cell, the copper shield does not act as a radiation shield for it does not redirect the heat load away from the experimental cell's cooling surfaces. For the experimental cell to hold an appreciable vapor pressure, while the thermally linked shield acts as a cryopumping surfaces, the two components will need to held at different temperatures. The experimental cell is held at a higher temperature than that of the cryopumping shield with a resistive heater, which is monitored and controlled with a temperature sensor diode (DT-670) and a Lakeshore controller (Model 325). A SS316 ( $k_{SS316}(T = 40 \text{ K}) \approx 7 \text{ W}/(\text{m K})$ ) stand off is used to create a poor thermal bridge between the two regions, allowing for a constant thermal gradient.

The main heat loads onto the system are those from the black body radiation, as well as the stainless steel rods supporting the shields from the top mounting plate. The temperature over the system may be determined by solving the heat/diffusion equation given proper boundary conditions.

$$\frac{\partial u(x, t)}{\partial t} = D \nabla^2 u(x, t) \quad (3.4)$$

To first order, we use Fourier's Law to approximate the conductive heat loads through individual pieces.

$$\dot{Q} = \frac{A}{l} \int_{T_1}^{T_2} k(T) dT \quad (3.5)$$

Where  $\dot{Q}$  is the rate of heat transfer,  $A$  is the cross sectional area of the component in question,  $l$  is the length of the component, and  $k(T)$  is the thermal conductivity as a function of temperature. For simplicity, we approximate the conductance at the expected

steady state temperature.

$$E = \sigma T^4 \quad (3.6)$$

This is the equation for the energy of BBR

$$\lambda_{max}T \approx 2900\mu \text{ m K} \quad (3.7)$$

This is the approximate peak wavelength emitted by a body given the temperature.

$$\dot{Q} = \sigma A(T_1^4 - T_2^4) \frac{\epsilon_1 \epsilon_2}{\epsilon_1 + \epsilon_2 - \epsilon_1 \epsilon_2} \quad (3.8)$$

Considering two surfaces, we find this as the form of the power incident as a function of both surface emissivities.



### 3.1.2 Gas Fill Lines

To have a functioning beam, we need to introduce both the buffer gas as well as the target species gas from room temperature without over burdening the cooling stage, or plugging the fill lines. The buffer gas fill line is made of thin walled SS316, minimizing the thermal connection between the room temperature mounting and the cold experimental cell. It is thermally anchored to the 40K cooling stage and then brazed onto a plate that mounts to the experimental cell. To avoid local freezing of the buffer gas, the tubing must avoid cryopumping shield as contact.

More care must be taken for the design of the water fill line, as it cannot make contact with any mildly cooled metal surface for fear of local freezing. The mating of the fill line to the experimental cell must also prevent excessive heat loads onto the cell while still enclosing the back side to preserve beam flux. With the design help of David Patterson, we utilize a thick walled 1/8" copper tube, with the tip bent at 90°, that enters from the bottom of the

CBGB (figure 3.4), through the shields, into the back of the experimental cell. The fill line can be manipulated from the bottom of the chamber and the insertion depth into the cell can be adjusted before pump down. By slathering the o-ring at the bottom of the chamber with silicon vacuum grease, one may also adjust the tubing in situ, but the CBGB should be gated off from the rest of the experiment.

Leaving the back of the cell open eliminated conductive heat transfer between the fill line and the cell, but did not allow for a reliable beam. Ice readily formed on the nearby copper surfaces and slowly closed the back opening, decreasing the effective  $A_{aperture}$  of the cell, thus changing the flow properties. The back was replaced with a 0.001" film of kapton with a cross cut into the middle for the fill line as seen in figure 3.5. The poor thermal conductivity of kapton (0.5 W/(m K)) ensures minimal conductive heat load to the cell, prevents ice from forming, while also closing the back of the cell. The beam may be run continuously with water entrained in the neon buffer gas for over 10 hours without any change in beam properties. Collisions with buffer gas particles within the cell transferring heat between the fill line and cell walls added  $< 0.05\text{W}$  of heat load. Solving Fourier's Law in cylindrical coordinates (3.9), we find that the heat load through the kapton is only 0.019 W.

$$\dot{Q} = \frac{2\pi k l (T_1 - T_2)}{\ln(r_2 - r_1)} \quad (3.9)$$



Figure 3.4: The water fill line, sealed by an ultratorr fitting and heated by nichrome wire. A shut off valve and vernier valve are used to regulate the flow of water into the buffer gas cell.

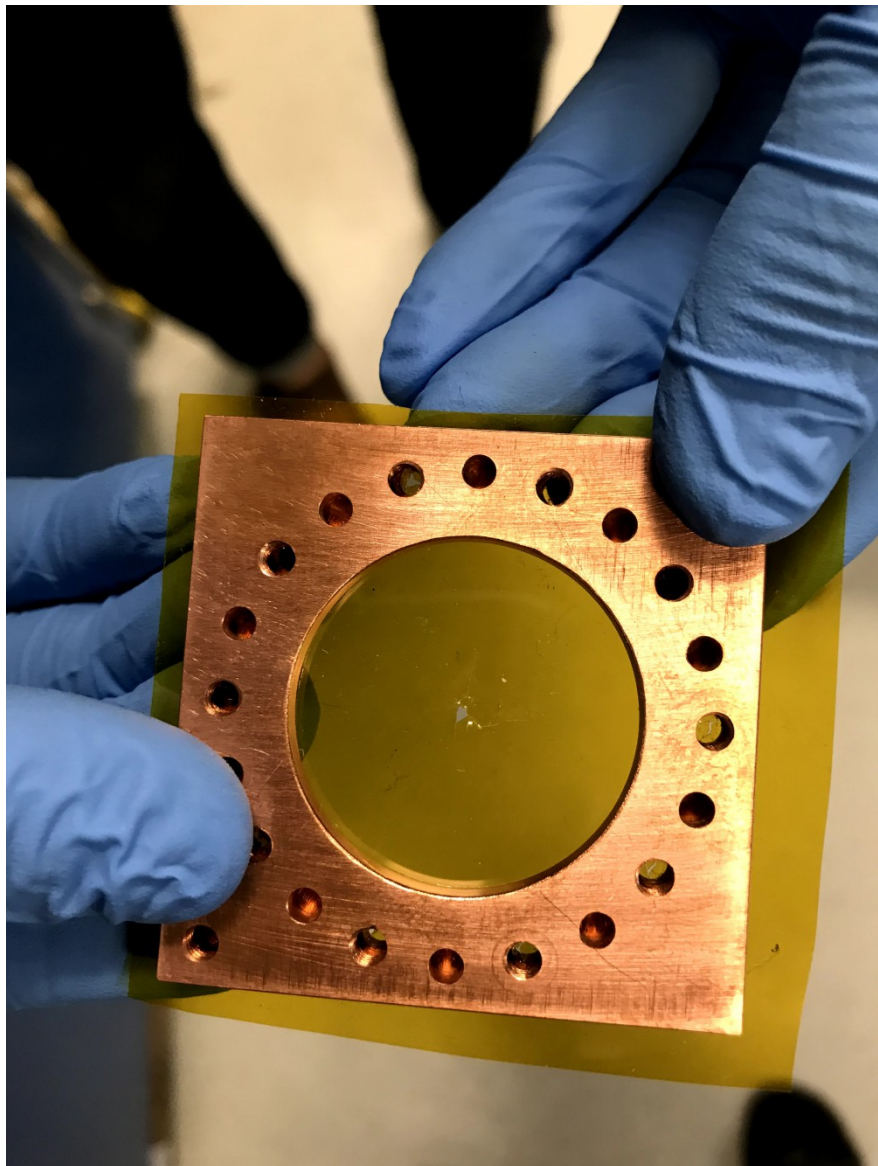


Figure 3.5: A kapton film serves as the back wall of the buffer gas cell with a hole punctured for the insertion of the water fill line. The kapton surface seals the back of the cell for a stronger forward beam, while limiting the heat load from a room temperature fill line, and resisting ice formation allowing for continuous and consistent operation with water for over 10 hours.

### 3.2 Beam Density and Extraction

We need to have a fairly dense beam of our target species to reach the ion trap center in order to get a reasonable signal to noise of the cold molecule reaction as opposed to the warm background reactions. A dense beam coupled with good cryopumping ensures that the signals seen are primarily, if not solely due to the introduction of the cold beam.

The downstream properties of a beam all start with the buffer gas stagnation density within the experimental cell. The stagnation density is the steady state buffer gas density that is determined by the physical dimensions of the cell, including the aperture, and the gas throughput, or number flow rate going in. Experimentally, it's preferable to use volumetric flow rates when operating the apparatus, so for calculations, that needs to translate to number flow rate using the ideal gas law:

$$\dot{N} = \frac{Pf}{k_B T}$$

where  $P$  is pressure and  $f$  is the volumetric flow rate, this translates to about  $4 \times 10^{17}$  particles/s<sup>-1</sup> for 1 SCCM of gas flow. By solving for the number density in the flow out of an aperture with molecular flow, we find that the stagnation density within the cell can be shown as:

$$C_{ap} = A \frac{\bar{v}}{4}$$

$$n_b = \frac{4\dot{N}}{A_{aperture} \bar{v}} \quad (3.10)$$

In general, buffer gas beams operate with stagnation densities around  $10^{15} - 10^{17}$  cm<sup>-3</sup>. Outside of the cell, we can describe the density of the beam as a function of distance. [33]

$$n(z) = \frac{n_0}{2} \left( 1 - \frac{z}{\sqrt{z^2 + a^2}} \right) \quad (3.11)$$

Where  $z$  is the distance from the aperture into the vacuum side,  $n_0$  is the initial number density,  $a$  is the radius of the aperture. In the far-field, this goes to:

$$n(z) = \frac{n_0 a^2}{4z^2}$$

But there is something that we must consider, that is that we aren't seeing the full aperture while we are at all locations, we are actually seeing an appended area due to the inclusion of apertures and skimmers in the way. While only  $n_0$  is only dependent on the aperture size of the cell,  $n(z)$  will have a set value defined by the smallest aperture in the beam path. For us, although our cell aperture is  $\approx 9$  mm in diameter, we have multiple apertures and skimmers in the way, the smallest of which is a skimmer from Beam Dynamics with a diameter of 2 mm.

Sympathetic cooling occurs through collisions between the hot target species being introduced and the cryogenic buffer gas particles. We may consider each hard sphere collision to transfer heat from the hot target species ( $T_s$ ) to the cold buffer gas at constant temperature ( $T_b$ ).

$$\Delta T_s = -\frac{T_s - T_b}{k}$$

Where  $k \equiv \frac{(m_b + m_s)^2}{2m_b m_s}$ . For the  $N^{\text{th}}$  collision, we can write the change in temperature:

$$T_s(N) - T_s(N-1) = -\frac{T_s(N-1) - T_b}{k}$$

For large values of  $N$ , where the change in temperature becomes small, we can turn the discrete equations into a differential form.

$$\frac{dT_s(N)}{dN} = -\frac{T_s(N) - T_b}{k}$$

Which we can solve with the condition that  $T_s(0) = T_0$

$$\begin{aligned} \frac{T_s(N)}{T_b} &= \left( \frac{T_0}{T_b} - 1 \right) e^{-\frac{N}{k}} + 1 \\ &\approx \frac{T_0}{T_b} e^{-\frac{N}{k}} + 1 \end{aligned}$$

Assuming an ablation loading process in which  $T_0 = 1 \times 10^4$  K, we find that it still only takes  $\approx 12$  collisions to thermalize the target species within a factor of 2 of the buffer gas temperature. In general  $\approx 100$  collisions are needed to relax rotational states to the same range. Vibrational degrees of freedom may take upwards of  $10^4$  collisions to fully thermalize [cite if the elastic collision energy is much lower than the internal vibrational level].

By finding the mean free path, we can consider the characteristic length the particles travel to be thermalized with the buffer gas, this is then compared to the characteristic length of the cell to determine the effectiveness of the cooling.

$$\lambda = \frac{A_{\text{aperture}} \bar{v}}{4f\sigma \sqrt{m_s/m_b}}$$

If a species is introduced into the buffer gas cell that has a lower vapor pressure than that is allowed at the current temperature, it will be lost when it comes in contact with the cell walls. The rate of this loss can be described as the characteristic time of diffusion of a particle in the buffer gas to the physical dimensions of the cell set the diffusion time constant:

$$\tau_{\text{diff}} = \frac{16}{9\pi} \frac{A_{\text{cell}} n_{0,b} \sigma}{\bar{v}} \quad (3.12)$$

where  $\sigma$  represents the collisional cross section for the buffer gas with the target species. On the other hand, we have the characteristic pump out time given by the conductance of a cell aperture:

$$\tau_{\text{pump}} = \frac{4V_{\text{cell}}}{\bar{v} A_{\text{aperture}}} \quad (3.13)$$

By combining equations eqs. (3.12) and (3.13), we can get a dimensionless ratio,  $\gamma$  that characterizes the extraction fraction out of the cell.

$$\gamma = \frac{\tau_{\text{diff}}}{\tau_{\text{pump}}} = \frac{\sigma f}{L_{\text{cell}} \bar{v}} \quad (3.14)$$

Notice that the  $\gamma$  factor does not depend on aperture size, this is generally true, but increasing the aperture size will lower your number density within the cell, which then influences the characteristic length scale of thermalization. Larger apertures thus run the risk of not allowing your particles to fully thermalize in rotational/vibrational states. But decreasing the aperture size can make alignment as well as controlling the number density more difficult, as finer control over the flow rate is necessary for equivalent flow regimes.

Using equations eqs. (3.14) and (3.10), knowing the physical dimensions of the experimental cell, we find that we may derive theoretical characteristics of the buffer gas beam. During normal operation, our main control over the buffer gas beam is the manipulation of the Ne flow rate, so as a function of buffer gas flow rate ( $f$ ), we may see how key properties are affected.

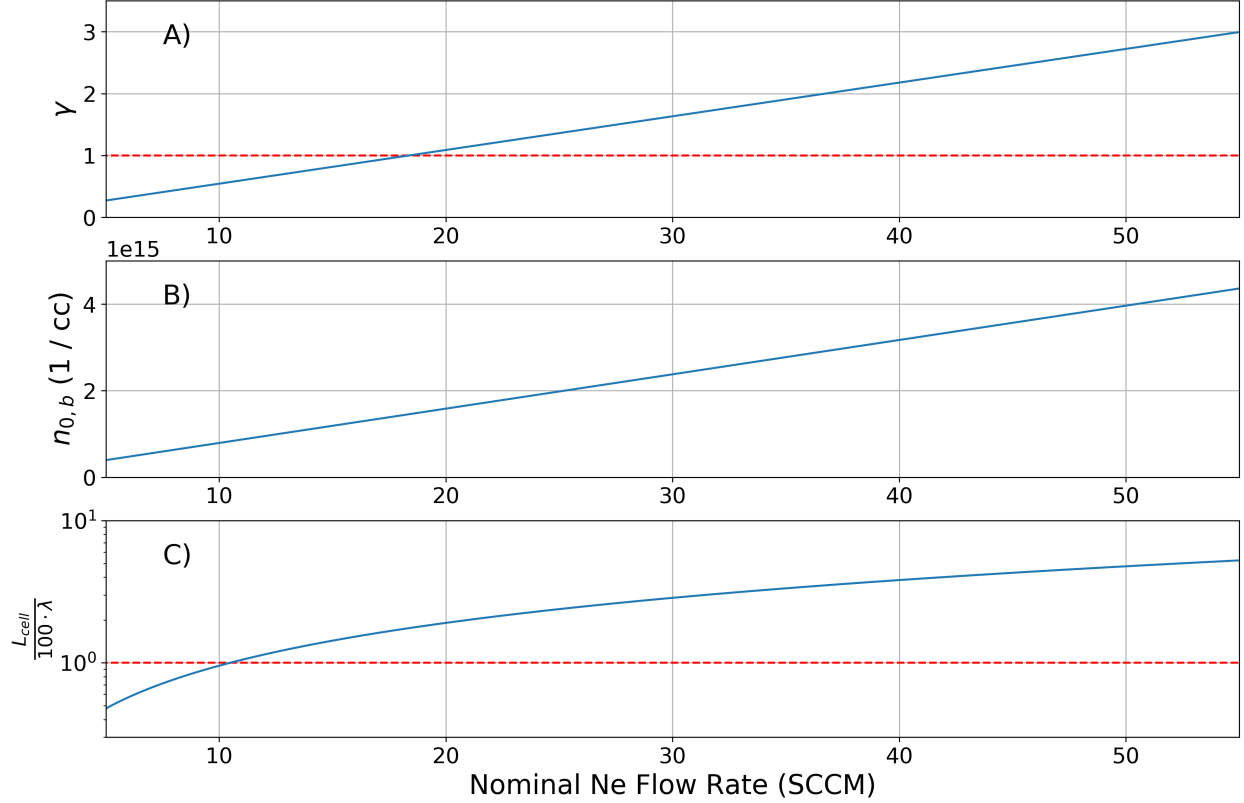


Figure 3.6: Theoretically derived buffer gas beam properties of interest given the physical dimensions of our cell in particular:  $d_{aperture} = 9$  mm. A)  $\gamma$  extraction ratio, dotted red line indicates  $\gamma = 1$  where hydrodynamic entrainment begins. B) Number density of buffer gas species within the experimental cell, given an enclosed back wall. The density of target species introduced should stay under 1% of the buffer gas density for other properties to hold. C) Number of collisions a target species particle would expect before extraction out of the cell, the dotted red line indicates 100 collisions before extraction, when rotational degrees of freedom are characteristically thermalized.

### 3.2.1 Direct density measurements

Although we can make statements about the properties of the buffer gas itself in the beam, we are most interested in the properties of the target species introduced into the cell. In

particular, understanding the extraction ratio  $\gamma$ , as well as the velocity, gives us a good handle on the target species characteristics.

To observe the extraction of the target species from the cell, a residual gas analyzer (RGA) is used to determine the density of the beam in the ballistic regime upstream from the ion trap. To ensure the highest possible signal, the Swagelok vernier flow valve used to regulate water vapor flow into the cell is fully opened. During normal operation of the beam in conjunction with the ion trap, the valve is set to a much smaller opening to ensure the properties of the beam are dominated by the buffer gas species, as well as to control the reaction rates.

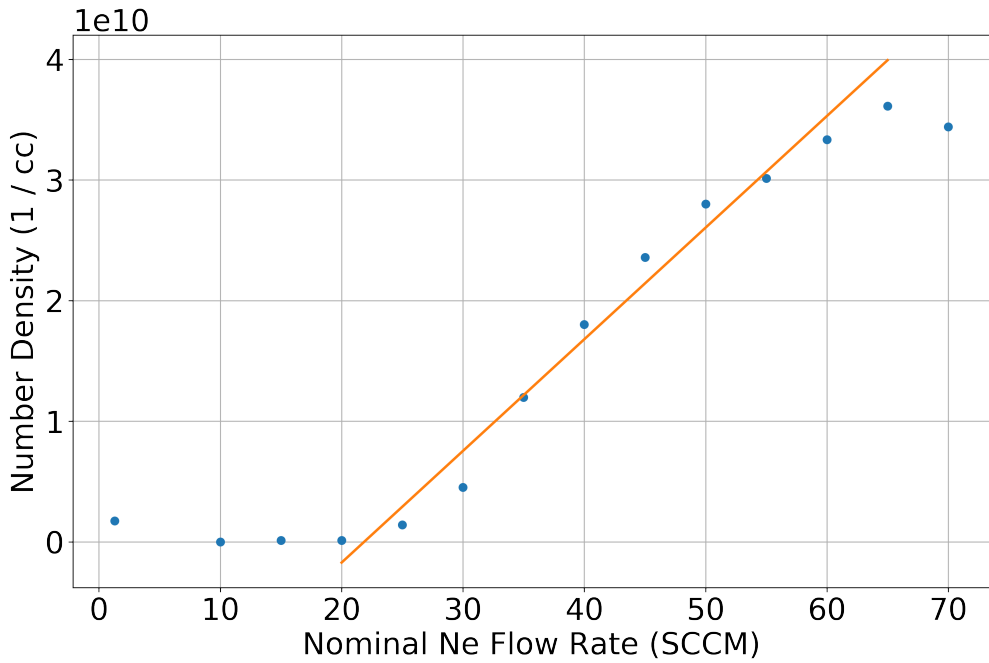


Figure 3.7: Fitted linear behavior of  $\text{H}_2\text{O}$  entrained in a Ne buffer gas beam 30 cm from cell aperture. The onset of hydrodynamic entrainment seems to occur around 20 SCCM up through 60/65 SCCM where the  $\text{H}_2\text{O}$  extracted into the beam has a clear linear form of  $(9.2 \times 10^8 \text{ cm}^{-3}/\text{SCCM})f - 2 \times 10^{10} \text{ cm}^{-3}$ .

We find that theoretical calculations and experimental results agree that the onset of hydrodynamic entrainment occurs at a buffer gas flow rate of  $\approx 20$  SCCM. We can combine

the results here with equations eqs. (3.3), (3.10) and (3.11) to map out beam densities subject to all other possible parameters we may want to adjust, over our entire experimental apparatus. We start by scaling a combination of equations eqs. (3.10) and (3.11) by  $\alpha$ , a buffer gas to target species density scaling factor.

$$n(z) = \alpha \frac{f}{A_{\text{aperture}} \bar{v}} \left( 1 - \frac{z}{\sqrt{z^2 + a^2}} \right)$$

But this only holds true for the region in which the number density is linearly dependent to the buffer gas flow rate, not over all possible ranges; we've seen that the target species only behaves linearly in the hydrodynamic regime. This means that we should be equating the function of  $n(z)$  with the linear fit performed on the data for the parameters the data was taken at.

$$mf + b = \alpha \frac{f}{A_{\text{aperture},0} \bar{v}_0} \left( 1 - \frac{z_0}{\sqrt{z_0^2 + a_0^2}} \right)$$

Where  $z_0 = 30$  cm, being the distance of the RGA from the cell aperture, and  $z = 0 = 2$  mm, for the smallest aperture seen during the experimental run. We also define the experimental scaling factors:

$$\begin{aligned} \alpha &= \frac{m}{\beta} + \frac{b}{\beta f} \\ \beta &= \frac{1}{A_{\text{aperture},0} \bar{v}_0} \left( 1 - \frac{z_0}{\sqrt{z_0^2 + a_0^2}} \right) \end{aligned}$$

Thus, we obtain a form that includes experimentally derived scaling factors that allows us to project the target species density over the length of the system.

$$n(z) = \frac{mf + b}{A_{\text{aperture}} \bar{v} \beta} \left( 1 - \frac{z}{\sqrt{z^2 + a^2}} \right) \quad (3.15)$$

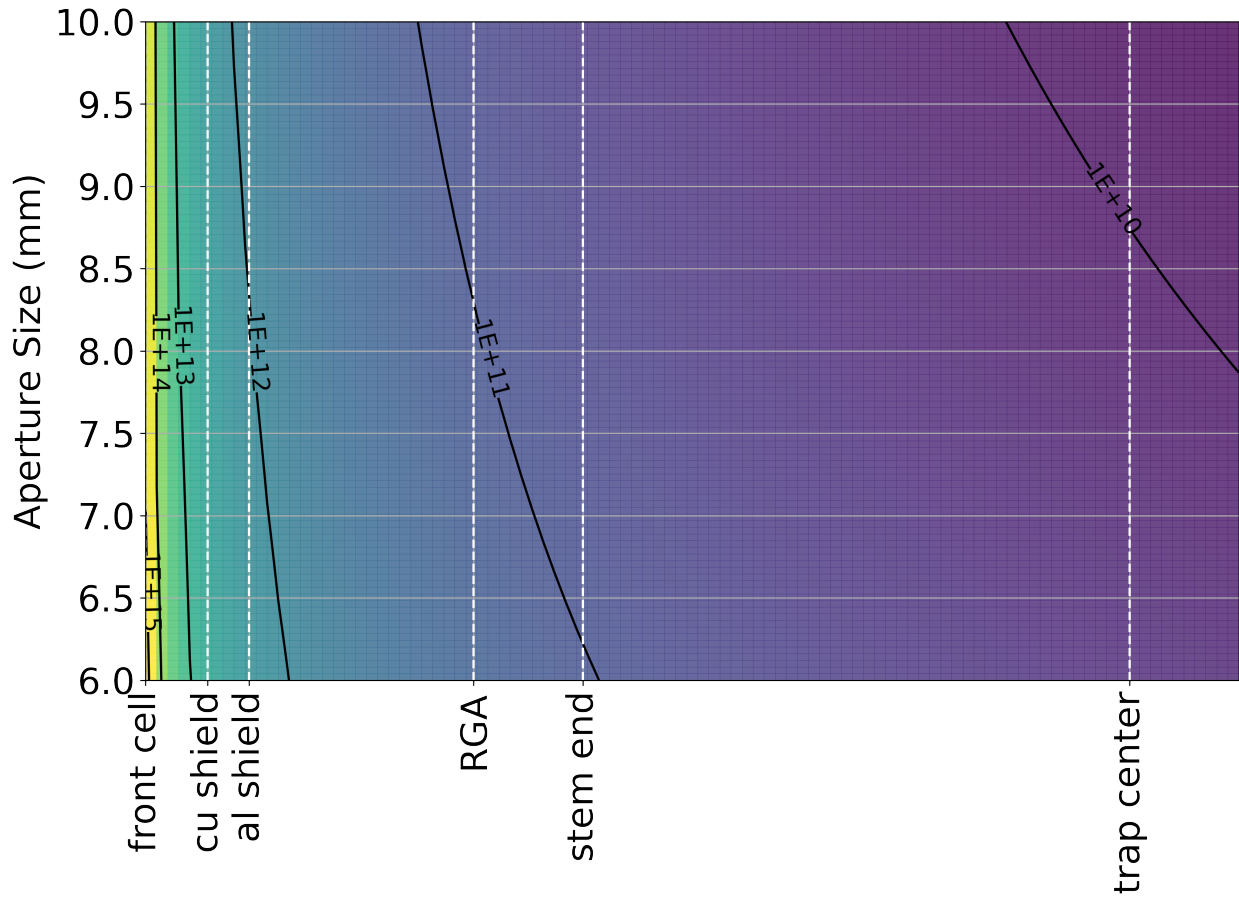


Figure 3.8: Projected beam densities with a Ne flow rate of 30 SCCM with various distances of interest within the chamber. Beam densities shown are without throttling of the H<sub>2</sub>O flow valve.

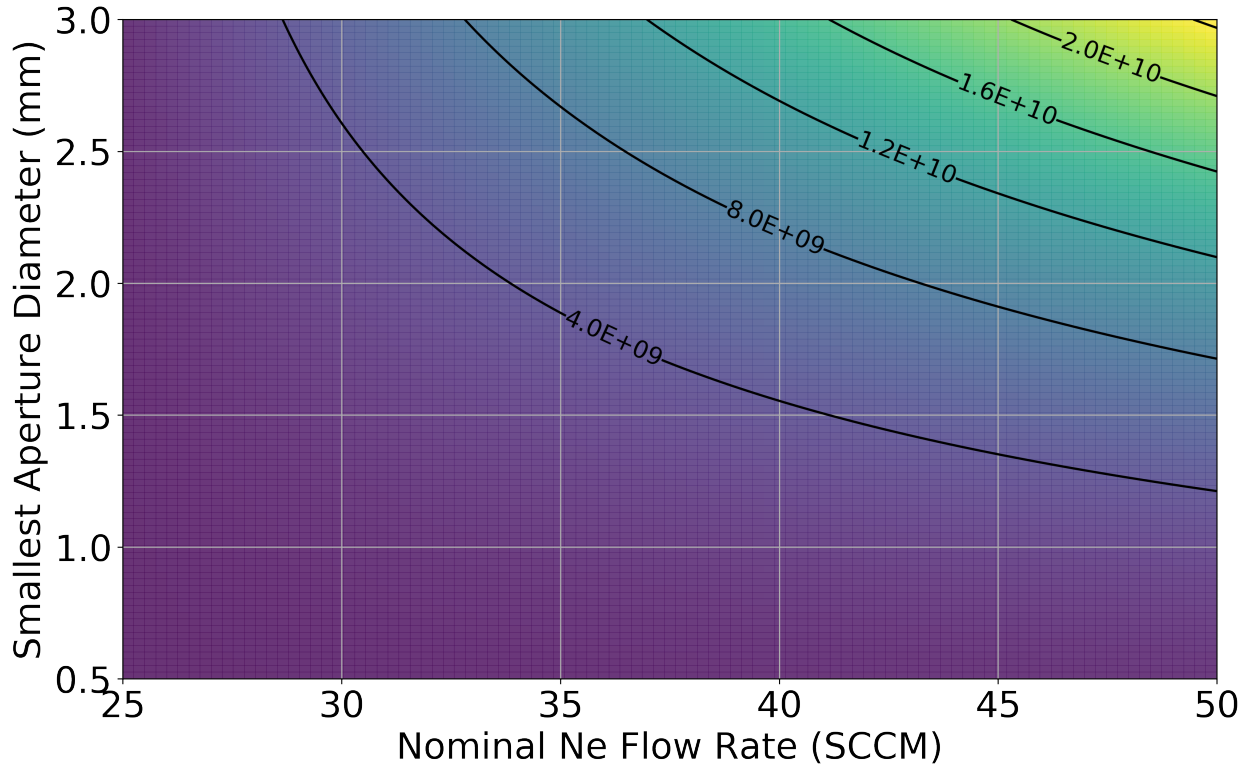


Figure 3.9: Projected beam densities at the trap center over various nominal Ne flow rates and smallest skimmer aperture size. Beam densities shown are without throttling of the H<sub>2</sub>O flow valve.

One should not forget the mass dependence in the thermal velocity equation, which leads us to conclude that the choice of the species is a statement of the dominant species in the beam. If we choose to calculate the thermal velocity of the target species found in the beam due to the theoretical thermal velocity of the buffer gas species, that indicates that the beam properties are still dominated by the buffer gas species. At target species/buffer gas ratios greater than 1/100, we may start to see the effects of the target species on not only the beam density, but also forward velocity.

### 3.3 Beam Velocity

Over the various flow regimes; effusive, intermediate, and supersonic, the forward velocity and distributions change drastically from 150 m/s up to 800 m/s. We first consider the edge cases of the effusive and supersonic regimes. In the effusive regime, we make the assumption that the particles in the cell are non-interacting. We may rewrite the equation 3.2 as a function of the mean velocity  $\bar{v}$  into a simpler form .

$$f(v) = \frac{32}{\pi^2} \frac{v^2}{\bar{v}^3} e^{-4v^2/\pi\bar{v}^2} \quad (3.16)$$

To get the velocity distribution in the beam, we can calculate the distribution of particles incident on an aperture in the cell.

$$\begin{aligned} f_{beam}(v) &= \frac{v}{\bar{v}} f(v) \\ &= \frac{32}{\pi^2} \frac{v^3}{\bar{v}^4} e^{-4v^2/\pi\bar{v}^2} \end{aligned}$$

For low Reynold's numbers ( $Re < 1$ ) the flow at the aperture is purely molecular, which means that there are few to no collisions. This allows us to continue to use the Maxwell-Boltzmann distribution to describe the forward velocity [23].

$$\bar{v}_{\parallel} = \int_0^{\infty} v f(v) dv \approx 1.2\bar{v} \quad (3.17)$$

The spread of the forward velocity of an effusive beam is the full width half max (FWHM) of the Maxwell-Boltzmann distribution:  $\Delta\bar{v} \approx 1.5\bar{v}$ . As the Reynolds number increases, one can reach the supersonic regime ( $Re > 100$ ) where the forward velocity reaches  $1.4\bar{v}$  and the distribution drastically narrows.[23, 33]

But as the flow regime nears the supersonic regime, forward collisions around the aperture cause boosting of the average velocity as well as a decrease in the velocity spread.

Supersonic beam velocities can be shown to be:[33]

Supersonic  
regime  
for-  
ward  
ve-  
loc-

$$v_\infty = \sqrt{\frac{2k_b T_0}{m} \frac{\gamma}{\gamma - 1}}$$

Where  $\gamma$  is the heat capacity ratio  $C_p/C_v$ , and  $T_0$  is the original temperature of the source.

The intermediate regime in between the effusive and supersonic regimes is particularly difficult to model, for there are some collisions at the aperture, causing some boosting and narrowing, but not enough to treat the behavior as fully fluid-like. The section 3.2 results show that we can produce a beam in this intermediate regime by demonstrating clear hydrodynamic entrainment.

To better understand the reaction temperatures we will be able to reach, we need a characterization of the beam's velocity, more specifically, the velocity of the target species entrained within the buffer gas. The ideal target species is one with a reliable loading method and can be directly detected in small amounts. Ytterbium metal is known to have good ablation properties and the produced neutrals have well known spectra. By ablating ytterbium foil inside of the experimental cell while the neon gas is being introduced, the ytterbium is cooled by the buffer gas and carried out of the cell. As long as the target species number density is a trace amount in comparison to the bulk buffer gas number density (0.1%), the flow characteristics are dominated by the buffer gas species [22]. Based upon the results of our direct RGA measurements of the beam density, we know that the cell parameters used in the previous measurement land us in the intermediate flow regime due to the clear evidence of hydrodynamic entrainment.

To determine the velocity of the beam, we ablate an ytterbium target mounted inside the experimental cell where both neon and water are being introduced. The resulting beam is then hit with a 399 nm laser to excite the Yb isotope transitions. The laser is scanned over 3.5 GHz, encompassing all possible Yb isotope peaks. Two scans were taken, one with the 399 nm light perpendicular to the beam path, and the other where the laser is coming in with an angle of 57.3°. The resulting spectra are then fitted with summed Gaussian functions with predetermined isotopic shifts, giving us the center ( $^{174}\text{Yb}$ ) frequency, as well as the widths

of the lines. The fitted shared widths give us a beam temperature of 20 K, which is exactly what the experimental cell was held to. Comparing the shift of the  $^{174}\text{Yb}$  frequency between the transverse beam scan and the angled one, we can determine the forward velocity.

$$\Delta f = \frac{\Delta v}{v} f \cos(\theta) \quad (3.18)$$

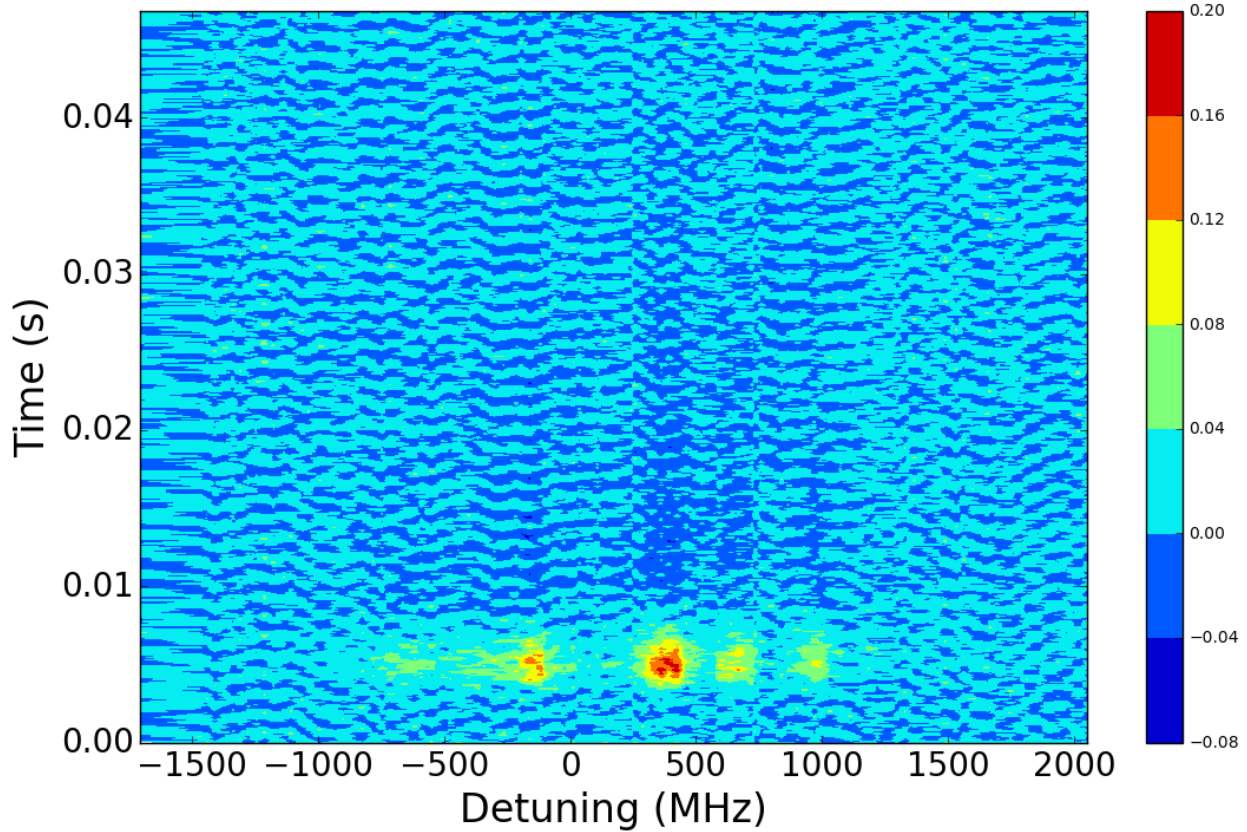
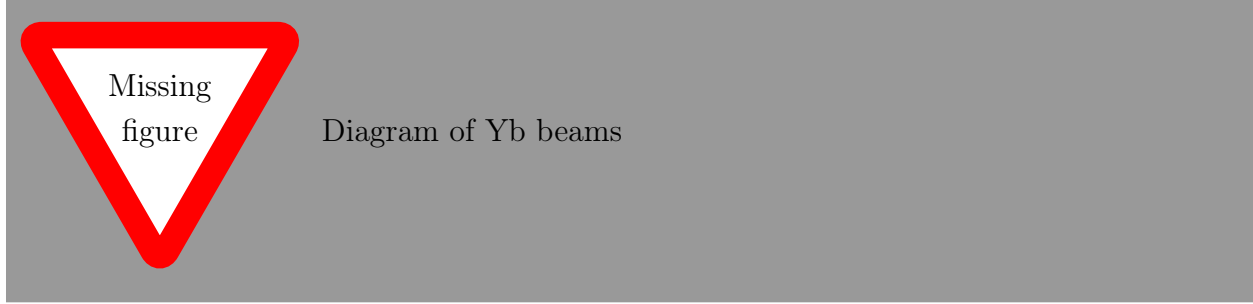


Figure 3.10:

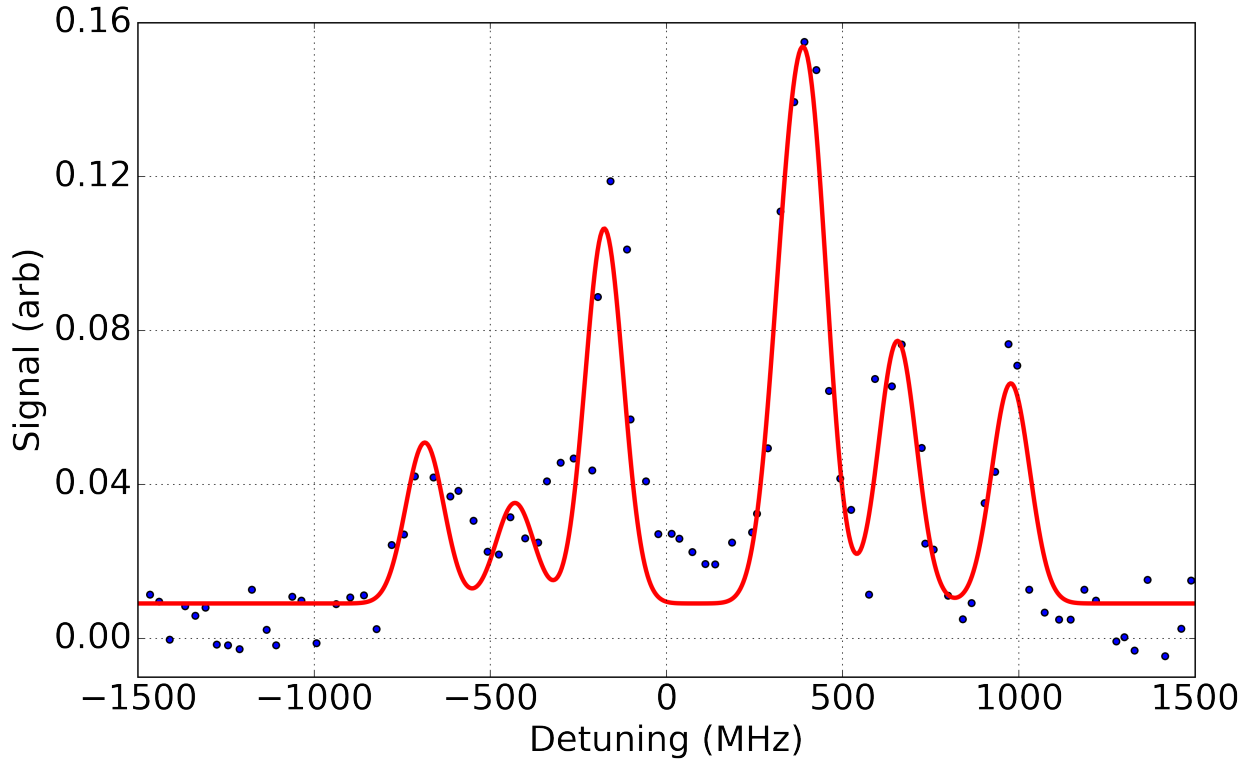


Figure 3.11:

We find that the Yb is entrained within the neon and sympathetically cooled to the cell's temperature. The water that is also introduced in the beam will also be at a similar temperature and forward velocity as long as the neon density is much larger than that of the water when the beam dynamics is dominated by the properties of the buffer gas species.

### 3.4 Beam Shuttering

With the RGA in the beam path, we were able to open and close a shutter in the beam path and see an extinction of the water signal, but a more accurate representation would be from the ions in the trap themselves. We know that the trapped  $\text{Be}^+$  ions will react with  $\text{H}_2\text{O}$  to predominately produce  $\text{BeOH}^+$ , which we see as a drop in the fluorescence. Figure 3.14 shows fits of the fluorescence decay as a beam from the CBGB is suddenly blocked by our

shutter in the beam line. Comparing the fitted reaction rates, we find that they agree with the background rates found as shown in figure 3.13. This indicates to us that we indeed have a beam of cryogenic water coming from the CBGB, as seen by the sudden extinction of the  $\text{Be}^+ + \text{H}_2\text{O}$  reaction.

To accurately control the reactions occurring in the ion trap, it is ideal to be able to quickly turn the beam on and off. Controlling the fill lines outside of the chamber is not ideal, as thin tubing was used, yielding very low conductances. The characteristic time of flow through a tube can be shown to be  $\tau_{tube} = CV$ , where  $C$  is the conductance and  $V$  is the volume of the tube in question. Turning on and off the flow outside of the chamber would give time constants in the range of seconds. To more deterministically control the beam flux, we insert a vacuum compatible Uniblitz VS35 35mm Optical Shutter in the beam line. The shutter does not create a seal within the chamber, background gasses may flow around and influence the beam.

Running the beam with the shutter in between the RGA and experimental cell, we find that there is a distinct difference in the  $\text{H}_2\text{O}$  signal when the shutter is open and closed. Using laser cooled  $\text{Be}^+$ , we find the difference in the reaction rate both independently, as well as in situ, figs. 3.13 and 3.14.

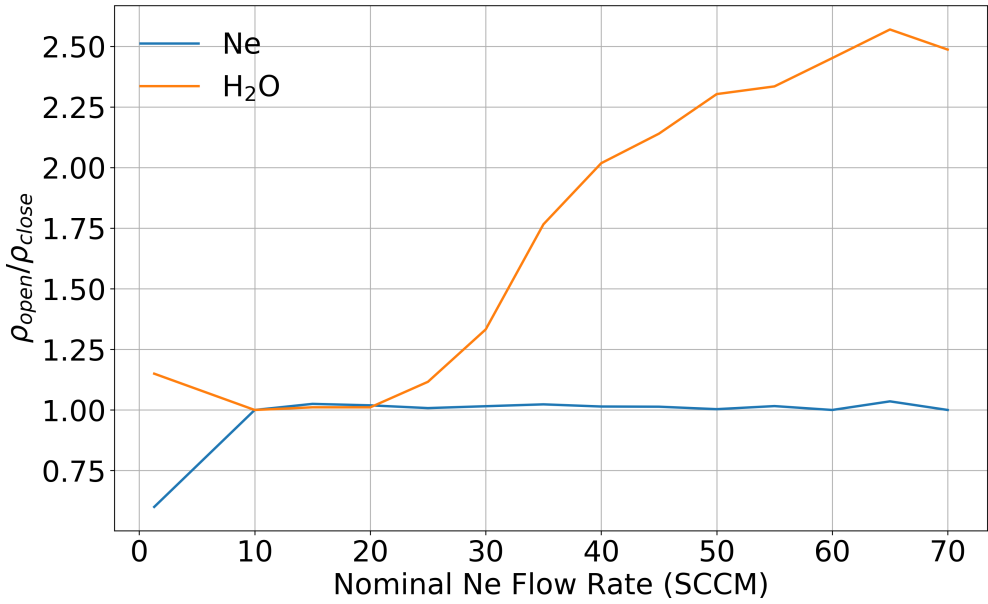


Figure 3.12: RGA contrast

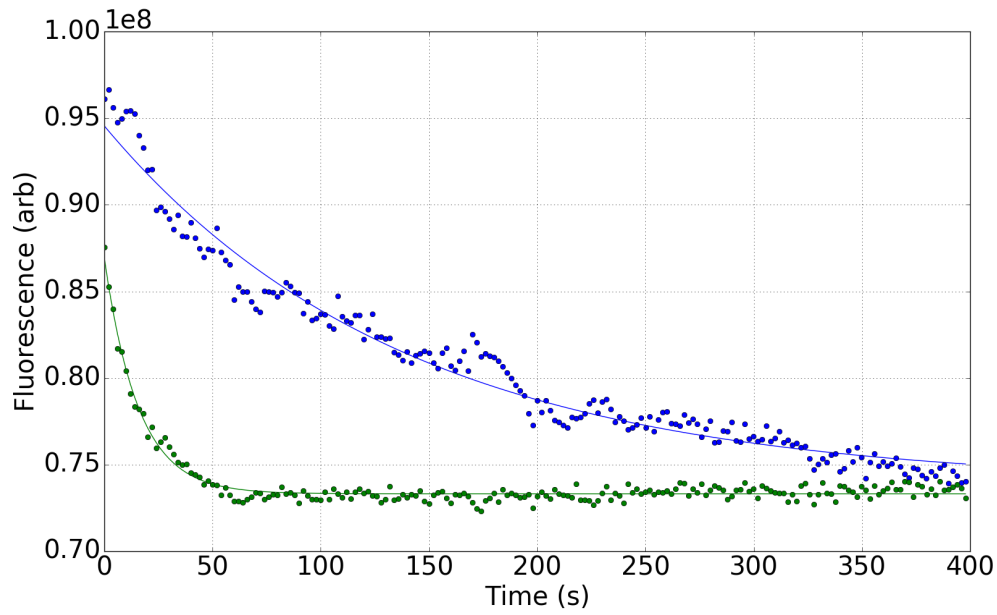


Figure 3.13: Fluorescence decays of loaded  $\text{Be}^+$  ions exposed to a cold water beam with an inline shutter either opened, in green ( $\tau = 7.23 \times 10^{-3} \text{ s}$ ) or closed, in blue ( $\tau = 6.37 \times 10^{-2} \text{ s}$ )

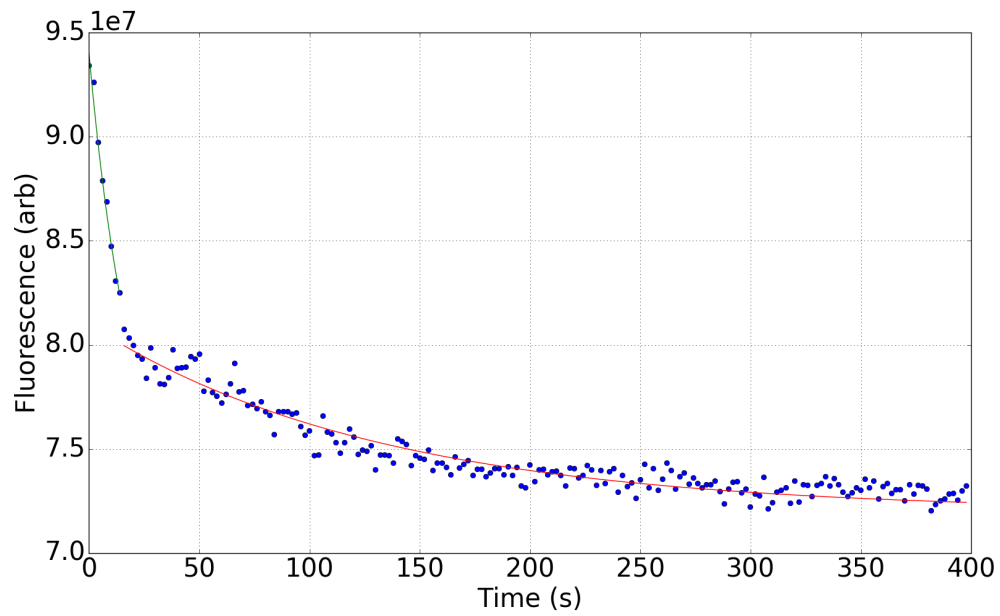


Figure 3.14: Fluorescence decays of loaded  $\text{Be}^+$  ions exposed to a cold water beam with an inline shutter opened, in green ( $\tau = 5.37 \times 10^{-2}\text{s}$ ) or closed, in red ( $\tau = 7.59 \times 10^{-3}\text{s}$ )

# CHAPTER 4

## Trapping and Cooling Ions

### 4.1 Ion Trapping

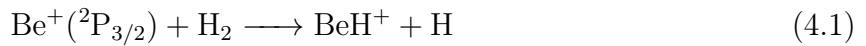
Use RF fields at 1MHz in a linear quadrupole ion trap (LQT) to trap charged particles spatially .

cite  
the  
OG  
Paul

### 4.2 Vacuum Requirements

To reliably laser cool and trap ions into crystals, it is ideal to have ultra-high vacuum (UHV) which is generally defined as having a pressure  $< 10^{-9}$  Torr. The characteristic collision rate between a monopole and polarizable neutral is defined by the  $C_4/r^4$  attractive term and is called the Langevin collision rate. In a vacuum chamber, we tend to find the predominant gas left after baking is H<sub>2</sub>, which will have collisions with the trapped ions at the Langevin rate.

By knowing the rate of



to be [36]. With an ion gauge, we find our vacuum to be 1e-10 Torr, and verified via rate Be<sup>+</sup> fluorescence decay due to reactions with background H<sub>2</sub>.

We want to make sure that there is as little H<sub>2</sub>O in the chamber as possible to ensure that the data we take with the water from the CBGB is exclusively from the CBGB and not due to background water collisions.

### 4.3 ${}^9\text{Be}^+$ Laser Cooling

Laser cooling for the  ${}^9\text{Be}^+$  ion is done with a Toptica TA-FHG Pro tuned to 313 nm with a peak power of 400 mW. The laser is detuned by 400 MHz from the  ${}^2\text{S}_{1/2}$  to  ${}^2\text{P}_{3/2}$  transition. We let the light

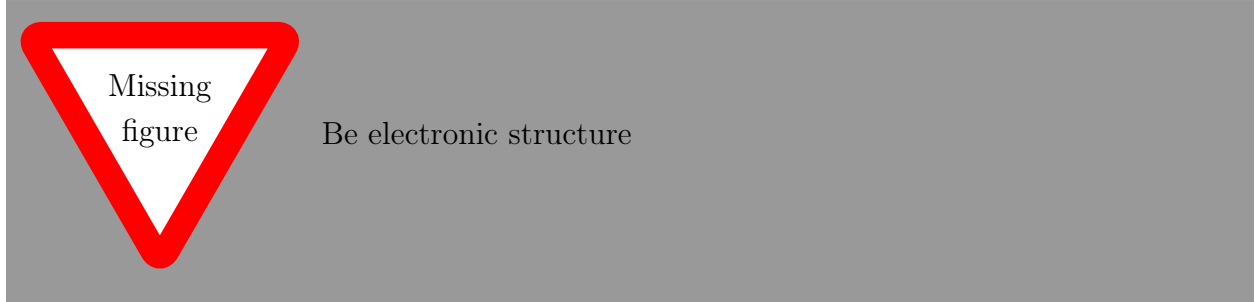


Figure 4.1: Electronic structure of  ${}^9\text{Be}^+$ . Laser cooling is done with 313 nm light tuned from the  ${}^2\text{S}_{1/2}$  to  ${}^2\text{P}_{3/2}$  state.

The scatter rate of two level system is defined as:

$$\rho_{pp} = \frac{a}{2} \frac{s}{a + s + 4(\delta/\Gamma)^2} \quad (4.2)$$

$$f_L = \frac{a\Gamma}{\Delta^2 + \Gamma^2/4} \quad (4.3)$$

$$I_s = \frac{\pi hc}{3\lambda^3\tau} \quad (4.4)$$

$$s_0 = \frac{I}{I_s} \quad (4.5)$$

Where  $\rho_{pp}$  is the fraction of the population in the excited P-state,  $s$  is the saturation parameter,  $\Gamma$  is the transition linewidth,  $\delta$  is the detuning from resonance, and  $a$  is an overall

scaling parameter encompassing all of the efficiencies associated with the optical collection and detection.

Ideally, having a single ion in the trap while sweeping the frequency or power would allow us to determine the saturation parameter, and thus the fraction of  $\text{Be}^+$  in the excited  ${}^2\text{P}_{3/2}$  state. Due to the size and depth of our ion trap, we cannot reliably load only one ion. On top of that, the most common residual gasses in a vacuum chamber,  $\text{H}_2\text{O}$  and  $\text{H}_2$  both readily react with  $\text{Be}^+$  in the excited state. The pressures we reach, indicate that we may expect reaction rates of order once per 10 seconds.

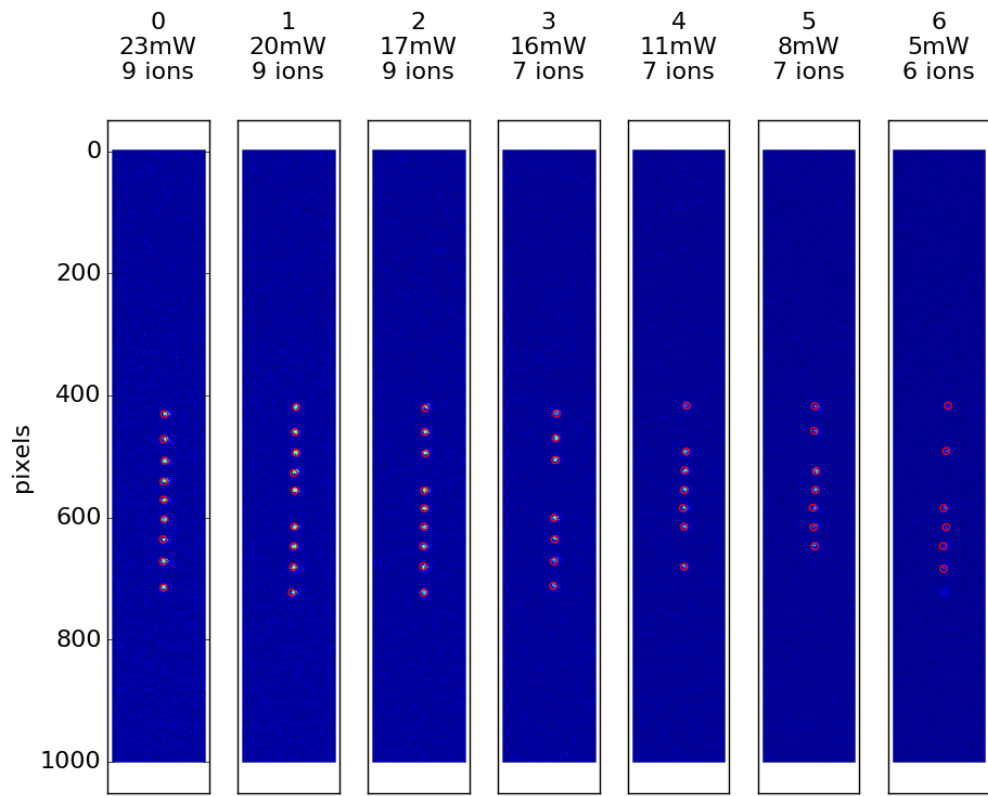


Figure 4.2: Set of ion images taken at various 313 nm powers with an algorithm that identifies individual ions

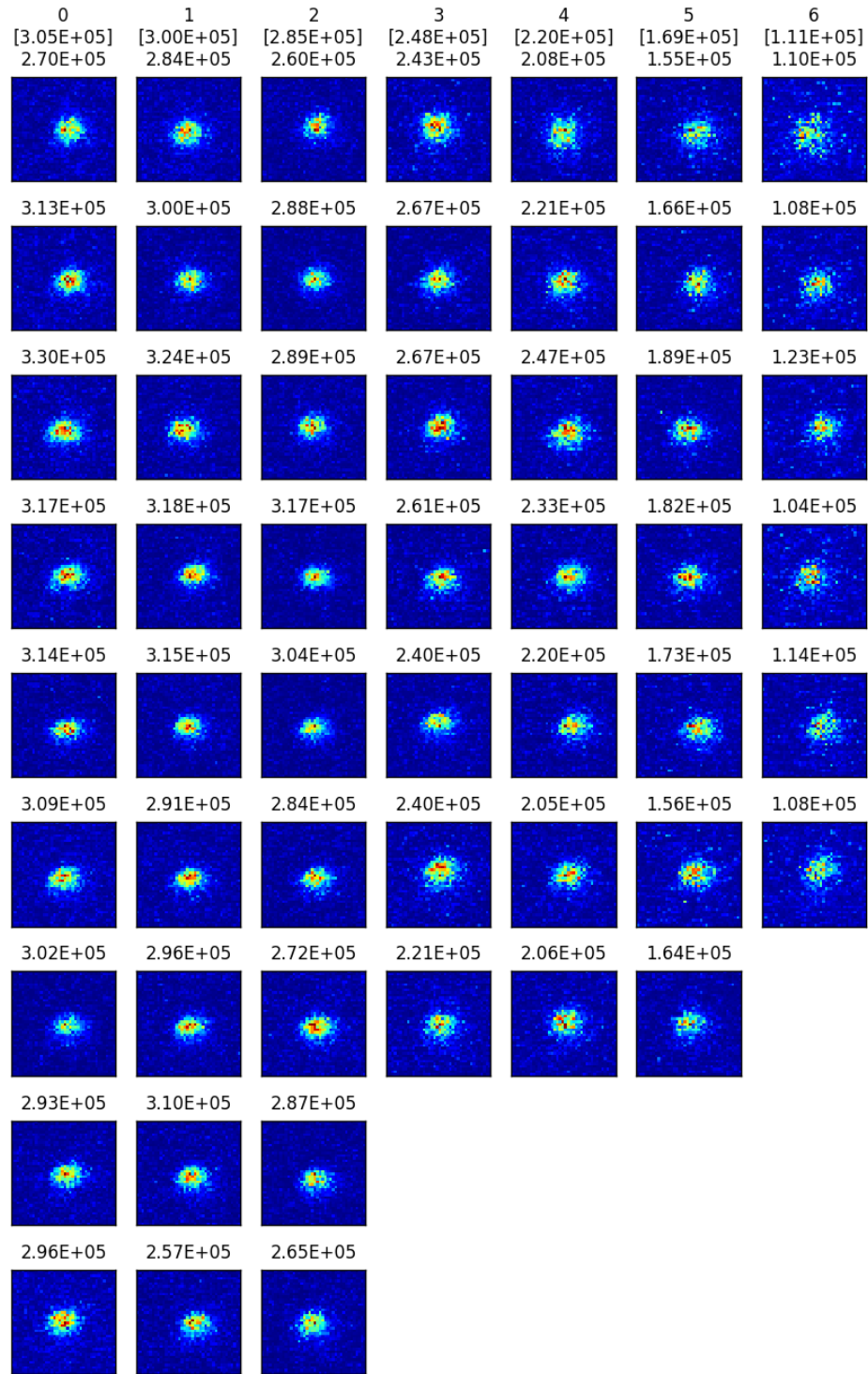


Figure 4.3: Individual ions identified from images in figure 4.2. Integrated fluorescence counts shown for each image as well as averaged value in brackets.

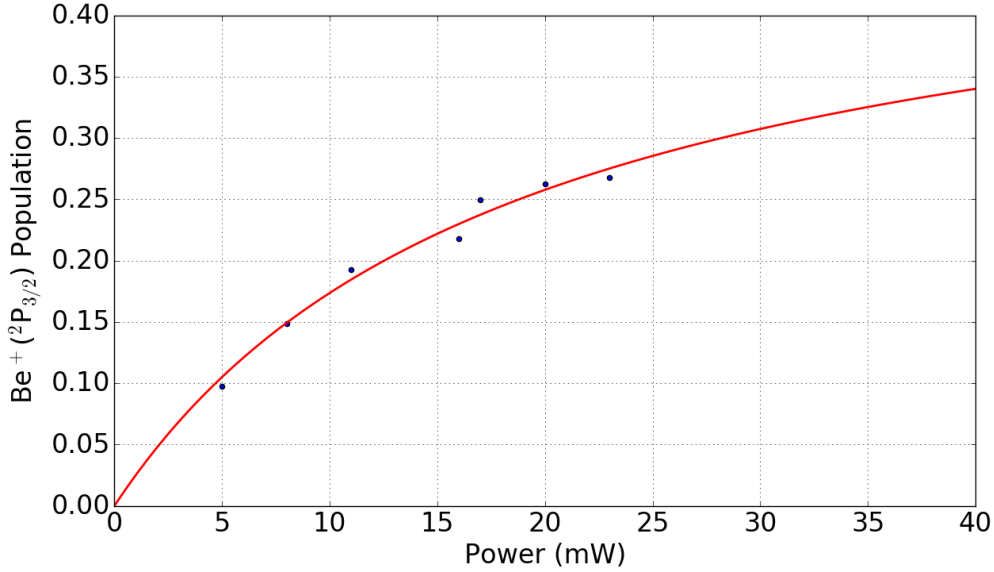


Figure 4.4: P-state fraction curve fitted to incident laser power at a fixed detuning of  $\omega_l = \omega_0 - \Gamma/2$ .

#### 4.4 Time of Flight Mass Spectrometer (TOF-MS)

pew pew shoot the ions into a tube and measure their mass

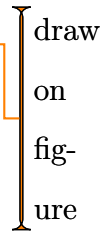
#### 4.5 Dual Species Loading

Although loading and cooling Be<sup>+</sup> ions is fairly straight forward, it is not as clear as how to load C<sup>+</sup> ions into the trap with Be<sup>+</sup> reliably. Early attempts involved using the home-made electron gun to electron dissociate and CO gas introduced via leak valve, all possible ionized products of CO were detected (C<sup>+</sup>, O<sup>+</sup>, and CO<sup>+</sup>). Even when loading into an empty trap, it was not possible to reliably isolate the C<sup>+</sup> via A-ramping of the trap RF voltage. Prolonged use of the electron gun directly towards the ion trap also caused charging that would slowly dissipate and change the trap parameters. On top of these complications, it would have to work in conjunction with ablation loading Be<sup>+</sup>.

Instead of using two different methods to load the different ion species, ablating both

simultaneously was found to be the best method. A sample of Be metal was placed on top of a piece of graphite on the target holder so that both samples were in view of the ablation laser. The set up shown in figure 4.5 allowed us to separate the ablation laser into two beam with independent alignment and focal planes. The polarization of the laser light is rotated with a half-waveplate, which then enters a polarizing beam splitter (PBS), allowing for tuning of power into either path. The vertically polarized reflected light is reflected again with another PBS and is steered up to the objective lens and then focused into the chamber. The horizontally polarized light transmitted through the first PBS is aligned through an adjustable telescope system. This light is then realigned with the vertically polarized light on the second PBS, co-propagating into the chamber. The "delay stage" for the horizontal light allows for independent focusing and alignment onto the sample.

---



draw  
on  
fig-  
ure

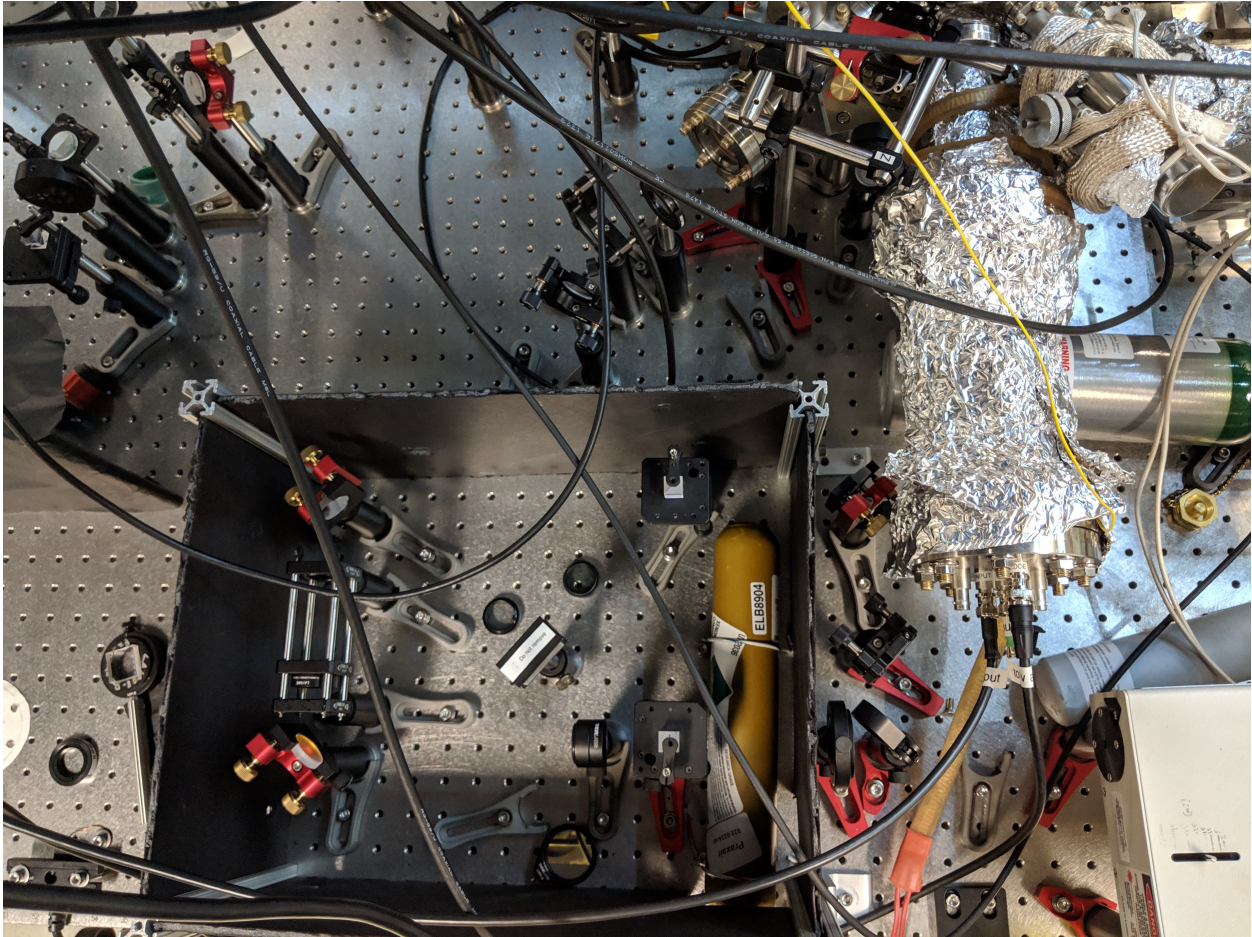


Figure 4.5: Image of the single laser, dual ablation set up. The 1064 nm YAG pulse is split into two paths, and recombined such that they proceed through the same focusing element into the chamber to hit two different targets.

Blocking one beam allowed for adjustments for the ablation of each species independently. When loading  $\text{C}^+$ , we found a strong dependence of the trapped species and the fluence. Lower fluence created not only  $\text{C}^+$ , but clusters of,  $\text{C}_2^+$ , and  $\text{C}_3^+$  as well. Tight focusing of the beam improves the efficiency of creating only  $\text{C}^+$ , but some  $\text{Cn}^+$  is still usually produced, which can then be ejected out of the trap with a soft A-ramp.

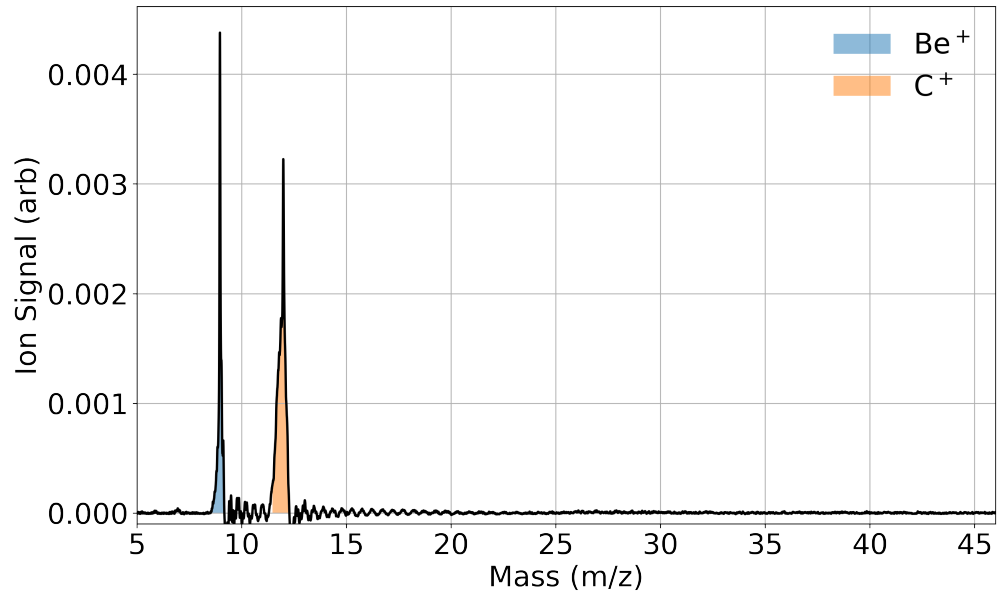


Figure 4.6: TOF trace of simultaneous  $\text{Be}^+$  and  $\text{C}^+$  ablation loading averaged over 10 shots.  
A soft A-ramp is applied after loading, ejecting any unintentionally loaded  $\text{C}_n^+$  clusters.

# CHAPTER 5



## 5.1 Optical Control of Reactions between Water and Laser-Cooled $\text{Be}^+$ Ions

### 5.1.1 Abstract

We investigate reactions between laser-cooled  $\text{Be}^+$  ions and room-temperature water molecules using an integrated ion trap and high-resolution time-of-flight mass spectrometer. This system allows simultaneous measurement of individual reaction rates that are resolved by reaction product. The rate coefficient of the  $\text{Be}^+(\text{^2S}_{1/2}) + \text{H}_2\text{O} \longrightarrow \text{BeOH}^+ + \text{H}$  reaction is measured for the first time and is found to be approximately two times smaller than predicted by an ion-dipole capture model. Zero-point-corrected quasi-classical trajectory calculations on a highly accurate potential energy surface for the ground electronic state reveal that the reaction is capture-dominated, but a submerged barrier in the product channel lowers the reactivity. Furthermore, laser excitation of the ions from the  $\text{^2S}_{1/2}$  ground state to the  $\text{^2P}_{3/2}$  state opens new reaction channels, and we report the rate and branching ratio of the  $\text{Be}^+(\text{^2P}_{3/2}) + \text{H}_2\text{O} \longrightarrow \text{BeOH} + \text{H}$  and  $\text{H}_2\text{O} + \text{Be}$  reactions. The excited-state reactions are nonadiabatic in nature.

#### 5.1.1.1 Introduction

Low-temperature reactions of simple ions with small molecules play a central role in astrochemical environments from interstellar clouds to cometary comae to planetary atmospheres, including that of Earth[2, 24]. The chemical evolution of interstellar molecular

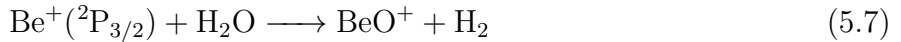
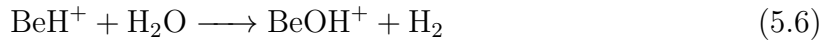
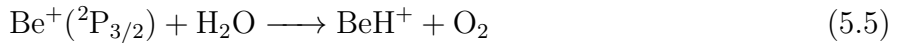
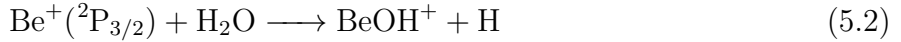
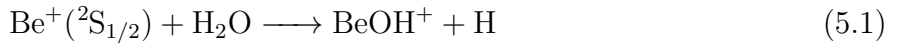
clouds ultimately yields the seedbed from which new stars and planets are born and the raw materials from which life likely developed. A firm understanding of the reaction rates for a host of elementary ion-molecule reactions is essential to accurately model these environments these environments. Techniques such as selected ion flow tubes (SIFTs)[1], guided ion beams[3], and supersonic flows (CRESU)[40] have improved our empirical understanding of these processes; however, each has its own limitations.[43, 44] Theoretically, it has long been recognized that these ion-molecule reactions are often barrierless, and their rates are frequently described by capture models.[16] However, recent studies have revealed that dynamical features can sometimes prevail,[29, 26, 6] in which case statistical treatments may not be accurate.[18, 9] Therefore, new experimental and theoretical efforts are needed to accurately address ion-molecule chemistry.

We have developed an approach, adapted from the ultracold ion community,[20, 50, 53] to study reactions of atomic ions with small molecules. Here we report the use of this approach to study the reaction of  $\text{Be}^+$  with gas-phase water for the first time. There have been very few experimental studies of gas-phase reactions between metal ions and water, especially at low temperature, despite their importance for metal ion chemistry in a range of environments.[19, 32, 52]

Singly ionized beryllium is a particularly attractive metallic reactant to use for such studies because it is both theoretically tractable and experimentally highly controllable. The relatively simple electronic structure of this three-electron ion allows both highly accurate characterization of its electronic structure and laser cooling,[4] and the low mass of  $\text{Be}^+$  lends itself to high motional frequencies as well as efficient sympathetic cooling of other chemically interesting atomic ions when employed in ion traps.[7, 36, 25, 39] For the molecular reaction partner,  $\text{H}_2\text{O}$  is arguably the most important molecule in chemistry, and theoretical studies of its reactions with a single atom have been reported on full-dimensional potential energy surfaces (PESs).[27, 45, 35, 28, 56] Thus this system of reagents provides an opportunity to perform a high-resolution comparison between experiments and theory for a molecule-ion system.

The apparatus employed here is shown in the Supporting Information (SI) (Figure S1). Laser ablation of metallic Be is used to produce  $\text{Be}^+$  ions, which are trapped in a linear radio frequency Paul trap.[55] Laser cooling [54] is used to cool the translational motion of the ions, resulting in a Coulomb crystal of  $\text{Be}^+$  ions. Gaseous, room-temperature  $\text{H}_2\text{O}$  molecules are then introduced via a leak valve into the trapping region, where they react with the trapped ions. Charged products of the chemical reaction remain in the trap and are subsequently detected via an integrated time-of-flight mass spectrometer (TOFMS) recently developed by our group[38, 37] and used to discover new species.[34] The total reaction rate is measured by monitoring the decay of  $\text{Be}^+$  ion fluorescence, and the product branching ratios are extracted from the mass spectrum.

A key feature of this experiment is that by varying the detuning of the 313 nm laser used to cool the ions, the population in the excited  $1\text{s}^2 2\text{p}^1 {}^2\text{P}_{3/2}$  and ground  $1\text{s}^2 2\text{s}^1 {}^2\text{S}_{1/2}$  states can be controlled. Because the energy difference between the ground and excited states is 3.96 eV, several more product channels are open for the  $\text{Be}^+({}^2\text{P}_{3/2}) + \text{H}_2\text{O}$  entrance channel. Using this system, we are able to measure the reaction rate and product branching ratio for these two entrance channels. We find that the ground-state channel,  $\text{Be}^+({}^2\text{P}_{3/2}) + \text{H}_2\text{O}$ , exclusively produces  $\text{BeOH}^+ + \text{H}$ , whereas the excited-state channel,  $\text{Be}^+({}^2\text{P}_{3/2}) + \text{H}_2\text{O}$ , also produces  $\text{H}_2\text{O}^+ + \text{Be}$  with a yield of 10%. Specifically, the reactions considered here are



Because the translational energy of the laser-cooled  $\text{Be}^+$  ions is  $< 0.5$  K, the energy of the room-temperature water sets the reaction kinetic energy of  $\text{Be}^+ + \text{H}_2\text{O}$  in the center of mass frame to 100K. The internal state distribution of the  $\text{H}_2\text{O}$  is assumed to be given by the 300 K. Typical TOF traces (10 sample average) at reaction times  $t = 0$  and 70 s with 7 and 26% relative  $\text{Be}^+(\text{P}_{3/2})$  state excitation are shown in Figure 1A,B, respectively. The fluorescence signal, which is used to determine the reaction time zero and normalize the initial ion number for the TOF, is monitored by the camera (ANDOR iXON3 EMCCD) in real time. At  $t = 0$  s, a large peak of  $m/z = 9(\text{Be}^+)$  and a smaller one of  $m/z = 9(\text{BeOH}^+)$  are evidenced in the TOF trace (blue line), which indicates that  $\text{Be}^+$  ions are the main species in the trap at  $t = 0$ . The finite amount of  $\text{BeOH}^+$  at  $t = 0$  reflects the fact that reactions eqs. (5.1) to (5.8) happen even during the loading process and that the mass filtering procedure is imperfect. At  $t = 70$  s, a  $m/z = 19$  peak emerges when more  $\text{Be}^+$  ions are excited to  $\text{P}_{3/2}$  state, which we identify as  $\text{H}_3\text{O}^+$  resulting from reactions eqs. (5.3) and (5.4). The  $\text{BeOH}^+ / \text{H}_3\text{O}^+$  ratio,  $\eta(P_P)$ , is measured by integrating both peaks for the experimentally controlled excited-state population  $P_P$ . The  $\text{BeOH}^+$  signal includes the amount unfiltered during loading, products from both reactions eqs. (5.1) and (5.2), as well as, in principle, the two-step reactions eqs. (5.5) to (5.8). The  $\text{H}_3\text{O}^+$  signal is produced via the two-step reactions eqs. (5.3) and (5.4). Whereas we do not observe products from reactions eqs. (5.5) to (5.8) (see also in SI), they are thermochemically allowed and therefore included in our analysis, which sets upper limits on their reaction rate coefficients.

The total reaction rate is given by  $\Gamma_t = \rho_{\text{H}_2\text{O}} k_t$ , where  $\rho_{\text{H}_2\text{O}}$  is the  $\text{H}_2\text{O}$  density measured from a Stanford Research Systems residual gas analyzer (RGA) calibrated to an ion gauge (see the SI for more information) and  $k_t$  is approximated as  $k_t = P_S k_1 + P_P k_2 + P_P k_3$ , where  $P_S$  and  $P_P$  are the  $\text{Be}^+$  population in the  $\text{S}_{1/2}$  and  $\text{P}_{3/2}$  states, respectively, and  $k_i$  is the reaction rate coefficient of reaction  $i$ . Reaction eq. (5.4) has been studied by other groups, reporting a rate coefficient of  $(2.05 \pm 0.010) \times 10^{-9} \text{ cm}^3/\text{s}$ .<sup>[21]</sup> The measured  $\text{H}_3\text{O}^+ / \text{BeOH}^+$

ratio is given from the reaction rates by

$$\eta(P_{\text{P}}) = \frac{P_{\text{P}}k_3}{P_{\text{S}}k_1 + P_{\text{P}}k_2} \quad (5.9)$$

To use equation 5.9 to extract the individual rate coefficients ( $k_i$ ), the total reaction rate  $\Gamma_t$  is first measured by monitoring the  $\text{Be}^+$  fluorescence decay with a camera, as shown in Figure (see also the SI). Fluorescence decay is monitored directly after a DC voltage applied to trap electrodes is used to filter out the heavier products from the trap to allow better crystallization of the  $\text{Be}^+$  ions by reducing ion-ion heating.[8] The inset of Figure shows typical fluorescence images of the  $\text{Be}^+$  coulomb crystal at various times. Fluorescence is used to measure the total reaction rate because the total measurement time is 30 times shorter than using the TOFMS (Figure ). To determine the separate rate coefficients for the  $\text{Be}^+$  ground and excited states, we measure the total reaction rate coefficients for different excited-state fractions, shown in Figure . A linear fit (blue line) is found using the least-squares method. The vertical intercept of this fit gives the  $\text{Be}^+$  ground-state reaction rate coefficient  $k_1 = (2.2 \pm 0.3_{\text{stat}}) \times 10^{-9} \text{ cm}^3/\text{s}$ , whereas the sum of the slope and intercept gives the total excited-state  $\text{Be}^+$  reaction rate coefficients  $k_2 + k_3 = (4.7 \pm 1.7_{\text{stat}}) \times 10^{-9} \text{ cm}^{-3}/\text{s}$ . Using equation 5.9, the reaction rate coefficients of reactions eqs. (5.2) and (5.3) are then calculated to be  $k_2 = (4.2 \pm 1.6_{\text{stat}}) \times 10^{-9} \text{ cm}^{-3}/\text{s}$  and  $k_3 = (0.47 \pm 0.11_{\text{stat}}) \times 10^{-9} \text{ cm}^{-3}/\text{s}$ , respectively. The ratio of reaction rate coefficients for reactions eq. (5.3) to eq. (5.2) is therefore  $k_3/k_2 = 0.11 \pm 0.03$  independent of systematic errors in the density measurement. Charged products from reactions eqs. (5.5) and (5.7) to be  $< 5 \times 10^{-10} \text{ cm}^3/\text{s}$ . Reactions at these upper bounds for the rate coefficients do not significantly change the analysis above, justifying their exclusion from  $k_i$ .

It is instructive to compare these measured rate coefficients to those predicted by capture theory. For an ion reacting with a polar molecule, the leading order interaction potential as a function of the molecule-ion separation  $r$  is described by monopole-dipole interaction ( $U \propto r^{-2}$ ) and the polarization of the molecule by the ion ( $U \propto r^{-4}$ ). For this case, the rate coefficient is typically found using the average dipole orientation (ADO) collision model,[47]

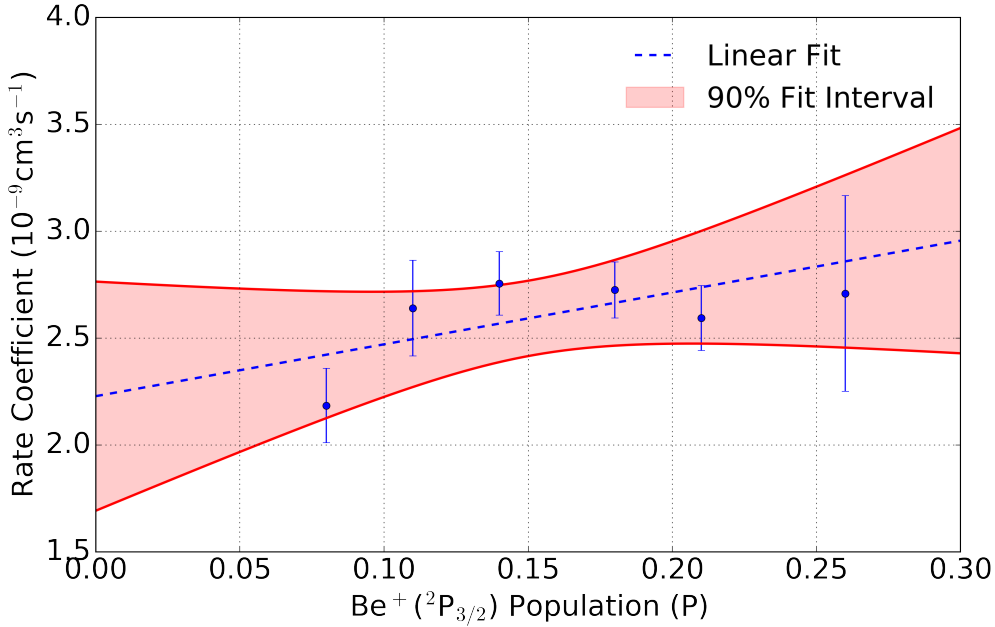


Figure 5.1:

where the ion-dipole interaction is averaged over rotational states. The expression for the rate coefficient from ADO theory is

$$k_{\text{ADO}} = 2\pi e \sqrt{\frac{\alpha}{\mu}} + 2\pi e \mu_D C \sqrt{\frac{2}{\mu \pi k_B T}} \quad (5.10)$$

where  $\alpha$  is the average neutral molecule polarizability,  $\mu$  is the reduced mass,  $\mu_D$  is the molecular dipole moment,  $e$  is the elementary charge, and  $C$  is the dipole locking constant. As a capture theory, ADO theory assumes that the reaction is dominated by long-range intermolecular forces, and when the ion moves inside the maximum of the centrifugal barrier, the reaction always proceeds with unit efficiency. The ADO model predicts that both the ground and excited Be+ states react with a rate coefficient of  $4.1 \times 10^{-9} \text{ cm}^3/\text{s}$  at 100 K reaction temperature, roughly two times larger than measured for the ground state, but in agreement with the measured reaction rate of the excited state. However, because it is long-range, the ADO model cannot provide the branching ratio and state-dependent information and is therefore insufficient for describing the observed reactions.

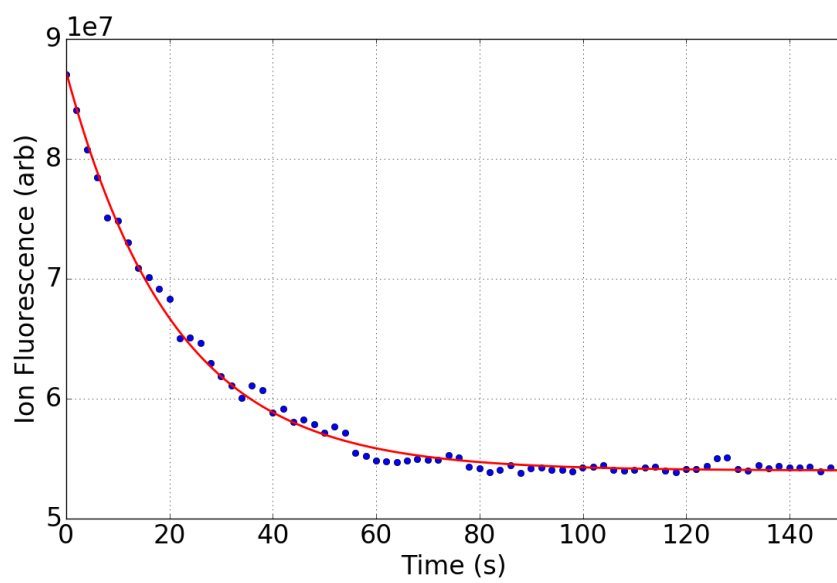


Figure 5.2:

# CHAPTER 6



## 6.1 Isotope-selective chemistry in the $\text{Be}^+(\text{^2S}_{1/2}) + \text{HOD} \longrightarrow \text{BeOD}^+ / \text{BeOH}$ H/D reaction

### 6.2 Abstract

Low temperature reactions between laser-cooled  $\text{Be}^+(\text{^2S}_{1/2})$  ions and partially deuterated water (HOD) molecules have been investigated using an ion trap and interpreted with zero-point corrected quasi-classical trajectory calculations on a highly accurate global potential energy surface for the ground electronic state. Both product channels have been observed for the first time, and the branching to  $\text{BeOD}^+ + \text{H}$  is found to be  $0.58 \pm 0.14$ . The experimental observation is reproduced by both quasi-classical trajectory and statistical calculations. Theoretical analyses reveal that the branching to the two product channels is largely due to the availability of open states in each channel.

### 6.3 Introduction

Together, isotope substitution and the measurement of the resulting product branching ratios provide important details about reaction dynamics and are often used to identify reaction pathways and understand bond-selective chemistry.[?, 10, 57] Important examples include X + HOD (X = H, F, Cl, O) reactions, where the branching ratios are experimentally controlled by selective excitation of the O–H or O–D bond.[41, 5, 30, 58, 45, 46, 15, 60, 42] It is now understood that a highly-accurate potential energy surface (PES) is crucial for performing

theoretical calculations of the product branching ratio, where subtle, difficult to identify, PES features have been found to significantly affect the results.[42]

A sophisticated understanding of radical-molecule reaction dynamics is continuing to develop from extensive experimental and theoretical studies. However, despite their importance in interstellar chemistry, where the isotopic branching ratios strongly influence the products of the interstellar cloud chemical network,far less progress has been made in the study of  $\text{H}_2^{14}$  ion–molecule reactions at low temperature. This is largely due to the challenges associated with both the experimental and theoretical approaches to these systems.[9, 12, 1, 3, 40, 43, 44] Experimental difficulties include a lack of quantum state preparation and readout techniques, while theoretical difficulties appear when treating dynamics dominated by the long range interaction between ions and molecules. Recently, several groups have employed cold ( mK) and fully-controlled laser-cooled trapped ions to address these experimental issues. For instance, isotope selectivity was probed in the reaction of laser-cooled  $\text{Mg}^+$  with  $\text{HD}$ ,and the  $\text{H}_2^{22}$  formation rate of  $\text{MgD}^+$  was found to be 5 times greater than  $\text{MgH}^+$ . This observation was ascribed to a dynamic mechanism in the exit channel of the reaction since statistical methods predict only a factor of approximately 2.[11] A similar experimental technique was applied to  $\text{Ca}^+ + \text{HD}$  reactions as well,[17] where the  $\text{CaD}^+$  channel was found to have 1.5 times higher population than the  $\text{CaH}^+$  channel; no detailed theoretical calculations have been performed for this system. With the help of laser-cooled ions, the initial quantum states are experimentally well controlled, but highly accurate PESs are still challenging to calculate with  $\text{Mg}^+$  or  $\text{Ca}^+$  ions due to the complexity of their electronic structures. The development of a more comprehensive understanding of ion–molecule reactions at low temperature will benefit from studies with less complex species that are amenable to theoretical treatment.

In this publication, we report a combined experimental and theoretical study of the effect of isotope substitution in an ion–polyatomic molecule reaction. A key objective is to understand the role of dynamics in such a reaction. Previous work on  $\text{Be}^+ + \text{H}_2\text{O}$  showed that chemical dynamics resulting from a submerged barrier strongly affect the reaction, leading to a reduction of the overall reaction rate from the capture limit. The overestimation

by the capture model was thus taken as a sign that this reaction is not completely statistical, despite the existence of a deep BeH<sub>2</sub>O<sup>+</sup> potential well along the reaction path. In this work, we probe the dynamics by examining the product branching ratio, which is presumably controlled by the exit channel barriers. Such a measurement is much more sensitive to the determination of the overall rates. Interestingly, here we find that the measured deuteration fraction of the ionic products is in good agreement with quasi-classical trajectory (QCT) calculations on the ground state PES. Furthermore, the branching ratio can be explained by a statistical model based on complete energy randomization in the long-lived transition complex.

## 6.4 Experimental

The apparatus employed here has been described in detail elsewhere. Briefly, laser ablation of metallic Be is used to produce Be<sup>+</sup> ions, which are trapped in a linear radio frequency Paul trap. Laser cooling[54] is used to cool the translational motion of the ions, resulting in a Coulomb crystal of Be<sup>+</sup> ions. A time-of-flight mass spectrometer (TOF-MS)[38, 37, 34, ?] is integrated into the Paul trap to analyze reaction products, allowing investigation of the isotope effect by mass spectrometry of the trapped ionic products. The 313 nm laser for cooling Be<sup>+</sup> ions allows manipulation of the Be<sup>+</sup> electronic quantum states; by tuning the frequency of this cooling laser, the fraction of ions in the <sup>2</sup>S<sub>1/2</sub> and <sup>2</sup>P<sub>3/2</sub> states can be precisely controlled. Promotion of the Be<sup>+</sup> to the <sup>2</sup>P<sub>3/2</sub> state opens more product pathways, as well as modifies existing product channels. HOD is made by mixing H<sub>2</sub>O and D<sub>2</sub>O.[?, ?] The gaseous room-temperature HOD/H<sub>2</sub>O/D<sub>2</sub>O mixture is then introduced via a leak valve into the trapping region for reaction with the trapped ions, the actual ratio of the mixture is measured from a Stanford Research Systems (SRS) residual gas analyzer (RGA). The RGA's fractionation of water was calibrated by introducing the water vapor into the chamber and integrating all resulting m/z signals. A typical scan reveals water fractionation products at *m/z* = 18, 17, and 16, which coincide with H<sub>2</sub>O<sup>+</sup>, OH<sup>+</sup>, and O<sup>+</sup>. The fractionation ratios of water are found by solving the system of equations:

$$P_{\text{H}_2\text{O}} = R_{18} + R_{17} + R_{16} \quad (6.1)$$

$$R_{18} = \alpha P_{\text{H}_2\text{O}} \quad (6.2)$$

$$R_{17} = \beta P_{\text{H}_2\text{O}} \quad (6.3)$$

$$R_{16} = \gamma P_{\text{H}_2\text{O}} \quad (6.4)$$

where  $R_i$  is the pressure reading from the RGA and  $P_{\text{H}_2\text{O}}$  is the true  $\text{H}_2\text{O}$  pressure. These fragmentation ratios were found to be  $\alpha = 0.768 \pm 0.006$ ,  $\beta = 0.184 \pm 0.006$  and  $\gamma = 0.068 \pm 0.002$ . The direct readings from analog scans with deuterated samples were then adjusted to account for the fractionation for each isotopologue.

$$P_{\text{H}_2\text{O}} = \frac{1}{\alpha} \left( R_{18} - \frac{\beta}{\alpha} R_{20} - \frac{\beta}{2\alpha} R_{19} \right) \quad (6.5)$$

$$P_{\text{HOD}} = \frac{R_{19}}{\alpha} \quad (6.6)$$

$$P_{\text{D}_2\text{O}} = \frac{R_{20}}{\alpha} \quad (6.7)$$

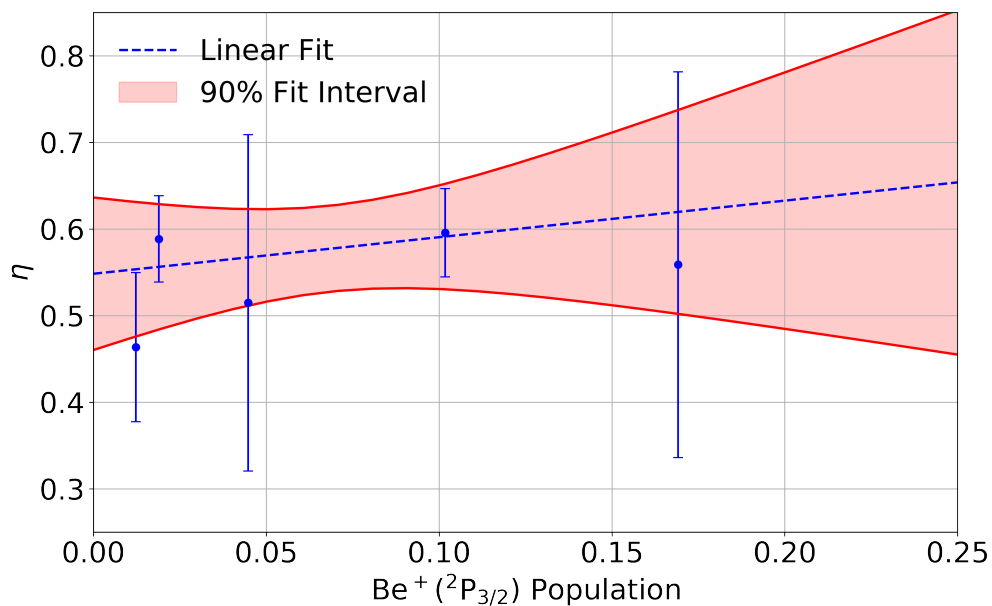


Figure 6.1:

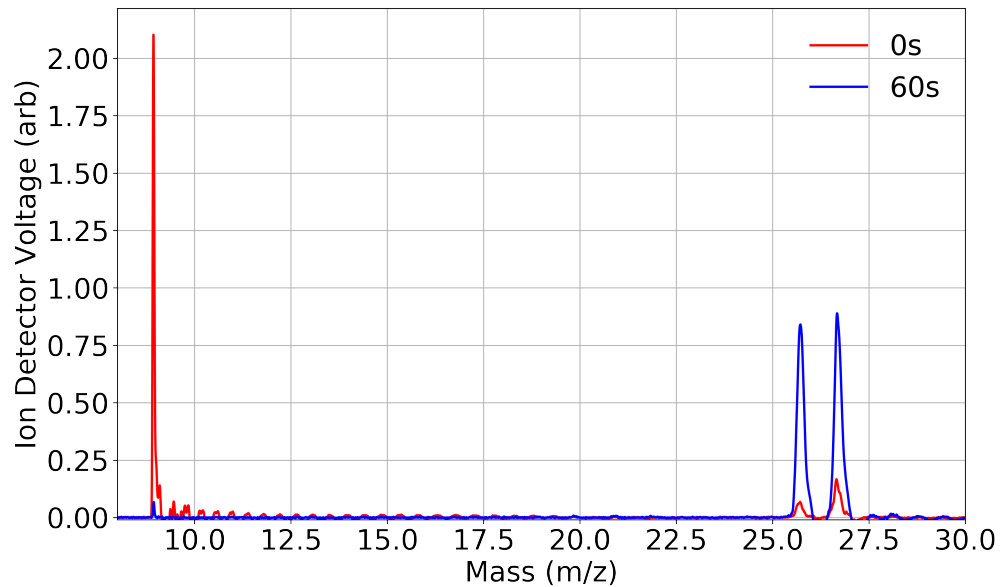


Figure 6.2:

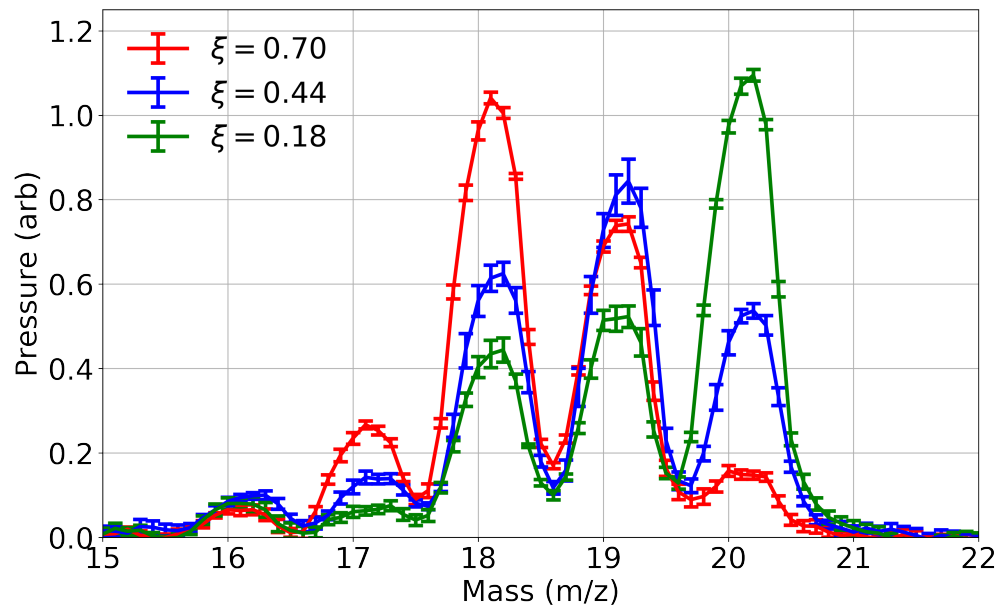


Figure 6.3:

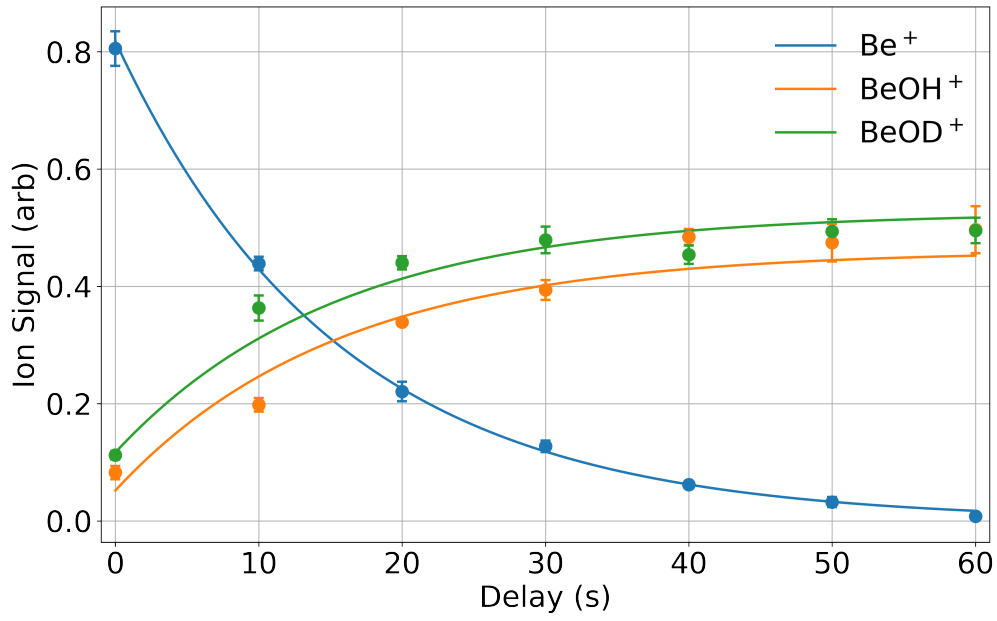


Figure 6.4:

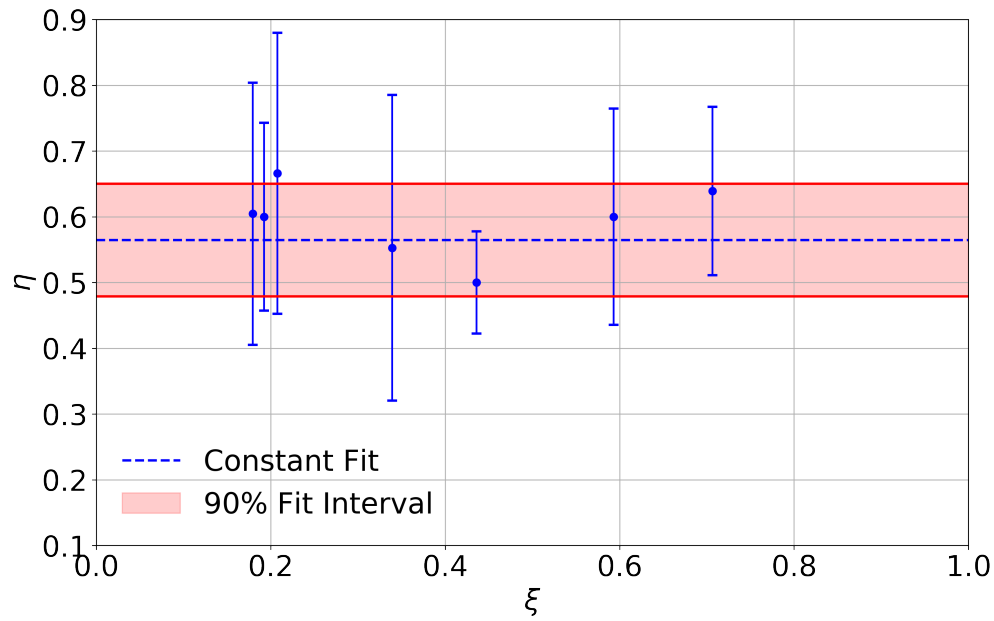
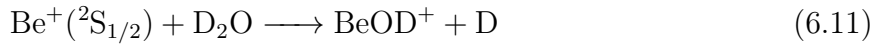
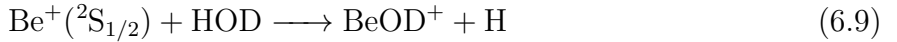
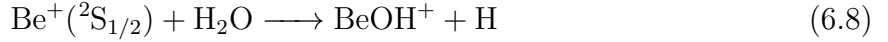


Figure 6.5:

## 6.5 Results and Discussion

Because the HOD sample also contains both H<sub>2</sub>O and D<sub>2</sub>O, the product BeOH<sup>+</sup> ( $m/z = 26$ ) has contributions of the reaction of the cation with H<sub>2</sub>O, while BeOD<sup>+</sup> ( $m/z = 27$ ) has contributions from reactions with D<sub>2</sub>O. The reactions of interest are:



Thus, the kinetics of the reagents and products are found from:

$$\dot{\text{Be}}^+(t) = (k_1\rho_1 + k_2\rho_2 + k_3\rho_3)\text{Be}^+(t) \quad (6.12)$$

$$\dot{\text{BeOH}}^+(t) = (k_1\rho_1 + (1 - \eta)k_2\rho_2)\text{Be}^+(t) \quad (6.13)$$

$$\dot{\text{BeOD}}^+(t) = (k_3\rho_3 + \eta k_2\rho_2)\text{Be}^+(t) \quad (6.14)$$

where  $k_i$  and  $\rho_i$  are the rate coefficient and density for  $\text{Be}^+$  reacting H<sub>2</sub>O, HOD, and D<sub>2</sub>O respectively. The branching ratio  $\eta \equiv k_{\text{BeOD}^+}/(k_{\text{BeOD}^+} + k_{\text{BeOH}^+})$  is the fraction of BeOD<sup>+</sup> produced from reactions (4.2) where  $k_j$  is the rate coefficient of species  $j$ . Solutions to the rate equations (4.4)–(4.6) are parameterized by the density measurements of the water isotopologues taken from a RGA, and a least-squares fit is taken over data sets of integrated TOF mass spectra with shared fitting parameters  $k_1$ ,  $k_2$ ,  $k_3$ , and  $\eta$ . In order to extract the pure  $\text{Be}^+(^2\text{S}_{1/2})$  and  $\text{Be}^+(^2\text{P}_{3/2})$ -state branching ratios, the process shown in Fig. 1(A)–(C) was repeated at different P-state fractions. The results are shown in Fig. 1(D) along with a least-squares linear-fit (blue line). The vertical intercept of this fit gives  $\eta_S = 0.56 \pm 0.03$  for the ground  $\text{Be}^+(^2\text{S}_{1/2})$  state reaction, while no conclusive dependence on P-state fractions is found within the confidence intervals. To further verify that our measurement is independent

of reagent ratios, we repeated the measurement for different mixtures of HOD, H<sub>2</sub>O, and D<sub>2</sub>O, as shown in Fig. 3. The branching ratio of BeOD<sup>+</sup> + H in reaction Be<sup>+</sup> + HOD (with 2% Be<sup>+</sup>(<sup>2</sup>P<sub>3/2</sub>) state population) is consistent over different hydrogen fractions in the gas. The fraction of hydrogen atoms in the chamber ( $\xi$ ) from all water isotopologues is defined by:

$$\xi = \frac{2\rho_{\text{H}_2\text{O}} + \rho_{\text{HOD}}}{\rho_{\text{H}_2\text{O}} + \rho_{\text{HOD}} + \rho_{\text{D}_2\text{O}}} \quad (6.15)$$

Weighted averaging of the fitted values over different mixtures then gives  $\eta = 0.58 \pm 0.14$ ,  $k_2/k_1 = 0.8 \pm 0.9$ ,  $\frac{k_3}{k_1} = 0.8 \pm 0.9$ . Despite the large error bars on the relative rate coefficients, due to the significant covariance of the rate coefficients,  $\eta$  is reasonably well determined. To further check our measurement of  $\eta$ , the process was repeated for shared fits with identical rate coefficients ( $k_1 = k_2 = k_3$ ) yielding  $\eta = 0.57 \pm 0.07$ . The calculated overall rate coefficients of the Be<sup>+</sup> + D<sub>2</sub>O and Be<sup>+</sup> + HOD reactions are  $(2.29 \pm 0.05) \times 10^{-9}$  cm<sup>3</sup> molecule<sup>-1</sup> s<sup>-1</sup> and  $(2.29 \pm 0.05) \times 10^{-9}$  cm<sup>3</sup> molecule<sup>-1</sup> s<sup>-1</sup>, respectively, which are slightly larger than that  $((2.02 \pm 0.04) \times 10^{-9}$  cm<sup>3</sup> molecule<sup>-1</sup> s<sup>-1</sup>)25 of the Be<sup>+</sup> + H<sub>2</sub>O reaction. The calculated  $k_2/k_1$  and  $k_3/k_1$  ratios are  $1.13 \pm 0.04$  and  $1.13 \pm 0.04$ , which are consistent with experimental values of  $0.8 \pm 0.9$  and  $0.8 \pm 0.9$ , respectively. The identical  $k_2/k_1$  and  $k_3/k_1$  ratios suggests the negligible isotopic effect in the thermal reaction probabilities of the Be<sup>+</sup> + D<sub>2</sub>O and Be<sup>+</sup> + HOD reactions. The branching ratio was determined using the QCT method for the Be<sup>+</sup> + HOD reaction. Specifically, the calculated branching fraction of Be<sup>+</sup> + HOD ( $\eta$ ) is  $0.61 \pm 0.02$ , which is in good agreement with experimental value  $0.58 \pm 0.14$ . The branching ratio of the two products (BeOD<sup>+</sup> and BeOH<sup>+</sup>) can be understood in terms of the PST model, which assumes complete energy randomization in the deep intermediate (BeHOD<sup>+</sup>) well. In Fig. 4, the branching fraction for the BeOD<sup>+</sup> + H channel is plotted as a function of the collision energy, which shows very weak temperature dependence. At the specific collisional temperature 100 K, the fraction obtained by integrating the energy dependent branching ratio with a Boltzmann weight is 0.67, which is in reasonable agreement with the QCT results.

To shed more light onto the preference of the  $\text{H} + \text{BeOD}^+$  channel in the  $\text{Be}^+ + \text{HOD}$  reaction, we provide a further analysis of the two important factors in determining the branching ratio. In PST, the reactivity in a particular product channel is controlled by the availability of open states, which is in turn dictated by the rovibrational states of the corresponding product molecule above the exit barrier formed by the centrifugal potential. Due to the heavier deuterium, it is readily understood that there are more rovibrational states for  $\text{BeOD}^+$  than  $\text{BeOH}^+$ . However, the availability of open channels is also constrained by the orbital angular momentum ( $l$ ), which erects a centrifugal barrier in both the reactant and product channels. The  $l$ -dependent centrifugal barrier is also isotope dependent, due to the difference in the reduced mass between the two products. The centrifugal barrier rises faster in the  $\text{BeOD}^+ + \text{H}$  channel than the  $\text{BeOH}^+ + \text{D}$  channel, due to the larger reduced mass of the latter. This is consistent with the fact that the branching fraction ( $\eta$ ) of  $\text{BeOD}^+ + \text{H}$  channel becomes larger when the centrifugal barrier was not considered (shown in Fig. 4). These two factors have opposing effects on the branching ratio, but the higher density of states in the  $\text{BeOD}^+$  molecule dominates, at least at low energies. As a result, the  $\text{H} + \text{BeOD}^+$  product channel is strongly favored. The good agreement of the statistical model with both the experimental and QCT results in branching ratio suggests that the reaction is largely statistical. In addition, the DCSs of the  $\text{Be}^+ + \text{H}_2\text{O}/\text{HOD}/\text{D}_2\text{O}$  reactions calculated by the QCT method are shown in Fig. 5. It can be seen from the figure that the DCSs of all three reactions are roughly forward-backward symmetric, due to the long-lived intermediates formed in the reactions. The forward-backward symmetry in DCSs suggests the statistical nature of the reaction, which further validates the suitability of the PST model discussed above.

## 6.6 Conclusion

To summarize, chemical reactions between  $\text{Be}^+(^2\text{S}_{1/2})$  and HOD have been investigated using an integrated ion trap and highresolution TOF-MS and ZPE corrected QCT calculations on an accurate global PES. Two product channels have been observed and the branching to

$\text{BeOD}^+ + \text{H}$  is accurately determined to be  $0.58 \pm 0.14$ . The experimental result is in good agreement with ZPE corrected QCT calculation result ( $0.61 \pm 0.02$ ) as well as close to the statistical PST model ( 0.67), which reveals that the branching to the two product channels is largely due to the availability of different open states in each channel. Since their rate coefficients deviate from the capture limit as reported in our earlier work, it is clear that the  $\text{Be}^+(2\text{S}_{1/2}) + \text{H}_2\text{O}/\text{D}_2\text{O}/\text{HOD}$  reactions have a non-negligible non-statistical component. Interestingly, however, the good prediction of the branching ratio by the statistical model discussed above suggests that the formation of the products is largely statistical. This conclusion is further supported by the forward–backward symmetry of the calculated DCSs.

## 6.7 Notes

We mix "equal" amounts of  $\text{H}_2\text{O}$  and  $\text{D}_2\text{O}$  and leave it overnight to produce roughly 1:2:1 ratio of  $\text{H}_2\text{O}:\text{HOD}:\text{D}_2\text{O}$  as roughly verified by the RGA. If we consider being a singular oxygen atom looking at a sea of  $\text{H}_2\text{O}$  and  $\text{D}_2\text{O}$ , it has a 1/4 probability of grabbing H or D twice. It then has a 1/2 chance of grabbing an H and D in either order, which gives us the 1:2:1 ratio.

To generalize this, we can write the fraction of  $\text{H}_2\text{O}$  in the sample to be  $\gamma$  and the  $\text{D}_2\text{O}$  to be  $1 - \gamma$ . The probabilities of yielding any combination is then found quickly:

$$\text{H}_2\text{O} = \gamma^2 \quad (6.16)$$

$$\text{HOD} = 2\gamma(1 - \gamma) \quad (6.17)$$

$$\text{D}_2\text{O} = (1 - \gamma)^2 \quad (6.18)$$

For the sake of readability, let  $(\text{H}_2\text{O}, \text{HOD}, \text{D}_2\text{O})$  be represented as  $(1, 2, 3)$  respectively.

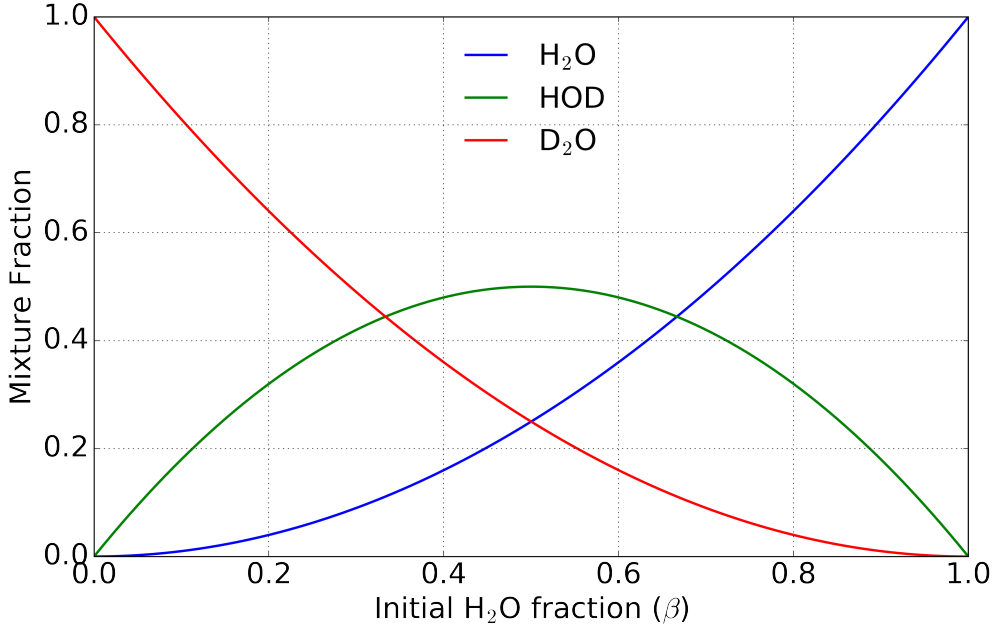


Figure 6.6:

Reading water with an RGA causes some known fractionation, where the  $H_2O$  is broken into its constituents, including  $OH^+$  and  $O^+$ . We expect then to see a lower mass 18 peak than normal, to truly know what the ratios are, we have to calibrate the RGA ourselves.

Possible fractionation pathways:

$$P'_{18} = \alpha P_{H_2O} + \beta \left( \frac{P_{HOD}}{2} + P_{D_2O} \right) \quad (6.19)$$

$$P'_{19} = \alpha P_{HOD} \quad (6.20)$$

$$P'_{20} = \alpha P_{D_2O} \quad (6.21)$$

$$P'_{17} = \beta \left( \frac{P_{HOD}}{2} + P_{H_2O} \right) \quad (6.22)$$

$$P'_{16} = \gamma (P_{H_2O} + P_{HOD} + P_{D_2O}) \quad (6.23)$$

$$1 = \alpha + \beta + \gamma \quad (6.24)$$

By solving this system of equations, we get 76.8% of the real value as cited by the RGA program itself; this is also true for HOD and  $D_2O$ . Of that lost 23.2%, 18.4% goes to  $OH^+$ ,

but for the isotopogues of HOD and D<sub>2</sub>O, we would need to consider which mass signal it will add to. No other mode of fractionation will contribute to the other water isotopologue peaks

$$P'_1 = \alpha P_1 + \beta P_3 + \frac{\beta}{2} P_2 \quad (6.25)$$

$$P'_2 = \alpha P_2 \quad (6.26)$$

$$P'_3 = \alpha P_3 \quad (6.27)$$

Where we let  $\alpha = 0.744$  and  $\beta = 0.256$  per the SRS RGA software. Where P is the real pressure accounting for fractionation, and P' is the raw observed pressure value. Solving for the real pressure, we find:

$$P_1 = \frac{1}{\alpha} \left( P'_1 - \frac{\beta}{\alpha} P'_3 - \frac{\beta}{2\alpha} P'_2 \right) \quad (6.28)$$

$$P_2 = \frac{P'_2}{\alpha} \quad (6.29)$$

$$P_3 = \frac{P'_3}{\alpha} \quad (6.30)$$

## 6.8 Be<sup>+</sup> + HOD branching ratio

Now that we can characterize the pressures in the chamber more accurately, we then consider the possible reactions between the Be<sup>+</sup> and water isotopologues:



Which can then be written as a system of differential equations.

$$\dot{Be}(t) = -(k_1\rho_1 + k_2\rho_2 + k_3\rho_3)Be(t) \quad (6.35)$$

$$\dot{BeOH}(t) = (k_1\rho_1 + (1 - \eta)k_2\rho_2)Be(t) \quad (6.36)$$

$$\dot{BeOD}(t) = (k_3\rho_3 + \eta k_2\rho_2)Be(t) \quad (6.37)$$

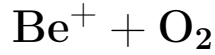
We are interested in reactions 6.32 and 6.33 and the ratio between the two ( $\eta$ ), which is not directly found from the ratio of the production rates of the two ions. Since this is a ratio, we don't need to concern ourselves with calculating the density ( $\rho$ ), the RGA pressure is fine.

$$\beta \equiv \frac{\dot{BeOD}}{\dot{BeOH}} = \frac{k_3P_3 + \eta k_2P_2}{k_1P_1 + (1 - \eta)k_2P_2} \quad (6.38)$$

$$\eta = \frac{\beta(k_1P_1 + k_2P_2) - k_3P_3}{k_2P_2(1 + \beta)} \quad (6.39)$$

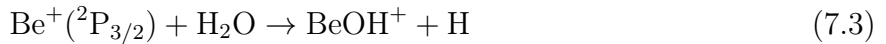
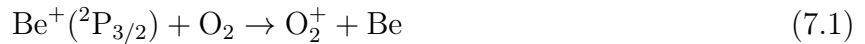
The theorists found that the statistical value of the reaction is around 3, but with dynamics, tends towards  $\frac{\eta}{1-\eta} = 1.7$  or  $\eta = 0.63$  for  $\text{Be}^+(\text{S})$ .

## CHAPTER 7



Beryllium metal is ablated with an Nd:YAG laser and trapped in a linear Paul trap. Laser cooling is applied with a 313nm laser. Pure O<sub>2</sub> gas is introduced into the chamber via leak valve to react with the ions. Remaining reactants and charged reaction products are ejected into a time-of-flight mass spectrometer (TOF) where the various masses of ions can be determined.

When the Be<sup>+</sup> is excited from the <sup>2</sup>S<sub>1/2</sub> to the <sup>2</sup>P<sub>3/2</sub> manifold, we find the energetically allowed channels to be:



Without excitation into the <sup>2</sup>P<sub>3/2</sub> manifold, reactions 7.1 and 7.2 are endothermic by 2.75eV and 1.1eV, respectively.

Despite the fact that reaction 7.2 is energetically allowed, it is never seen with laser cooling.

Without 313nm light, the Be<sup>+</sup> ions stay in the <sup>2</sup>S<sub>1/2</sub> ground state, but with a ion trap depth > 4eV, there are portions of the ion cloud with enough energy to still proceed with the production of BeO<sup>+</sup>. Without the laser cooling, we observe the disappearance of BeO<sup>+</sup>

from the trap due to exciting the molecule into a pre-dissociative state.

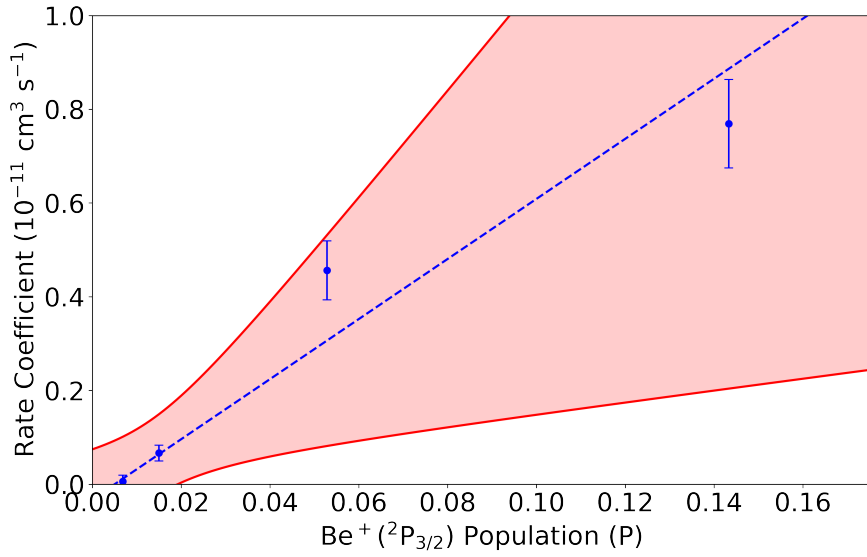


Figure 7.1: A linear dependence on the rate constant for reaction 7.1 as a function of P state excitation.  $k = (6 \pm 1) \times 10^{-11}P + (-0.03 \pm 0.16) \times 10^{-11}$

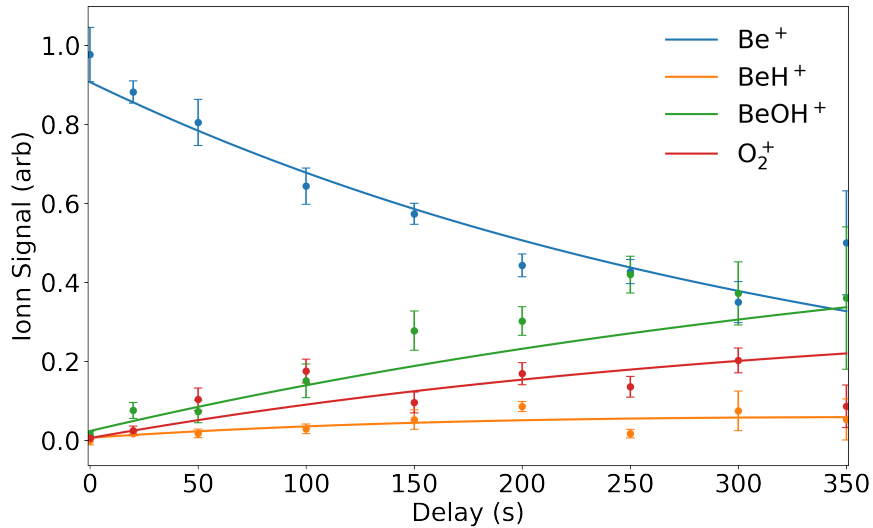


Figure 7.2: Shared fitting of trapped products with 14% p-state excitation.

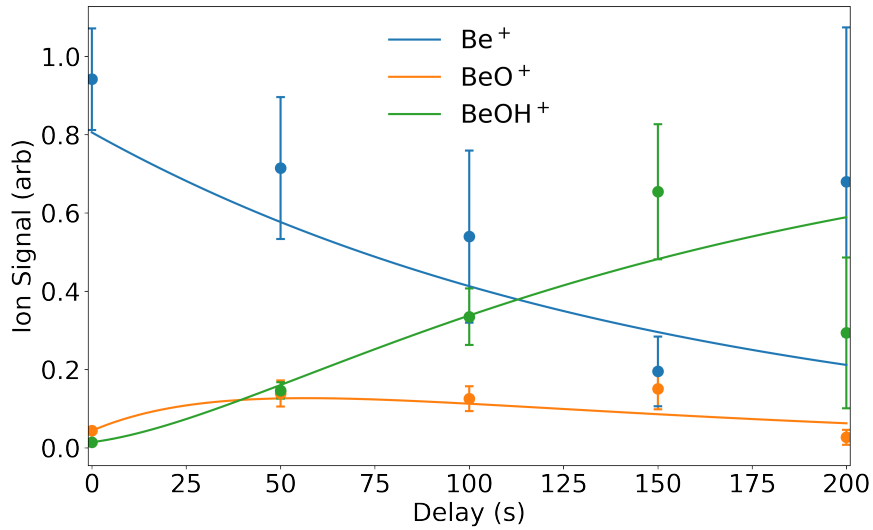


Figure 7.3: Shared fitting of trapped products with 14% p-state excitation.

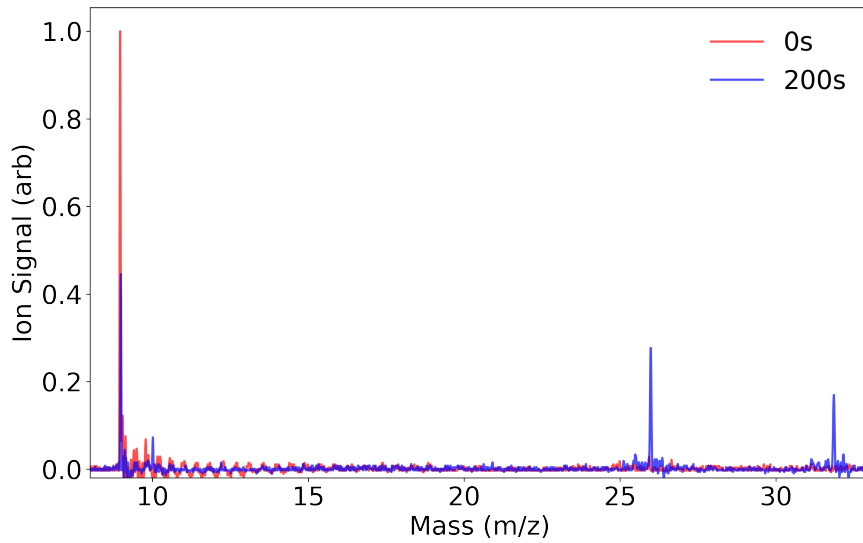


Figure 7.4: TOF traces for data taken with 14% p-state excitation at 0s and 200s showing no products at 0s, but distinct peaks for reaction products  $\text{BeH}^+$ ,  $\text{BeOH}^+$ , and  $\text{O}_2^+$ .

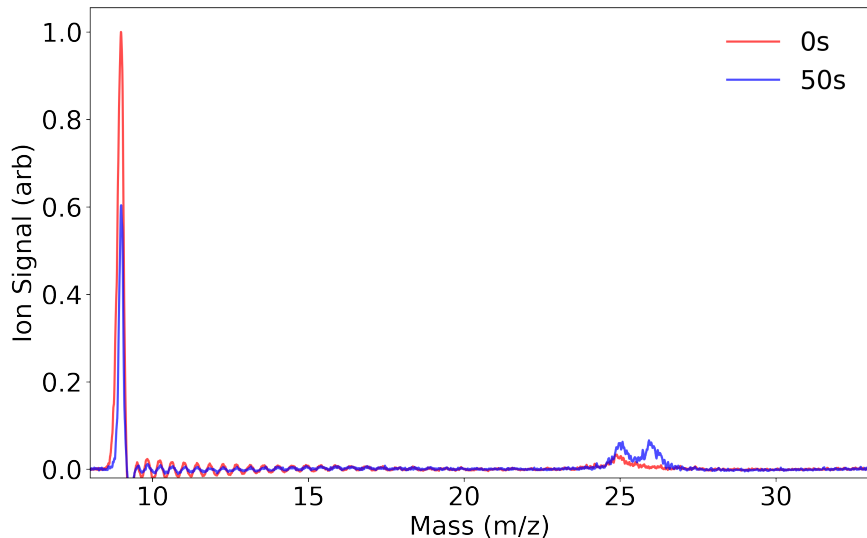
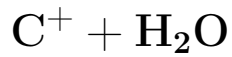


Figure 7.5: TOF traces for data taken with 14% p-state excitation at 0s and 200s showing no products at 0s, but distinct peaks for reaction products  $\text{BeH}^+$ ,  $\text{BeOH}^+$ , and  $\text{O}_2^+$ .

Considering state counting, reactions ?? and ?? have been measured to have branching ratios that vary from 60:40 ( $\text{CO}^+:\text{O}^+$ ) to 30:70 in the other direction. By looking at experimental data as well as the theoretical state counting, we find the ratio to be pretty definitively 60:40.

# CHAPTER 8



## 8.1 Formyl Isomer Branching Ratio

With our dual ablation system, we can reliably co-trap carbon and beryllium ions and introduce cold molecules from the CBGB. Introducing water entrained in a cold neon buffer gas beam, we can see the reaction products due to these collisions. The internal temperature of the buffer gas in the beam is verified to be, which is defined by the temperature of the inner cell.

We do not expect any reactions to occur with the cold neon buffer gas. We have experimentally verified the absence of new mass peaks when introducing neon into the system with carbon and beryllium ions, only an overall loss rate attributed to elastic collisions within the trap.

Add  
graphs  
of  
flu-  
o-  
res-  
cence  
de-  
cay

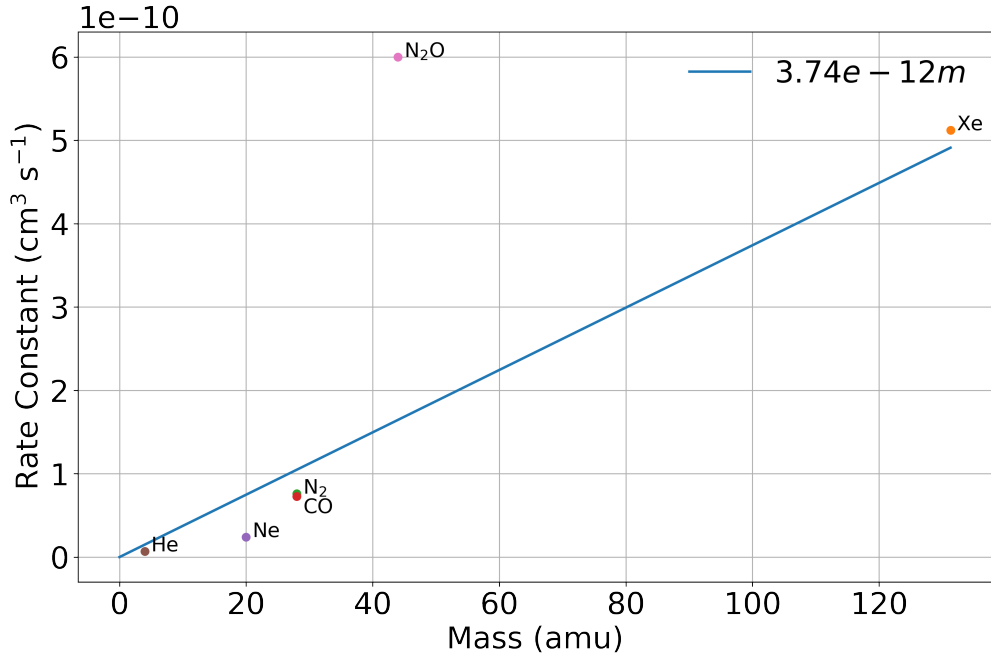


Figure 8.1: Gasses

Conversely, the water molecules will react readily with both beryllium and carbon ions, where the prevailing beryllium reactions are eqs. (5.1) to (5.3). Considering the known reaction products of  $\text{C}^+ + \text{H}_2\text{O}$ :



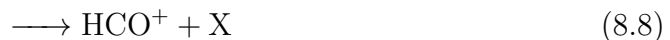
$$\text{C}(t) = \text{C}_0 e^{-k_1 \rho t} \quad (8.4)$$

$$[\text{HCO}](t) = \frac{e^{-(k_1+k_2)\rho t}}{k_1 - k_2} (e^{k_1 \rho t} ((\text{C}_0 + [\text{HCO}]_0)k_1 - [\text{HCO}]_0 k_2) - \text{C}_0 e^{-(k_1+k_2)\rho t}) \quad (8.5)$$

$$\text{H}_3\text{O}(t) = \text{H}_3\text{O}_0 + [\text{HCO}]_0 (1 - e^{-k_2 \rho t}) + \frac{\text{C}_0 (k_1 (1 - e^{-k_2 \rho t}) + k_2 (e^{-k_1 \rho t} - 1))}{k_1 - k_2} \quad (8.6)$$

We want to probe the branching ratio of the formyl isomers formed in reactions 8.1 and 8.2 at low temperatures. At room temperatures, the branching ratio has been found to be approximately 84:16 ( $\text{COH}^+$ : $\text{HCO}^+$ )[14], but unexplored at lower regimes.

By definition, these formyl isomers of reactions eqs. (8.1) and (8.2) have identical mass and thus, cannot be readily read off by the TOF system. To be able to separate the isomer products, we need to be able to separate their masses. By introducing a gas into the system with a proton affinity in between the isomer products, we may selectively react only one the less stable  $\text{COH}^+$  isomer. This also yields a distinct  $m/z$  peaks due to each isomer. By using an external gas, we are doing an indirect measurement, and as such, it may add unintended complications. Certain gasses are more reactive and may react with the excited  $\text{Be}^+$ ,  $\text{C}^+$ , or any other ionized species in the trap. Another possibility is that the  $\text{COH}^+$  may isomerize due to interactions with the gas(8.7).[13]



	Affinity (kcal/mol)
CO*	427
Kr	425
HF	490
N <sub>2</sub>	495
Xe	496
NO	531
CO <sub>2</sub>	548
CH <sub>4</sub>	552
HCl	564
HBr	569
N <sub>2</sub> O	571
*CO	594

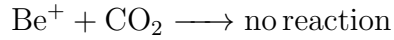
Table 8.1: Proton affinities of gasses between formyl isomers where (\*) indicates H bonding location.

Previous literature utilized gasses such as NO, CH<sub>4</sub>, N<sub>2</sub>O, and Kr to perform similar titrations. Kr, and Xe are inert and would not react with any other trapped ion but are too heavy to reliably trap after a reaction. NO is caustic and will ruin the vacuum chamber if introduced, and thus was avoided. Attempts were made with N<sub>2</sub>O and well as CH<sub>4</sub>, but both had issues. N<sub>2</sub>O rapidly reacts with Be<sup>+</sup> and made reliable TOF traces unattainable due to the loss of coolant ion. CH<sub>4</sub> readily reacted with most of the ions in the trap to produce a multitude of mass peaks, greatly complicating the analysis. At the end, success was found with CO<sub>2</sub> and <sup>15</sup>N<sub>2</sub>.

## 8.2 CO<sub>2</sub> Titration

From table 8.1, we see that CO<sub>2</sub> is a viable option to titrate the reaction products. The possible reactions of CO<sub>2</sub> with Be<sup>+</sup> are unknown in literature, but found to be non-reactive

in both ground and excited states, while  $\text{C}^+$  readily reacts.



Testing the purity of the  $\text{CO}_2$ , I introduce the  $\text{CO}_2$  into the ion chamber with the RGA.

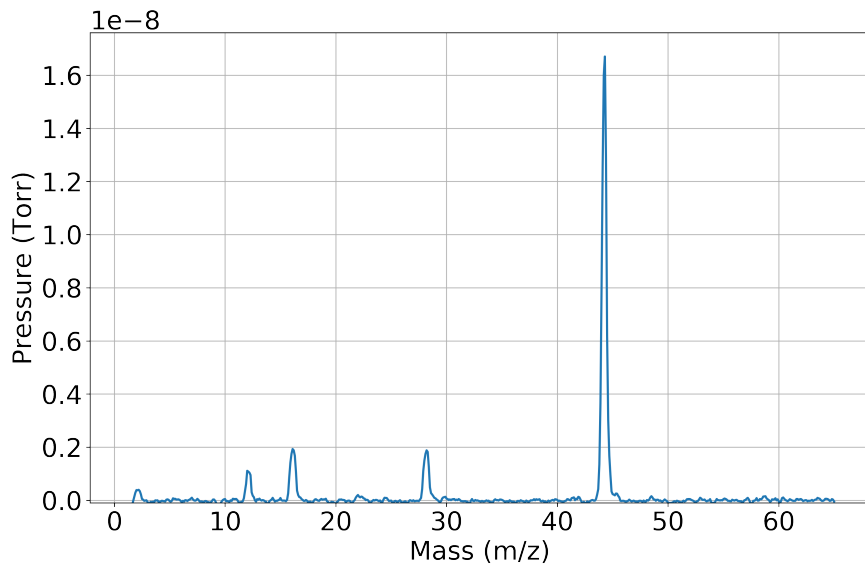


Figure 8.2: RGA showing purity of  $\text{CO}_2$  introduced into chamber. Ratios of  $\text{CO}_2$  peaks at  $m/z = 12, 16, 28$ , and  $44$  in agreement with table 8.2, with no conclusive evidence of contamination by any other gas.

m/z	Fraction
44	0.85
28	0.05
16	0.05
12	0.012

Table 8.2: RGA fractionation of CO<sub>2</sub> as given by  
<http://ytonline.com/technical-information/rga-spectra-data-fragmentation-factor/>

### 8.2.1 Be<sup>+</sup> + CO<sub>2</sub>

Introducing the CO<sub>2</sub> into the ion chamber to react with only laser cooled Be<sup>+</sup>, The TOF only shows that there are trace amounts of H<sub>2</sub>O in the chamber, with no indication of any further loss due to the inclusion of CO<sub>2</sub>.

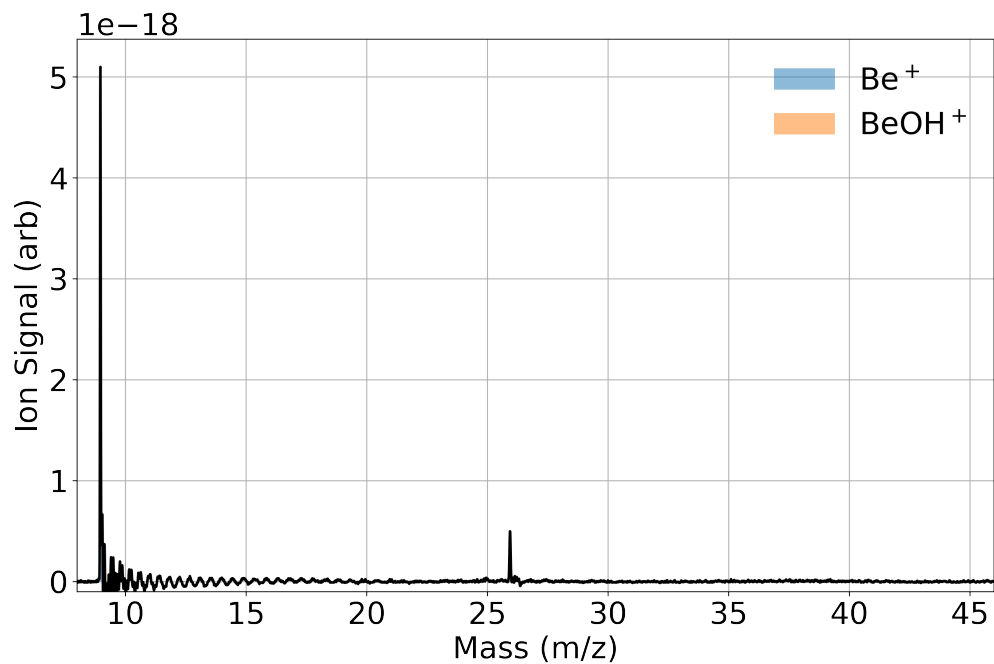


Figure 8.3: TOF trace of laser-cooled Be<sup>+</sup> reacting with  $\approx 1 \times 10^{-8}$  Torr CO<sub>2</sub> introduced via leak valve for 50 seconds.

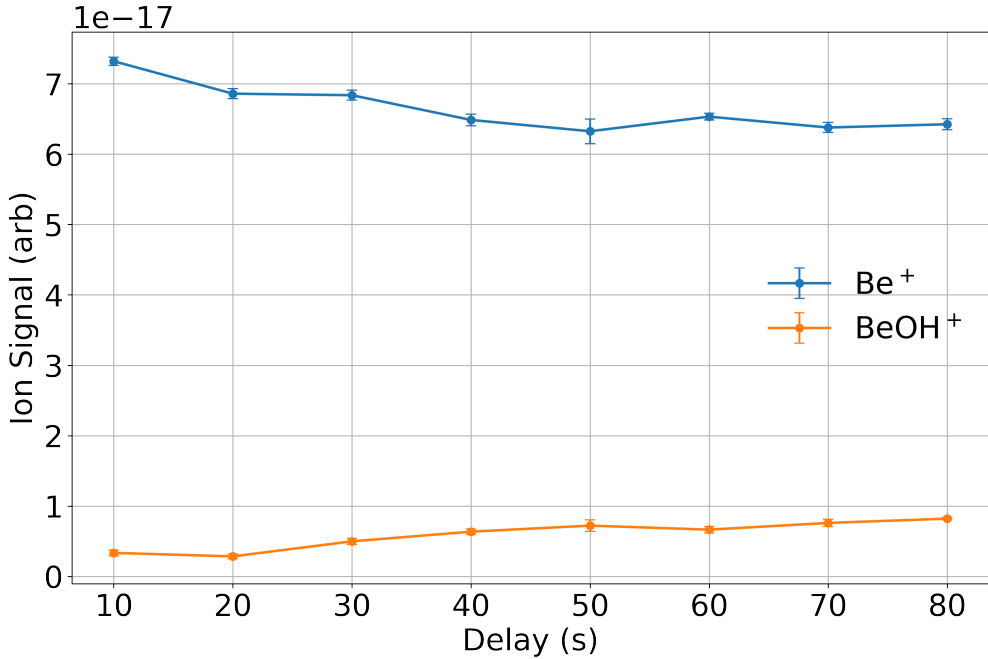


Figure 8.4: Integrated ion signal of individual TOF traces normalized by  $\text{Be}^+$  fluorescence at various  $\text{CO}_2$  exposure times.

We see that there aren't any reactions happening between  $\text{Be}^+$  and  $\text{CO}_2$ , while there is a little bit of water in the leak valve, which was baked afterwards. This does indicate that there are also no reactions between  $\text{BeOH}^+$  and  $\text{CO}_2$ .

### 8.2.2 $\text{C}^+ + \text{CO}_2$

By ablating both  $\text{C}^+$  and  $\text{Be}^+$  into the trap and introducing  $\text{CO}_2$  via the leak valve, we find the expected reactions 8.10, 8.11, and 8.12 as well as unexpected peaks appearing at  $m/z = 15, 29$ , and  $45$ .

Labels in figures sections 8.2.2 and 8.2.2 are of predicted chemicals coinciding with the masses. The initial guess is that there is  $\text{H}_2\text{O}$  in the leak valve, as we saw it before in the  $\text{Be}^+ + \text{CO}_2$  reaction, but the leak valve region was baked since that data was taken. Similarly, if there was water, we would see a peak at  $m/z = 26$ , coinciding with  $\text{BeOH}^+$ , which we do not see, we should also expect to see an abundance of  $\text{H}_3\text{O}^+$  due to reactions between the

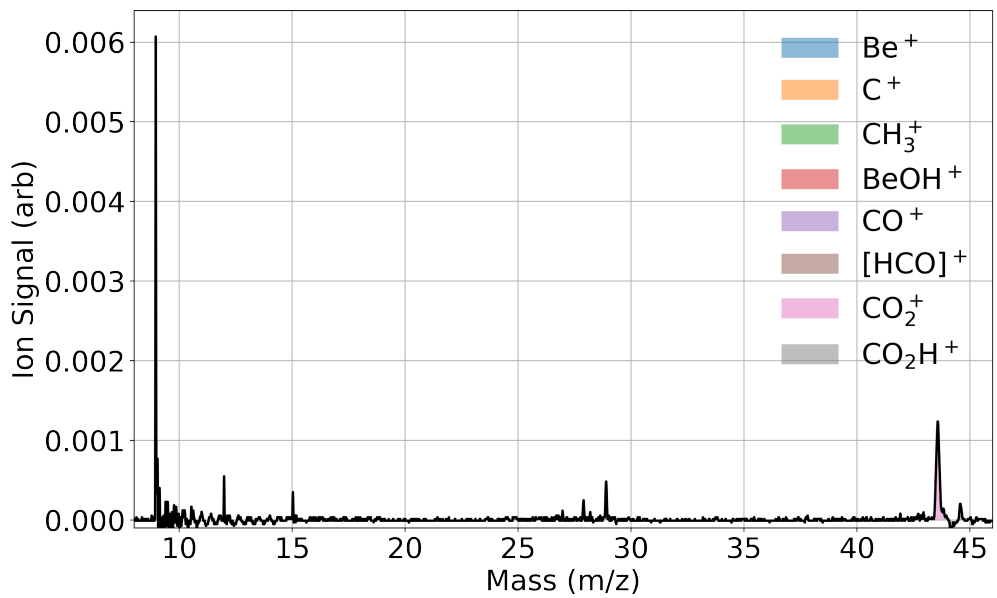


Figure 8.5: TOF trace of laser-cooled  $\text{Be}^+$  and  $\text{C}^+$  reacting with  $\approx 1 \times 10^{-8}$  Torr  $\text{CO}_2$  introduced via leak valve for 40 seconds.

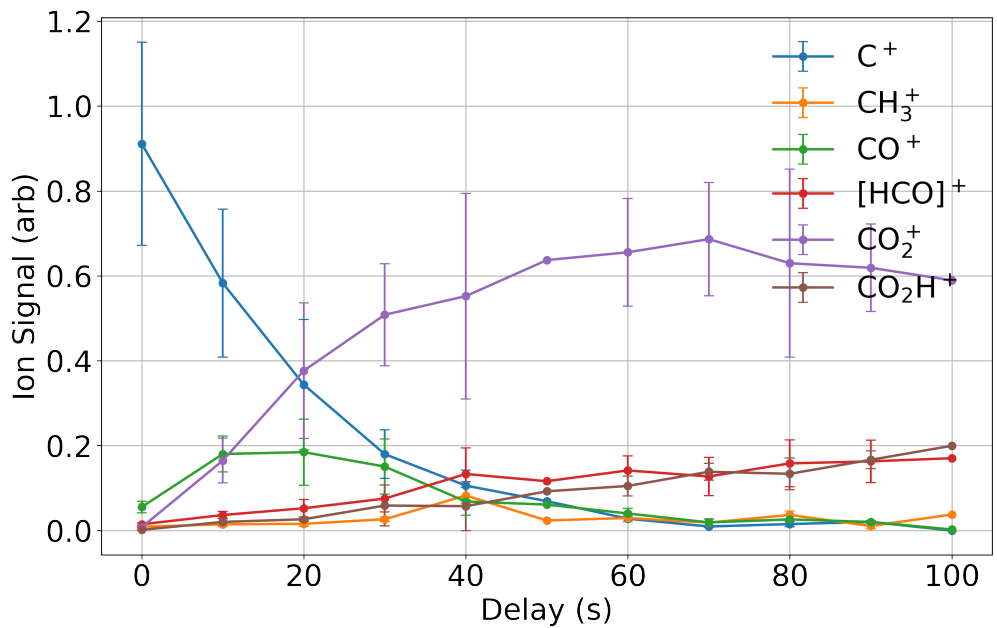


Figure 8.6: Integrated ion signal of individual TOF traces normalized by total ion signal excluding  $\text{Be}^+$  at various  $\text{CO}_2$  exposure times.

alleged  $[HCO]^+$  and  $CO_2H^+$ , which we also do not see. But, the peak at 45 could possibly be explained by  $H_2O$  in reaction 8.14, while 29 could be due to reactions 8.2 and 8.1. But there are no reactions with  $H_2O$  for the production of 15.



I still doubt that the 29 mass is due to  $C^+$  directly reacting with  $H_2O$  because the traces clearly show it increasing despite the depletion of  $C^+$ , indicating it is a second order reaction. It wouldn't be  $H_2$  either, because we would see  $BeH^+$  in the trap, as well as many other peaks associated with  $C^+ + H_2$  including 14, 16, and 17.

### 8.2.3 $Be^+ + C^+ + H_2O$ with $CO_2$

Water is introduced into the chamber via the CBGB with the cell held at a temperature of 20K. After  $(10 \pm 1)$  seconds of exposure, the gate valve is closed and  $CO_2$  is leaked in to react away the formyl isomers such that  $\approx 99\%$  are reacted away (determined by the disappearance of  $C^+$ ).

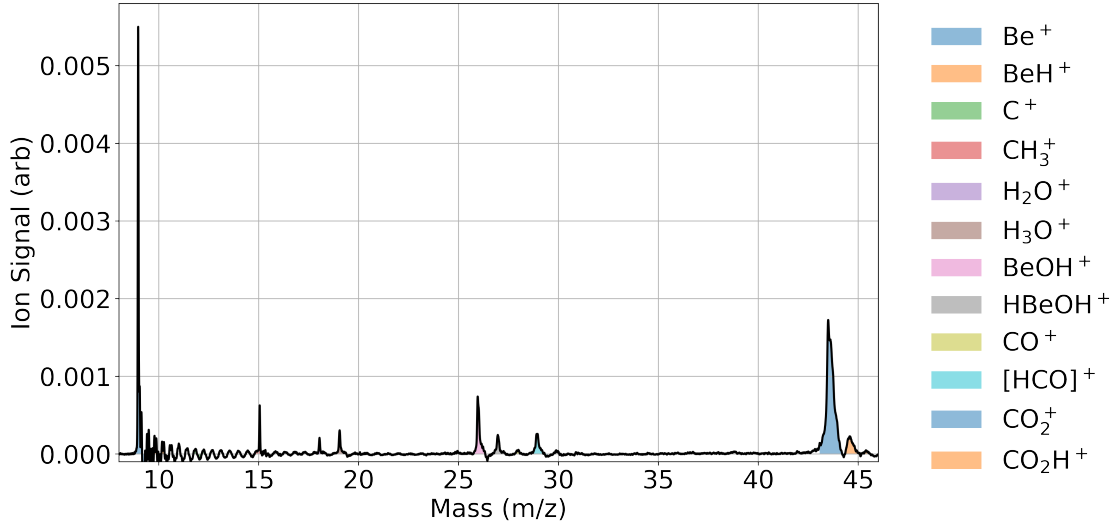


Figure 8.7:  $\text{C}^+$  and  $\text{Be}^+$  loaded into the trap is reacted with  $\text{H}_2\text{O}$  introduced from the beam. The gate valve is closed after 10 seconds and  $\text{CO}_2$  is introduced via leak valve so that the  $\text{COH}^+$  is titrated into  $\text{CO}_2\text{H}^+$ .

Knowing the anomalous peaks in the previous tests, the peaks of interest are not exclusively the branching ratio between the formyl isomers, where we define  $\gamma$  as the fraction of products that produce  $\text{COH}^+$ .

Solving the differential equations of the  $\text{C}^+ + \text{H}_2\text{O}$  reactions (eqs. (8.2), (8.1) and (8.3)), we may derive the equations of the ion reactions:

We define the ratio of the formyl isomers and remaining  $\text{C}^+$

$$\alpha(t) \equiv \frac{[\text{HCO}](t)}{[\text{HCO}](t) + [\text{C}](t)} \quad (8.16)$$

In the data taken, we introduced the water in the beam for approximately 10s, the fraction of  $\text{C}^+$  that has turned into  $[\text{HCO}]^+$  is thus  $\alpha = 0.37 \pm 0.02$ . Considering that after titration with  $\text{CO}_2$ , the fraction of the remaining 63% of  $\text{C}^+$  has turned into equal amounts of  $m/z = 29, 45$  defined as  $\beta = 0.17 \pm 0.02$ .

$$N_C(0) = N_0 \quad (8.17)$$

$$N_C(\tau_1) = (1 - \alpha(\tau_1))N_0 \quad (8.18)$$

$$N_{29}(\tau_1) = \alpha(\tau_1)N_0 \quad (8.19)$$

Where  $N_C(t)$  is the amount of  $\text{C}^+$  is in the trap after being exposed to either the water beam or  $\text{CO}_2$  for time  $t$ .  $\tau_1$  is the amount of time where the ions are exposed to the water beam, where  $\alpha$  is the proportion of  $\text{C}^+$  that is converted to  $m/z = 29$ , which in our case is 0.37. We then introduce the  $\text{CO}_2$  into the system and yield:

$$N_C(\tau_1 + \tau_2) = 0 \quad (8.20)$$

$$N_{29}(\tau_1 + \tau_2) = N_{29}(\tau_1)(1 - \gamma) + N_C(\tau_1)\beta \quad (8.21)$$

$$= N_0(\alpha(1 - \gamma) + \beta(1 - \alpha)) \quad (8.22)$$

$$N_{45}(\tau_1 + \tau_2) = N_{29}(\tau_1)\gamma + N_C(\tau_1)\beta \quad (8.23)$$

$$= N_0(\alpha\gamma + \beta(1 - \alpha)) \quad (8.24)$$

In conjunction with the ratio  $\eta \equiv \frac{\text{CO}_2\text{H}^+}{\text{CO}_2\text{H}^+ + \text{HCO}^+} = 0.55 \pm 0.02$

$$\eta = \frac{N_{45}(\tau_1 + \tau_2)}{N_{29}(\tau_1 + \tau_2) + N_{45}(\tau_1 + \tau_2)} \quad (8.25)$$

But we know that there are contributions to both masses of interest due to the inclusion of the  $\text{CO}_2$ , thus, we need to solve for  $\gamma$ :

$$\eta = \frac{\beta - \alpha\beta + \alpha\gamma}{\alpha + 2\beta - 2\alpha\beta} \quad (8.26)$$

$$\gamma = \frac{1}{\alpha}(\alpha\eta + \beta(\alpha + 2\eta - 2\alpha\eta - 1)) \quad (8.27)$$

Using equation 8.27, we find at the true branching ratio is scaled from  $0.55 \pm 0.03$  to  $0.58 \pm 0.05$ .

## 8.3 $^{15}\text{N}_2$ Titration

Normally  $\text{N}_2$  would not be a good choice, due to the fact that  $\text{N}_2\text{H}^+$  has the same mass as the formyl isomers at  $m/z = 29$ , but we may instead introduce  $^{15}\text{N}_2$  to produce a new peak at  $m/z = 31$ .

### 8.3.1 Estimate Isomerization

To estimate a limit on the isomerization, we consider the above reaction eqs. (8.8) and (8.7), where  $\text{X} = ^{15}\text{N}_2$  in the context that we can only determine the abundance of  $[\text{HCO}]^+$  and  $^{15}\text{N}_2\text{H}^+$ . As a function of pressure, we cannot see reaction 8.8, but if it does contribute, we should see a discrepancy in the total rate constant, which we estimate to be Langevin:  $k_L = 8.0 \times 10^{-10}$ . The functional form is as follows:

$$\eta(t) = C(1 - e^{-k_{8.7}\rho t}) \quad (8.28)$$

Where we define  $\eta(t) \equiv \frac{^{15}\text{N}_2\text{H}^+(t)}{^{15}\text{N}_2\text{H}^+(t) + [\text{HCO}]^+(t)}$

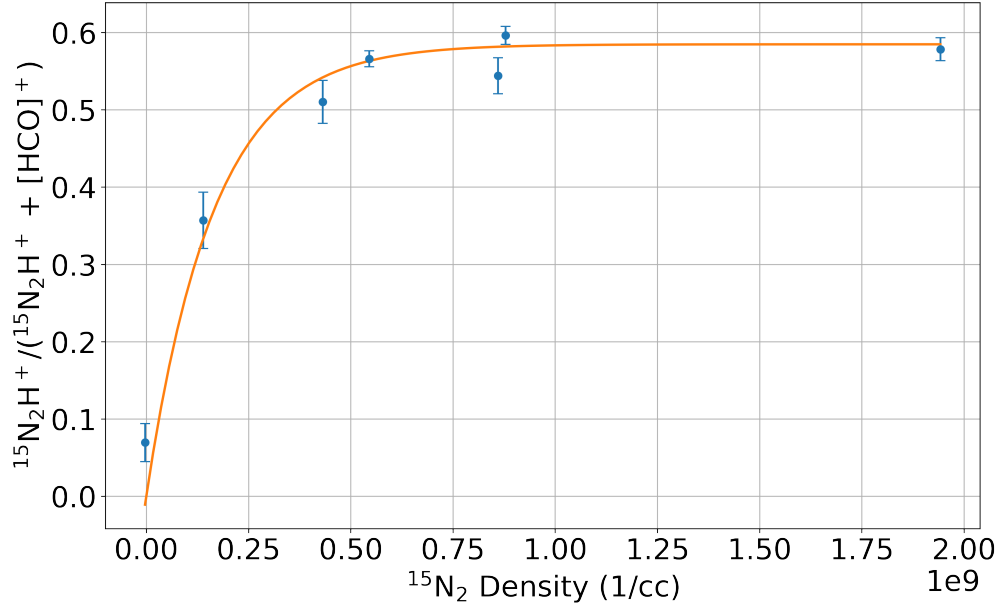


Figure 8.8:  $C = 0.58 \pm 0.02$   $k_{8.7} = ((6.1 \pm 1.5) \times 10^{-10}) \text{ cm}^3/\text{s}$

# CHAPTER 9

## Conclusion and Future Outlook

The experiment has broken new ground in ion-molecule reactions at various reaction temperatures, but there is still much left unexplored. The recent inclusion of two Lioptec dye lasers will allow for more stuff and stuff.

Also stereodynamics with molecules or just atoms

We have only been exciting the  $\text{Be}^+$  into the  ${}^2\text{P}_{3/2}$  state because it is easier than the  ${}^2\text{P}_{1/2}$  manifold, but that would allow us to possibly see fine structure dependent rates and dynamics.

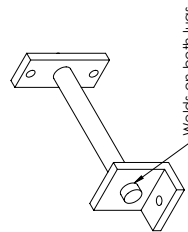
## **APPENDIX A**

### **CBGB Drawings**

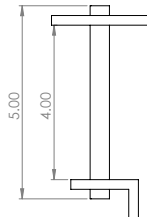
## 4K\_thermal\_link

Campbell Lab Attn: Gary Chen  
301-206-6782

gchen@physics.ucla.edu



Lengths are approximate



Tolerance:  $X_{XXX} = +/- 0.05$   
 $X_{XXX} = +/- 0.005$

Material: Cu 10100  
Quantity: 2

## REFERENCES

- [1] N. G. Adams and D. Smith. The selected ion flow tube (SIFT); A technique for studying ion-neutral reactions. *International Journal of Mass Spectrometry and Ion Physics*, 21(3-4):349–359, 1976.
- [2] Marcelino Agúndez and Valentine Wakelam. Chemistry of Dark Clouds: Databases, Networks, and Models. *Chemical Reviews*, 113(12):8710–8737, 2013.
- [3] PB Armentrout. Reactions and Thermochemistry of Small Transition Metal Cluster Ions. *Annual Review of Physical Chemistry*, 52(1):423–461, 2002.
- [4] J J Bollinger, J S Wells, D J Wineland, and Wayne M Itano. Hyperfine structure of the  $2p^2P_{1/2}$  state in  ${}^9\text{Be}^+$ . *Physical Review A*, 31(4):2711–2714, 1985.
- [5] Michael J. Bronikowski, William R. Simpson, Bertrand Girard, and Richard N. Zare. Bond-specific chemistry: OD:OH product ratios for the reactions H+HOD(100) and H+HOD(001). *Journal of Chemical Physics*, 95(11):8647–8648, 1991.
- [6] Eduardo Carrascosa, Jennifer Meyer, and Roland Wester. Imaging the dynamics of ion-molecule reactions. *Chemical Society Reviews*, 46(24):7498–7516, 2017.
- [7] Kuang Chen, Scott T. Sullivan, and Eric R. Hudson. Neutral gas sympathetic cooling of an ion in a Paul trap. *Physical Review Letters*, 112(14):1–5, 2014.
- [8] Kuang Chen, Scott T. Sullivan, Wade G. Rellergert, and Eric R. Hudson. Measurement of the coulomb logarithm in a radio-frequency Paul trap. *Physical Review Letters*, 110(17):1–5, 2013.
- [9] D. C Clary. Fast Chemical Reactions: Theory Challenges Experiment. *Annual Review of Physical Chemistry*, 41(1):61–90, 1990.
- [10] F. Fleming Crim. Bond-selected chemistry: Vibrational state control of photodissociation and bimolecular reaction. *Journal of Physical Chemistry*, 100(31):12725–12734, 1996.
- [11] N. F. Dalleska, Kevin C. Crellin, and P. B. Armentrout. Reactions of alkaline earth ions with hydrogen, deuterium, and hydrogen deuteride. *The Journal of Physical Chemistry*, 97(13):3123–3128, 2005.
- [12] C. E. Dateo and D. C. Clary. Rate constant calculations on the  $\text{C}^+ + \text{HCl}$  reaction. *The Journal of Chemical Physics*, 1989.
- [13] Colin G. Freeman, John S. Knight, Jonathan G. Love, and Murray J. McEwan. The reactivity of  $\text{HOC}^+$  and the proton affinity of CO at O. *International Journal of Mass Spectrometry and Ion Processes*, 80(C):255–271, 1987.

- [14] Colin G. Freeman and Murray J. McEwan. A selected-ion flow tube study of the  $\text{C}^+ + \text{H}_2\text{O}$  reaction. *International Journal of Mass Spectrometry and Ion Processes*, 75(1):127–131, 1987.
- [15] Bina Fu and Dong H. Zhang. A full-dimensional quantum dynamics study of the mode specificity in the  $\text{H} + \text{HOD}$  abstraction reaction. *Journal of Chemical Physics*, 142(6), 2015.
- [16] George Gioumousis and D. P. Stevenson. Reactions of gaseous molecule ions with gaseous molecules. V. theory. *The Journal of Chemical Physics*, 29(2):294–299, 1958.
- [17] Anders K. Hansen, Magnus A. Sørensen, Peter F. Staanum, and Michael Drewsen. Single-ion recycling reactions. *Angewandte Chemie - International Edition*, 51(32):7960–7962, 2012.
- [18] William L. Hase, Jochen Mikosch, Roland Wester, Jiaxu Zhang, Rico Otto, and Jing Xie. Identification of Atomic-Level Mechanisms for Gas-Phase  $\text{X}^- + \text{CH}_3 \rightarrow \text{S}_{\text{N}}2$  Reactions by Combined Experiments and Simulations. *Accounts of Chemical Research*, 47(10):2960–2969, 2014.
- [19] J L Highberger, C Savage, J H Bieging, and L M Ziurys. HEAVY-METAL CHEMISTRY IN PROTO-PLANETARY NEBULAE: DETECTION OF MgNC, NaCN, AND AlF TOWARD CRL 2688. *the Astrophysical Journal*, 562:790–798, 2001.
- [20] Eric R. Hudson. Sympathetic cooling of molecular ions with ultracold atoms. *EPJ Techniques and Instrumentation*, 3(1):8, 2016.
- [21] W. T. Huntress and R. F. Pinizzotto. Product distributions and rate constants for ion-molecule reactions in water, hydrogen sulfide, ammonia, and methane. *The Journal of Chemical Physics*, 59(9):4742–4756, 2004.
- [22] Nicholas R Hutzler, Hsin-I Lu, and John M Doyle. The buffer gas beam: an intense, cold, and slow source for atoms and molecules. *Chemical reviews*, 112(9):4803–27, sep 2012.
- [23] NR Nicholas R Hutzler, MF Maxwell F Parsons, Yulia V Gurevich, Paul W Hess, Elizabeth Petrik, Ben Spaun, Amar C Vutha, David Demille, Gerald Gabrielse, and John M Doyle. A cryogenic beam of refractory, chemically reactive molecules with expansion cooling. . . . *Chemistry Chemical . . . ,* 13(42):1–16, 2011.
- [24] Vladimir A Krasnopolsky. Chemical composition of Titan’s atmosphere and ionosphere: Observations and the photochemical model. *Icarus*, 236:83–91, 2014.
- [25] D. J. Larson, J. C. Bergquist, J. J. Bollinger, Wayne M. Itano, and D. J. Wineland. Sympathetic cooling of trapped ions: A laser-cooled two-species nonneutral ion plasma. *Physical Review Letters*, 57(1):70–73, 1986.

- [26] Adan Li, Jianzheng Song, Yang Sun, and Tifeng Jiao. The application of resonance-enhanced multiphoton ionization technique in gas chromatography mass spectrometry. *Journal of Spectroscopy*, 2014, 2014.
- [27] Jun Li, Bin Jiang, and Hua Guo. Spin-orbit corrected full-dimensional potential energy surfaces for the two lowest-lying electronic states of  $\text{FH}_2\text{O}$  and dynamics for the  $\text{F} + \text{H}_2\text{O} \rightarrow \text{HF} + \text{OH}$  reaction. *Journal of Chemical Physics*, 138(7), 2013.
- [28] Jun Li, Bin Jiang, Hongwei Song, Jianyi Ma, Bin Zhao, Richard Dawes, and Hua Guo. From ab initio potential energy surfaces to state-resolved reactivities:  $\text{X} + \text{H}_2\text{O} \leftrightarrow \text{HX} + \text{OH}$  [ $\text{X} = \text{F}, \text{Cl}$ , and  $\text{O}({}^3\text{P})$ ] reactions. *Journal of Physical Chemistry A*, 119(20):4667–4687, 2015.
- [29] U. Lourderaj, M. Weidemuller, W. L. Hase, J. Mikosch, R. Otto, R. Wester, C. Eichhorn, J. X. Zhang, and S. Trippel. Imaging Nucleophilic Substitution Dynamics. *Science*, 319(5860):183–186, 2008.
- [30] Ricardo B. Metz, John D. Thoemke, Joann M. Pfeiffer, and F. Fleming Crim. Selectively breaking either bond in the bimolecular reaction of  $\text{HOD}$  with hydrogen atoms. *Journal of Chemical Physics*, 99(3):1744–1751, 1993.
- [31] Edvardas Narevicius, Adam Libson, Christian G. Parthey, Isaac Chavez, Julia Narevicius, Uzi Even, and Mark G. Raizen. Stopping supersonic oxygen with a series of pulsed electromagnetic coils: A molecular coilgun. *Physical Review A - Atomic, Molecular, and Optical Physics*, 77(5):1–4, 2008.
- [32] M. Oppenheimer and A. Dalgarno. The Fractional Ionization in Dense Interstellar Clouds. *The Astrophysical Journal*, 192(12):29, 2002.
- [33] Hans Pauly. *Atom, Molecule, and Cluster Beams I: Basic Theory, Production and Detection of Thermal Energy Beams*, volume 28. Springer, 2000.
- [34] Prateek Puri, Michael Mills, Christian Schneider, Ionel Simbotin, John A. Montgomery, Robin Côté, Arthur G. Suits, and Eric R. Hudson. Synthesis of mixed hypermetallic oxide  $\text{BaO}\text{Ca}^+$  from laser-cooled reagents in an atom-ion hybrid trap. *Science*, 357(6358):1370–1375, 2017.
- [35] Amelia W. Ray, Jianyi Ma, Rico Otto, Jun Li, Hua Guo, and Robert E. Continetti. Effects of vibrational excitation on the  $\text{F} + \text{H}_2\text{O} \rightarrow \text{HF} + \text{OH}$  reaction: Dissociative photodetachment of overtone-excited  $[\text{F}-\text{H}-\text{OH}]^-$ . *Chemical Science*, 8(11):7821–7833, 2017.
- [36] B. Roth, P. Blythe, H. Wenz, H. Daerr, and S. Schiller. Ion-neutral chemical reactions between ultracold localized ions and neutral molecules with single-particle resolution. *Physical Review A - Atomic, Molecular, and Optical Physics*, 73(4):1–9, 2006.

- [37] Christian Schneider, Steven J. Schowalter, Kuang Chen, Scott T. Sullivan, and Eric R. Hudson. Laser-Cooling-Assisted Mass Spectrometry. *Physical Review Applied*, 2(3):1–7, 2014.
- [38] Steven J. Schowalter, Kuang Chen, Wade G. Rellergert, Scott T. Sullivan, and Eric R. Hudson. An integrated ion trap and time-of-flight mass spectrometer for chemical and photo- reaction dynamics studies. *Review of Scientific Instruments*, 83(4), 2012.
- [39] Steven J. Schowalter, Alexander J. Dunning, Kuang Chen, Prateek Puri, Christian Schneider, and Eric R. Hudson. Blue-sky bifurcation of ion energies and the limits of neutral-gas sympathetic cooling of trapped ions. *Nature Communications*, 7:1–8, 2016.
- [40] Ian R Sims. Gas-Phase Reactions and Energy Transfer at Very Low Temperatures. *Annual Review of Physical Chemistry*, 46(1):109–137, 2002.
- [41] Amitabha Sinha, Mark C. Hsiao, and F. Fleming Crim. Bond-selected bimolecular chemistry:  $\text{H} + \text{HOD}(4\nu_{OH}) \rightarrow \text{OD} + \text{H}_2$ . *The Journal of Chemical Physics*, 92(10):6333–6335, 1990.
- [42] Dimitris Skouteris, David E. Manolopoulos, Wensheng Bian, Hans Joachim Werner, Lih Huey Lai, and Kopin Liu. Van der Waals interactions in the Cl + HD reaction. *Science*, 286(5445):1713–1716, 1999.
- [43] I. W M Smith and Bertrand R. Rowe. Reaction kinetics at very low temperatures: Laboratory studies and interstellar chemistry. *Accounts of Chemical Research*, 33(5):261–268, 2000.
- [44] Theodore P. Snow and Veronica M. Bierbaum. Ion Chemistry in the Interstellar Medium. *Annual Review of Analytical Chemistry*, 1(1):229–259, 2008.
- [45] Hongwei Song and Hua Guo. Vibrational and Rotational Mode Specificity in the Cl + H<sub>2</sub>O → HCl + OH Reaction: A Quantum Dynamical Study. *Journal of Physical Chemistry A*, 119(24):6188–6194, 2015.
- [46] Hongwei Song, Soo Ying Lee, Yunpeng Lu, and Hua Guo. Full-Dimensional Quantum Dynamical Studies of the Cl + HOD → HCl/DCl + OD/OH Reaction: Bond Selectivity and Isotopic Branching Ratio. *Journal of Physical Chemistry A*, 119(50):12224–12230, 2015.
- [47] Timothy Su and Michael T. Bowers. Ion-polar molecule collisions: the effect of ion size on ion-polar molecule rate constants; the parameterization of the average-dipole-orientation theory. *International Journal of Mass Spectrometry and Ion Physics*, 12(4):347–356, 1973.
- [48] Timothy Su and Michael T. Bowers. Theory of ion-polar molecule collisions. Comparison with experimental charge transfer reactions of rare gas ions to geometric isomers of difluorobenzene and dichloroethylene. *The Journal of Chemical Physics*, 58(7):3027–3037, 1973.

- [49] Timothy Su and Michael T. Bowers. Ion-polar molecular collisions: the average quadrupole orientation theory. *International Journal of Mass Spectrometry and Ion Physics*, 17(3):309–319, 1975.
- [50] Michał Tomza, Krzysztof Jachymski, Rene Gerritsma, Antonio Negretti, Tommaso Calarco, Zbigniew Idziaszek, and Paul S. Julienne. Cold hybrid ion-atom systems. pages 1–61, 2017.
- [51] J. Troe. Statistical adiabatic channel model of ion-neutral dipole capture rate constants. *Chemical Physics Letters*, 122(5):425–430, 1985.
- [52] Ewine F. van Dishoeck, Eric Herbst, and David A. Neufeld. Interstellar Water Chemistry: From Laboratory to Observations. *Chemical Reviews*, 113(12):9043–9085, 2013.
- [53] Stefan Willitsch. Coulomb-crystallised molecular ions in traps: Methods, applications, prospects. *International Reviews in Physical Chemistry*, 31(2):175–199, 2012.
- [54] D. J. Wineland and Wayne M. Itano. Laser cooling of atoms. *Physical Review A*, 20(4):1521–1540, 1979.
- [55] Paul Wolfgang. Electromagnetic Traps For charged And Neutral Particles, 1990.
- [56] Chunlei Xiao, Xin Xu, Shu Liu, Tao Wang, Wenrui Dong, Tiangang Yang, Zhigang Sun, Dongxu Dai, Xin Xu, Dong H Zhang, and Xueming Yang. Experimental and theoretical differential cross sections for a four-atom reaction:  $\text{HD} + \text{OH} \rightarrow \text{H}_2\text{O} + \text{D}$ . *Science*, 333(6041):440–442, 2011.
- [57] Richard N. Zare. Laser Control of Chemical Reactions. *Science*, 279(5358):1875–1879, 1998.
- [58] Dong H Zhang and John C Light. Full-dimensional quantum study. 93(5):691–697, 1997.
- [59] Dongdong Zhang and Stefan Willitsch. Cold ion chemistry. 2017.
- [60] Rui Zheng, Yongfa Zhu, and Hongwei Song. Mode specific dynamics in bond selective reaction  $\text{O}'(^3\text{P}) + \text{HOD} \rightarrow \text{O}'\text{H} + \text{OD}/\text{O}'\text{D} + \text{OH}$ . *Journal of Chemical Physics*, 149(5), 2018.